



THEORETICAL INVESTIGATION INTO THE PHOTOPHYSICAL  
PROPERTIES OF IRIDIUM(III) COMPLEXES WITH  
*N*-HETEROCYCLIC CARBENE LIGANDS

BY

MR. PHOOM CHUMPONANOMAKUN

A THESIS SUBMITTED IN PARTIAL FULFILLMENT OF THE REQUIREMENTS  
FOR THE DEGREE OF MASTER OF SCIENCE (CHEMISTRY)

DEPARTMENT OF CHEMISTRY  
FACULTY OF SCIENCE AND TECHNOLOGY  
THAMMASAT UNIVERSITY  
ACADEMIC YEAR 2017

COPYRIGHT OF THAMMASAT UNIVERSITY

THEORETICAL INVESTIGATION INTO THE PHOTOPHYSICAL  
PROPERTIES OF IRIDIUM(III) COMPLEXES WITH  
*N*-HETEROCYCLIC CARBENE LIGANDS

BY

MR. PHOOM CHUMPONANOMAKUN



A THESIS SUBMITTED IN PARTIAL FULFILLMENT OF THE REQUIREMENTS  
FOR THE DEGREE OF MASTER OF SCIENCE (CHEMISTRY)  
DEPARTMENT OF CHEMISTRY  
FACULTY OF SCIENCE AND TECHNOLOGY  
THAMMASAT UNIVERSITY  
ACADEMIC YEAR 2017  
COPYRIGHT OF THAMMASAT UNIVERSITY

THAMMASAT UNIVERSITY  
FACULTY OF SCIENCE AND TECHNOLOGY

THESIS

BY

MR. PHOOM CHUMPONANOMAKUN

ENTITLED

THEORETICAL INVESTIGATION INTO THE PHOTOPHYSICAL PROPERTIES OF IRIDIUM(III)  
COMPLEXES WITH *N*-HETEROCYCLIC CARBENE LIGANDS

was approved as partial fulfillment of the requirements for  
the degree of master of science (chemistry)

on July 11, 2018

Chairman




(Asst. Prof. Nanthawat Wannarit, Ph.D.)

Advisor



(Assoc. Prof. Yuthana Tantirungrotechai, Ph.D.)

Co-advisor



(Siriporn P. Naprasertkul, Ph.D.)

Member



(Asst. Prof. Nararak Leesakul, Ph.D.)

Dean



(Assoc. Prof. Somchai Chakhatrakan, Ph.D.)

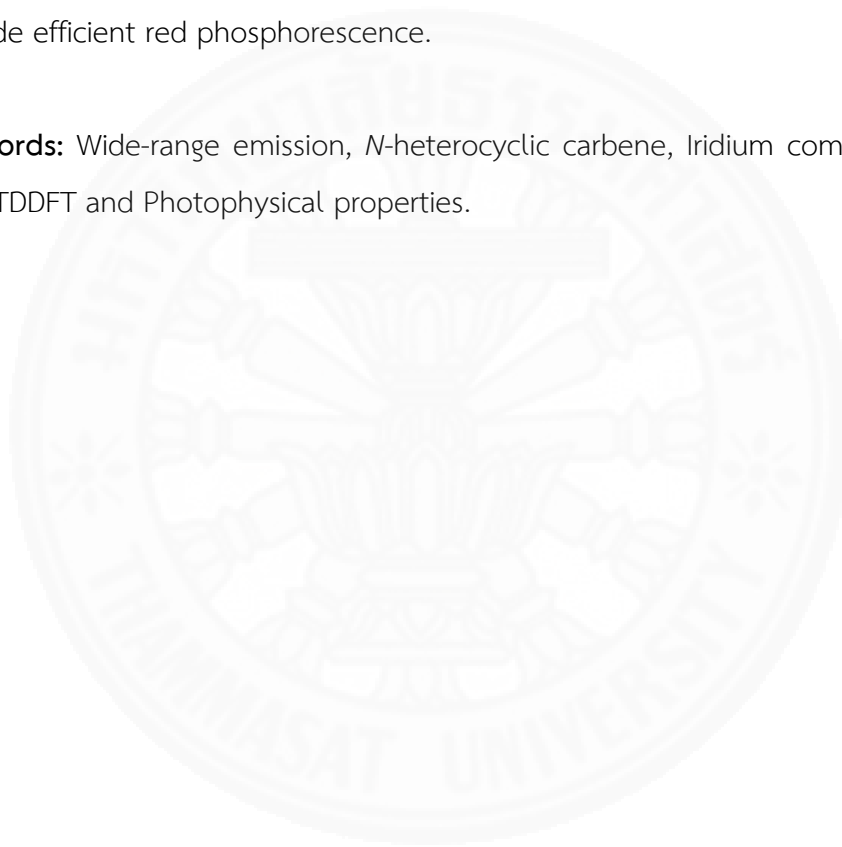
Thesis Title	THEORETICAL INVESTIGATION INTO THE PHOTOPHYSICAL PROPERTIES OF IRIIDIUM(III) COMPLEXES WITH <i>N</i> -HETEROCYCLIC CARBENE LIGANDS
Author	Mr. Phoom Chumponanomakun
Degree	Master of Science (Chemistry)
Department/Faculty/University	Department of Chemistry Faculty of Science and Technology Thammasat University
Thesis Advisor	Assoc. Prof. Yuthana Tantirungrotechai, Ph.D.
Thesis Co-Advisor	Siriporn P. Naprasertkul, Ph.D.
Academic Years	2017

## ABSTRACT

The modified *N*-heterocyclic carbene (NHC) ligands were applied to form complex with Iridium atom for wide-range emission from blue to red. The structural-dependent photophysical properties of the Iridium(III) complexes were investigated by density functional theory (DFT) and time-dependent density functional theory (TDDFT). The phosphorescence emission energies and quantum efficiency of the complexes were determined for exploring the effect of the different positions of  $\pi$ -conjugation in the NHC ligands on the photophysical properties. The emission energies were calculated by the  $\Delta$ SCF-DFT and TDDFT methods basis on the optimized triplet geometry. The radiative decay processes including the radiative rates, transition dipole moments, singlet-triplet spitting energies, and spin-orbit coupling (SOC) constants were detailed evaluated by using TDDFT method. The non-radiative decay processes were considered as two aspects that are the temperature-independence based on energy-gap law and the temperature-dependence following the deactivation pathway from the triplet metal centered state ( $^3MC$ ) to the ground state ( $S_0$ ). The energy different

between the emissive triplet state ( $^3\text{MLCT}$ ) and the ground state at their optimized geometries ( $E_{0-0}$ ) can accurately predict the emission energy of the complexes. The radiative decay rate of the complexes exponentially depends on the  $S_1\text{-}T_1$  splitting energy. The activation energy in thermal deactivation pathway that is the energy barrier of triplet transition state ( $^3\text{TS}$ ) can be controlled by the energy of emissive triplet state. The  $\pi$ -conjugated modifications on NHC Ir(III) complexes can achieve efficient blue and green phosphorescence with high quantum yields, but these modifications cannot provide efficient red phosphorescence.

**Keywords:** Wide-range emission, *N*-heterocyclic carbene, Iridium complexes, OLEDs, DFT, TDDFT and Photophysical properties.



## ACKNOWLEDGEMENTS

I would like to acknowledge several people who contributed to the research and this thesis, in particular. This research would not have been possible without their support.

First, my most sincere thanks are for my advisor, Assoc. Prof. Dr. Yuthana Tantirungrotechai and my co-advior, Dr. Siriporn P. Naprasertkul for their guidance, encouragement and help for all the duration of my master degree.

I gratefully thank the Research Professional Development Project under the Science Achievement Scholarship of Thailand (SAST) (Contract. No. 5712) and the Thammasat University under the TU Research Scholar (Contract No. 55/2560) for financial support.

I would like to express my thanks to Dr. Daniel Escudero for helpful suggestion into radiative rate calculation and Dr. Panichakorn Jaiyong for her recommend.

A special thanks to all members in my laboratory, especially, Mr. Rangsiman Ketkaew and Mrs. Wimon Siri Tanomsridachchai for all support.

Most of all, I would like to express my appreciation to my family for their love, support, and encouragement throughout my study.

Mr. Phoom Chumponanomakun

## TABLE OF CONTENTS

	Page
ABSTRACT	(1)
ACKNOWLEDGEMENTS	(3)
LIST OF TABLES	(6)
LIST OF FIGURES	(8)
LIST OF ABBREVIATIONS	(10)
CHAPTER 1 INTRODUCTION	1
1.1 Phosphorescent iridium complexes	1
1.2 Color tuning of phosphorescence in iridium complexes	4
1.3 <i>N</i> -heterocyclic carbene (NHC) in luminescent complexes	6
1.4 Computational perspective into photochemistry of complexes	7
1.5 Main purposes in this research	9
1.6 Scope of this research	9
CHAPTER 2 REVIEW OF LITERATURE	10
2.1 Structural control of phosphorescent complexes	10
2.2 Prediction of phosphorescence properties	17

CHAPTER 3 RESEARCH METHODOLOGY	21
3.1 Molecular designs	21
3.2 Optimization of $S_0$ and $T_1$ geometries	22
3.3 Absorption and emission energies	23
3.4 Quantum efficiency	24
3.4.1 Radiative decay	24
3.4.2 Vibrational coupling to ground state	26
3.4.3 Thermal population of metal-centered state	27
CHAPTER 4 RESULTS AND DISCUSSION	30
4.1 Optimized geometries	30
4.2 Electronic properties	35
4.3 Absorption energies	38
4.4 Emission energies	40
4.5 Radiative decay	45
4.6 Nonradiative decay of vibrational coupling to ground state	50
4.7 Nonradiative decay of thermal population on $d-d$ state	51
4.8 Quantum yield calculation	56
CHAPTER 5 CONCLUSIONS AND RECOMMENDATIONS	58
REFERENCES	60
APPENDIX	67
BIOGRAPHY	79



## LIST OF TABLES

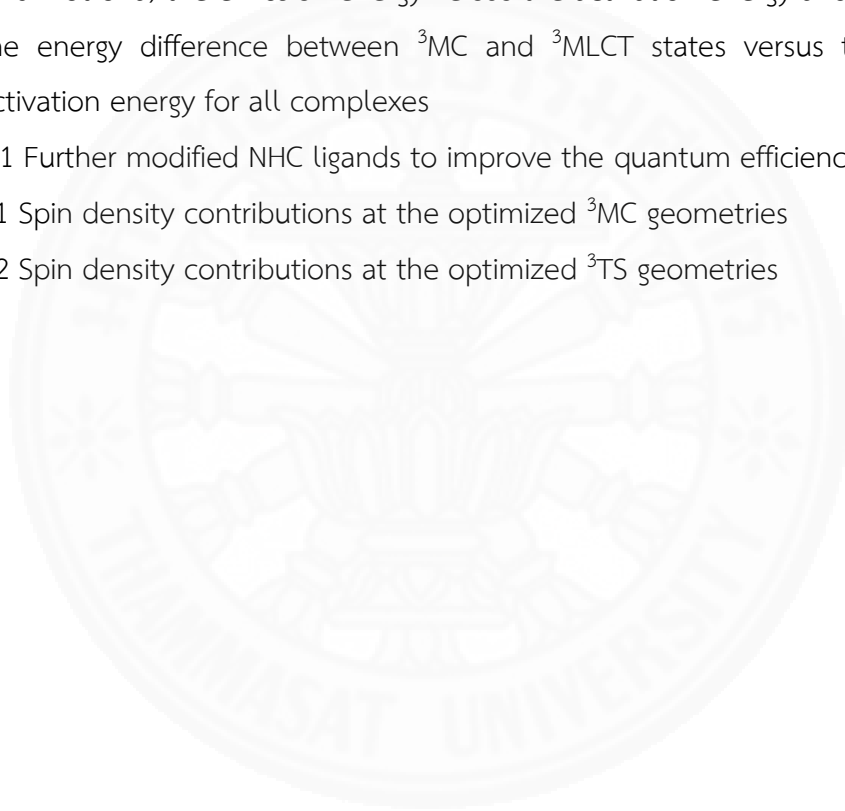
Tables	Page
4.1 Structural parameters of <b>1a</b> and <b>1b</b> complexes	31
4.2 Selected bond distance (Å), bond angles, and dihedral angles (degree) of the $S_0$ and $T_1$ geometries for all complexes	33
4.3 $S_0$ - $T_1$ transition energy, averaged $S_0$ - $T_1$ transition moment, radiative rate constants, and radiative lifetimes for all complexes	47
4.4 Calculated 0-0 transition energies, Huang-Rhys factors, reorganization energies, and calculated $k_{nr}$ at 298 K	51
4.5 Structural parameters of $^3MC$ state for all complexes	53
4.6 Emission energy $E_{0,0}$ and activation energy $E_a$ , $E_b$ , and $E_c$ (kcal/mol) of the metal-centered state decay for all complexes	55
4.7 Summary of phosphorescent quantum efficiencies	57
A1. Energy (eV), electron contribution (%) and main assignment of each molecular orbital for <b>1</b>	73
A2. Energy (eV), electron contribution (%) and main assignment of each molecular orbital for <b>1a</b>	73
A3. Energy (eV), electron contribution (%) and main assignment of each molecular orbital for <b>1b</b>	74
A4. Energy (eV), electron contribution (%) and main assignment of each molecular orbital for <b>2a</b>	74
A5. Energy (eV), electron contribution (%) and main assignment of each molecular orbital for <b>2b</b>	75
A6. Energy (eV), electron contribution (%) and main assignment of each molecular orbital for <b>3a</b>	75
A7. Energy (eV), electron contribution (%) and main assignment of each molecular orbital for <b>3b</b>	76
A8. Energy (eV), electron contribution (%) and main assignment of each molecular orbital for <b>4a</b>	76

Tables	Page
A9. Energy (eV), electron contribution (%) and main assignment of each molecular orbital for <b>4b</b>	77
A10. Calculated absorption energies, oscillator strength ( $f$ ), orbital contributions, and charge transfer characters for selected vertical $S_0$ to $S_n$ transition of the complexes in series <b>1</b>	77
A11. Calculated absorption energies, oscillator strength ( $f$ ), orbital contributions, and charge transfer characters for selected vertical $S_0$ to $S_n$ transition of the complexes in series <b>2</b>	79
A12. Calculated absorption energies, oscillator strength ( $f$ ), orbital contributions, and charge transfer characters for selected vertical $S_0$ to $S_n$ transition of the complexes in series <b>3</b>	80
A13. Calculated absorption energies, oscillator strength ( $f$ ), orbital contributions, and charge transfer characters for selected vertical $S_0$ to $S_n$ transition of the complexes in series <b>4</b>	81
A14. Transition dipole moments, singlet-triplet splitting energies, and SOC constants for the complexes in series <b>1</b>	82
A15. Transition dipole moments, singlet-triplet splitting energies, and SOC constants for the complexes in series <b>2</b>	82
A16. Transition dipole moments, singlet-triplet splitting energies, and SOC constants for the complexes in series <b>3</b>	83
A17. Transition dipole moments, singlet-triplet splitting energies, and SOC constants for the complexes in series <b>4</b>	83

## LIST OF FIGURES

Figures	Page
1.1 Triplet harvesting by rapid intersystem crossing (ISC) from the first singlet state to the lowest triplet state	1
1.2 Photophysical process of cyclometalated Ir(III) complexes	3
1.3 The effect of electron-donating and withdrawing groups on the molecular orbital energies for control of emission color	5
1.4 Adjustment of non-emissive state ( <i>d-d</i> transition state) to control the quantum yield by using <i>N</i> -heterocyclic carbene ligand	7
3.1 Molecular structure of all studied NHC Ir(III) complexes	22
3.2 Temperature-dependent nonradiative channels of Ir(III) complexes	28
4.1 Optimized structure of ground state for complex <b>1</b>	30
4.2 The overlap between X-ray (brown) and PBE0 calculated (gray) structures for <b>1a</b> and <b>1b</b>	31
4.3 Calculated bond length variations between the $S_0$ and $T_1$ geometries for the Ir(III) complexes	34
4.4 Energy levels, energy gaps, and orbital distributiona of HOMO and LUMO for the Ir(III) complexes	36
4.5 Spin density at the optimized $T_1$ geometries for all complexes	38
4.6 Simulated absorption spectra of the complexes in $CH_2Cl_2$ media	39
4.7 Calculated lowest triplet energy wavelengths (nm) of TDDFT method with B3LYP, CAM-B3LYP, PBE0, M05-2X, and M06-2X functionals for all Ir(III) complexes	40
4.8 Calculated lowest triplet energy wavelength (nm) for all complexes	42
4.9 Correlation of calculated $E_{0-0}$ and experimental emission energies	42
4.10 Electron density difference maps (EDDMs) of the emission transition for all complexes	44
4.11 Correlation of radiative rate constants between the experiment and the calculation based on the $S_0$ and $T_1$ optimized geometries	46

Figures	Page
4.12 The splitting energies between lowest triplet state ( $T_1$ ) and higher singlet states ( $S_1$ - $S_6$ ) for all complexes	49
4.13 Radiative decay rate versus $S_1$ - $T_1$ splitting energy for all complexes	49
4.14 Optimized $^3MC$ geometry of <b>1</b> by elongation of Ir-C4 bond length	52
4.15 Relative energy profile of temperature-dependent non-radiative pathways through $^3MC$ state for all complexes	54
4.16 Plot of a) the emission energy versus the activation energy and b) the energy difference between $^3MC$ and $^3MLCT$ states versus the activation energy for all complexes	55
5.1 Further modified NHC ligands to improve the quantum efficiency	59
A1 Spin density contributions at the optimized $^3MC$ geometries	84
A2 Spin density contributions at the optimized $^3TS$ geometries	84



## LIST OF ABBREVIATIONS

Symbols/Abbreviations	Terms
B3LYP	Becke-3-parameter-Lee-Yang-Parr
DFT	Density functional theory
ECP	Effective core potential
EDDMs	Electron difference density maps
FC	Franck-Condon
HOMO	Highest occupied molecular orbital
IC	Internal conversion
ILCT	Intraligand charge transfer
ISC	Intersystem crossing
LC	Ligand-centered
LUMO	Lowest unoccupied molecular orbital
MC	Metal-centered
MECP	Minimum energy crossing point
MLCT	Metal-to-ligand charge transfer
NHC	<i>N</i> -heterocyclic carbene
PBE0	Perdew-Burke-Ernzerhof
PCM	Polarized continuum model
PES	Potential energy surface
$S_0$	Ground state
SCF	Self-consistent field
SOC	Spin-orbit coupling
$T_1$	Lowest triplet state
TDDFT	Time-dependent density functional theory
TS	Transition state
ZFS	Zero-field splitting
ZORA	Zero-order regular approximation

## CHAPTER 1

### INTRODUCTION

#### 1.1 Phosphorescent iridium complexes

Cyclometalated Ir(III) complexes have been widely investigated because they offer thermal stability, high phosphorescence quantum yields, relatively short excited state lifetimes, and simple color tuning by ligand modification.<sup>1</sup> The advantages of the phosphorescent Ir(III) complexes give them applications as luminescent sensors<sup>2-4</sup>, biological labeling agents<sup>5</sup>, photocatalysts for CO<sub>2</sub> reduction<sup>6</sup>, oxygen sensitizers<sup>7-9</sup>, and especially electroluminescence uses as light-emitting electrochemical cells (LECs)<sup>10-14</sup> and organic light-emitting diodes (OLEDs).<sup>14-15</sup> Almost 100% internal quantum efficiency can be achieved by association of both singlet and triplet states as shown in **Figure 1.1**. The first process starts from exciton formation with a 25% singlet and 75% triplet character. Because the central iridium ion contains a significant spin-orbit coupling (SOC), the Ir(III) complexes exhibit a rapid intersystem crossing (ISC) from the first singlet state ( $S_1$ ) to the lowest triplet state ( $T_1$ ).<sup>16</sup> The triplet state can effectively emit photons by harvesting from an association of singlet and triplet excited states.

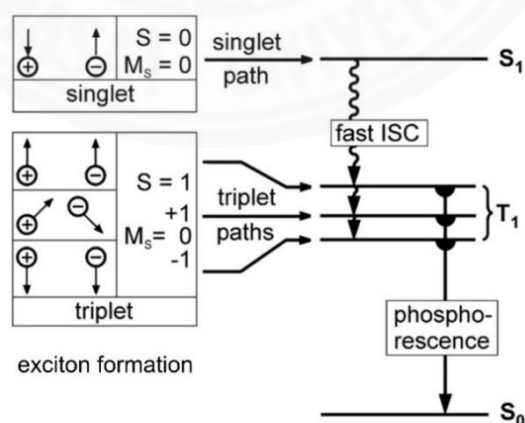


**Figure 1.1** Triplet harvesting by rapid intersystem crossing (ISC) from the first singlet state to the lowest triplet state. Efficient phosphorescence occurs from  $T_1$  to  $S_0$ .<sup>16</sup>

To understand the design strategies for using iridium complexes as phosphors, photoexcitation of the cyclometalated Ir(III) complexes was explored with the simple case of *fac*-iridium *tris*(2-phenylpyridinato) (*fac*-Ir(ppy)<sub>3</sub>).<sup>17</sup> The electronic interactions strongly act on the frontier molecular orbitals: the highest occupied molecular orbital (HOMO) and the lowest unoccupied molecular orbital (LUMO). The participation of molecular orbitals in photoexcitation to the T<sub>1</sub> were obtained using time-dependent density functional theory, based on quantum calculations.<sup>18</sup> The calculation revealed that the HOMO in this complex was mainly delocalized over the *d* orbitals of Iridium and the π orbitals of the phenyl ring, while the LUMO primarily involved the π\* orbitals of the pyridyl ring. The photoexcitation involves two electronic transitions,  $d(\text{Ir}) \rightarrow \pi^*(\text{ligand})$  and  $\pi(\text{ligand}) \rightarrow \pi^*(\text{ligand})$ . These are characterized as metal-to-ligand charge transfer (MLCT) and ligand-centered (LC) transitions, respectively. Moreover, strong SOC derived from the central iridium simplifies the triplet state of MLCT and LC transitions resulting in the production of four electronic states: singlet and triplet states of MLCT and LC transition states (<sup>1</sup>MLCT, <sup>3</sup>MLCT, <sup>1</sup>LC, and <sup>3</sup>LC).

The energy of <sup>1</sup>LC transitions is normally higher than that of <sup>1</sup>MLCT transitions. The <sup>3</sup>MLCT bands are naturally observed between the <sup>1</sup>MLCT and <sup>3</sup>LC transition bands because the exchange energy (difference between singlet energy and triplet energy) of the MC transition is usually smaller than that of the LC transition.<sup>19</sup> Therefore, the order of energy for the four transitions is <sup>1</sup>LC > <sup>1</sup>MLCT > <sup>3</sup>MLCT > <sup>3</sup>LC. Typically, the phosphorescence of the MLCT state has a relatively short lifetime in comparison with that of LC state. A pure LC state produces no phosphorescence, since it lacks the metal character that provides SOC, and therefore the otherwise forbidden T<sub>1</sub> → S<sub>0</sub> emission.<sup>20</sup> The MLCT state, consequently, is associated with the metal component, simplifying efficient triplet emission. Beside the MLCT and LC states, an intra-ligand charge transfer (ILCT) transition can present in cyclometalating ligands with donor-acceptor-type electronic structures.<sup>21-23</sup> The ILCT transitions that are localized on the ligand are similar to LC transitions.

The photophysical processes of common Ir(III) complexes are shown in **Figure 1.2**. First, photoexcitation populates both the LC and MLCT transition states. Two transition states can be intensely coupled due to sharing of ligand localization on LUMO. The higher-lying  $^1\text{LC}$  excited state in  $\text{fac-Ir}(\text{ppy})_3$  can transition to the lower-lying  $^1\text{MLCT}$  excited state with a time constant of more than 100 fs in a process called “internal conversion (IC)”.<sup>24</sup> Due to the SOC effect of the iridium core, the  $^1\text{MLCT}$  excited state can undergo efficient intersystem crossing (ISC) to the  $^3\text{MLCT}$  excited state.<sup>24</sup> The time constant of the ISC process in  $\text{fac-Ir}(\text{ppy})_3$ , of less than 100 fs, is shorter than that of the IC process.<sup>25</sup> Therefore, the phosphorescence of  $\text{fac-Ir}(\text{ppy})_3$  can be obtained by energy relaxation from the  $^3\text{MLCT}$  excited state to the ground state. Additionally, phosphorescence with high efficiency in most Ir(III) complexes can originate from either  $^3\text{MLCT}$  or  $^3\text{MLCT}$  mixed with  $^3\text{LC}$ .<sup>26</sup> Nevertheless, not all complexes are highly phosphorescent, due to the different non-emissive pathways.

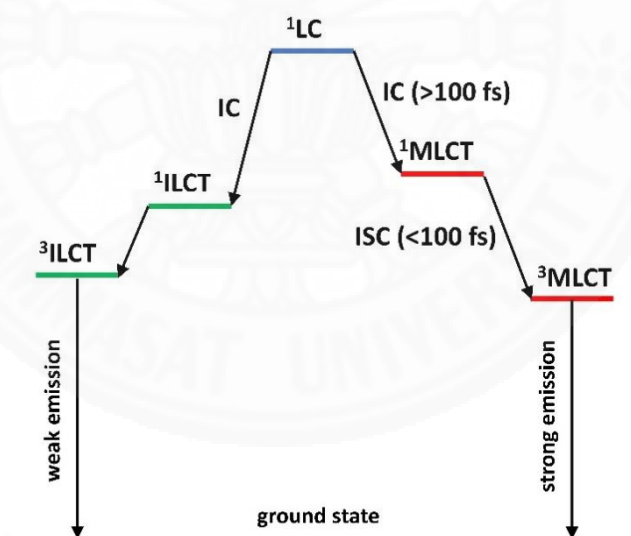


**Figure 1.2** Photophysical process of cyclometalated Ir(III) complexes: LC, ligand-centered state; MLCT, metal-to-ligand charge transfer state; ILCT, intraligand charge transfer state; ISC, intersystem crossing; IC, internal conversion.<sup>19</sup>



## 1.2 Color tuning of phosphorescence in iridium complexes

The phosphorescence color can be altered through ligand substitution in either of the two rings. In the previous example of Ir(ppy)<sub>3</sub>, the phenyl ring with a formal negative charge and the iridium center provide the main distribution to the HOMO, while zero-charge pyridyl ring plays the primary role in the LUMO. In consequence, substitutions in the phenyl ring more strongly affect the HOMO energy than the LUMO energy, whereas substitutions in the pyridyl ring have the opposite effect.<sup>27</sup> Electron-withdrawing substituents (such as the fluoro, cyano, and trifluoromethyl groups) commonly stabilize the molecular orbitals by filling the electron shells, while electron-donating substituents (such as the methylamino and methoxy groups) normally destabilize the molecular orbitals. Ir(ppy)<sub>3</sub> normally emits at the green wavelength, but the emission can be tuned to either red or blue by substitution (see **Figure 1.3**). Red-shift is obtained by substitution of electron-donating groups into the metallated phenyl ring, raising the HOMO energy level. Substitution of electron-withdrawing groups into the pyridyl ring decreases the LUMO energy level, and therefore the HOMO-LUMO energy gap. More extended conjugation (such as by polyaromatic hydrocarbons) on the metallated phenyl ring also decreases the HOMO-LUMO energy gap, leading to a red-shift of phosphorescence. Blue-shift is obtained by substitution of electron-withdrawing substituents into the phenyl ring, reducing the HOMO energy level. The LUMO energy level is increased by substitution of electron-donating group into the pyridyl ring, increasing the HOMO-LUMO energy gap. Blue-shifted emission can also be achieved by replacing the pyridyl ring with more electron-rich aza-heterocycles such as pyrazoles, triazoles, or imidazoles.<sup>28</sup>

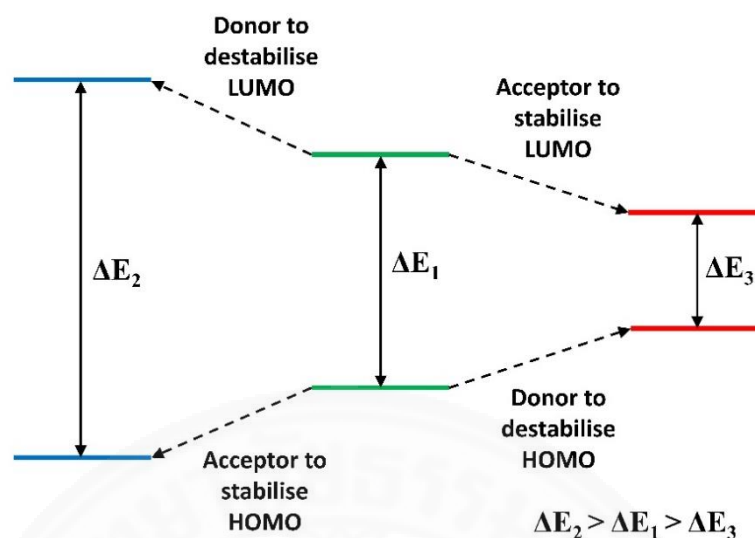


**Figure 1.3** The effect of electron-donating and withdrawing groups on the molecular orbital energies for control of emission color.<sup>20</sup>

Blue emitters are quite challenging to design because of a high emission energy is needed to widen the HOMO-LUMO energy gap in the phosphor. Blue phosphors of Ir(III) complexes naturally show inferior color purity and lower efficiency than green and red phosphors, due to the presence of a metal-centered (MC) *d-d* transition state.<sup>29</sup> The MC state, which is a high energy of transition state, is normally a non-emissive pathway.<sup>30</sup> Deep blue phosphorescence correlates with a high-lying emissive triplet state (<sup>3</sup>MLCT), which is close to the MC transition state. Thermal population of the <sup>3</sup>MC state can occur by energy transfer from the <sup>3</sup>MLCT state, producing non-radiative transition to the ground state. For instance, a homoleptic Ir(III) complex containing 1-phenylpyrazole (ppz) ligand emits deep blue phosphorescence ( $\lambda_{\text{max}} = 414 \text{ nm}$  at 77 K), but its phosphorescence is weak at room temperature.<sup>31</sup> This is because the thermal population of the <sup>3</sup>MC excited state decays to the ground state through non-radiative decay. To address this, *N*-heterocyclic carbene (NHC) ligands were applied, producing blue phosphors with high efficiency.<sup>32</sup>

### 1.3 *N*-heterocyclic carbene (NHC) in luminescent complexes

*N*-heterocyclic carbenes (NHC) have been extensively utilized as transition metal catalysts.<sup>33-34</sup> They have other applications as antitumor agents, liquid crystalline materials, organometallic polymers and luminescent materials.<sup>35</sup> The NHC ligands can shift the metal-carbene antibonding orbitals to higher energy states. As a result, the metal-carbene bonds have a stronger covalent composition than typical coordination bonds, increasing the stability of the complexes.<sup>35</sup>

From these advantages, Thompson and coworkers improved the blue emitters for a fabrication in OLEDs by synthesis of NHC Ir(III) complexes.<sup>32</sup> These complexes exhibit phosphorescence in blue and near-UV regions, and they show higher phosphorescent quantum yield than the Ir(ppz)<sub>3</sub>. The achievement originates from the strong ligand field and sufficient donor strength of the NHC ligand, which can raise the metal-centered *d-d* excited states to high energies causing them thermally inaccessible from the typical emissive triplet excited state as depicted in **Figure 1.4**. Moreover, such NHC iridium complexes applied in OLEDs have also used for avoiding the unstable fluorine-containing material and obtaining pure deep blue phosphorescence.<sup>36</sup> It is advantageous that the emission energies of these complexes can be shifted to lower energies by above color tuning strategies to attain efficient blue, green and red emission. The phosphorescence in blue and green regions should be achievable without shifting of the metal-centered excited state.<sup>37</sup> Therefore, the NHC iridium complexes would be suitable candidate for efficient phosphorescent emitter.<sup>38</sup>

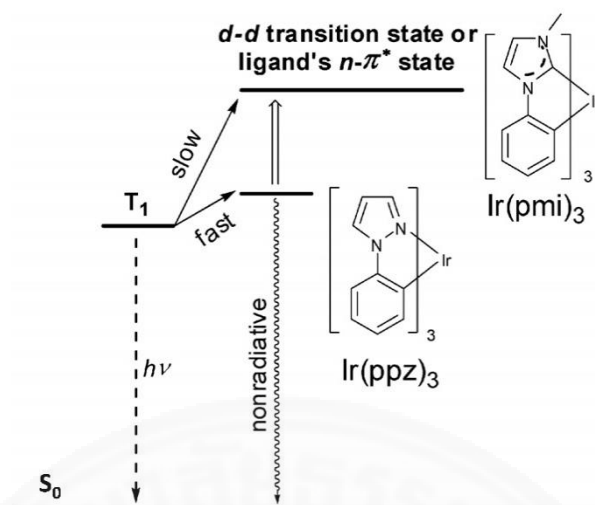


**Figure 1.4** Adjustment of non-emissive state (*d-d* transition state) to control the quantum yield by using *N*-heterocyclic carbene ligand: pmi, 1-phenyl-3-methylimidazolin-2-ylidene.<sup>32</sup>

#### 1.4 Computational perspective into photochemistry of metal complexes

A computational perspective of molecular modeling is useful to insight the properties of material at the atomistic level and to guide the synthesis of new materials through molecular designs. A density functional theory (DFT)<sup>39</sup> as effective method have vastly utilized in photo-functional complexes. An exchange-correlation (XC) of hybrid functionals, which is usually determine the accuracy of calculation, have been mostly used in chemistry such as B3LYP<sup>40</sup>. For excited state properties, the time-dependent functional theory (TDDFT) has become the popular method for accurately predicting photophysical properties in organic and inorganic molecules.<sup>41</sup> Therefore, TDDFT can efficiently simulate absorption spectrum from the ground state geometry. For excited state geometries, TDDFT can also use to search these geometries, so there is the method to gain emission spectra as well as excited state dynamics. The lowest excited states of iridium complexes are normally triplet states; consequently, an approximation of triplet excited state geometries (such as <sup>3</sup>MLCT and <sup>3</sup>MC excited states) can be simply gained by the DFT calculation. Besides, the TDDFT method can

alternatively utilized for calculating the excited state geometries, but consuming time is longer than the DFT method.<sup>42-43</sup>

Normally, solvation effect is included in TDDFT calculation for closely modeling real experiment.<sup>44</sup> There are two models for simulating solvent, i.e. explicit<sup>45</sup> and implicit<sup>46-47</sup> models. Explicit model is simulation of solvent molecules, and it has limitation to only apply in small to medium solutes. Meanwhile, the implicit model is performed as dielectric medium without the structure of solvent, and the solvent is limited within a cavity determined by the molecular structure. Therefore, the model can efficiently reduce the computational cost. Another important effect of the iridium complexes is a relativistic effect, which are occasionally utilized for ground and excited state properties. To calculate the relativistic effect including SOC effect, the four-component Dirac equations that reduced to 2-component procedure such as the zero-order regular approximation (ZORA).<sup>48</sup>

The geometry operated in a calculation is important for precise prediction the emission energy and lifetime of iridium complexes. Many research have predicted phosphorescent properties using optimized triplet geometry reasoning from the exciton population on the  $T_1$  manifold in observed phosphorescence.<sup>49-52</sup> On the other hand, there are some reports that the emission properties obtained from optimized singlet geometry are better agreed with the experiment.<sup>53-56</sup> The better correlation with the experiment was found by calculation of emission energies from both singlet and triplet geometries.<sup>56-57</sup> These observation can be described by the vibrational mode relating to the change between the singlet and triplet geometries. The triplet state displays a shallow and anharmonic potential, so the maximum wave function should locate between the singlet and triplet equilibrium geometries.<sup>56</sup> The reliable calculations of phosphorescent lifetimes was performed using quadratic response (QR) approximation associated with TDDFT method for different iridium complexes.<sup>53, 55-56</sup>

### 1.5 Main purposes in this research

Main objectives in this research are to examine the influence of  $\pi$ -conjugation in *N*-heterocyclic carbene Ir(III) complexes on electronic structures and photophysical properties by theoretical approaches and to explore the computational protocol for reliably predicting photophysical properties such as emission energies, radiative decay process, and nonradiative decay process of the Ir(III) complexes.

### 1.6 Scope of this research

This research focuses on the electronic structures and photophysical properties of the *N*-heterocyclic carbene Ir(III) complexes. The ground and triplet states will be optimized for analysis of structural properties and frontier molecular orbitals. The optimized structures of complexes are further used for investigation of photophysical properties, which are absorption spectra, emission properties including emission wavelengths and quantum efficiency. The radiative rate and non-radiative pathway that are a part of the quantum efficiency will be determined. Additionally, the different DFT methods and solvation effect may be explored for the reliable protocol of calculation, which providing the calculation results is consistent with the experimental results.

## CHAPTER 2

### REVIEW OF LITERATURE

This chapter starts from structural control of phosphorescent Ir(III) complexes with different isomers: facial and meridional isomers, followed by modification of ligand with  $\pi$ -conjugation. Additionally, the calculation methods in emissive properties including emission energies, radiative rate decay, nonradiative rate decay, and quantum yield were also reviewed here.

#### 2.1 Structural control of phosphorescent complexes

Tamayo *et al.*<sup>31</sup> explored structure and photophysics of tris-cyclometalated Ir(III) complexes in facial (*fac*) and meridional (*mer*) isomers. They investigated in both phenylpyridyl-based and phenylpyrazolyl-based Ir(III) complexes. In the synthesis, the meridional isomer of these complexes was formed at 140-150 °C, whereas the facial isomer was predominantly found at higher temperature of reaction. The meridional isomers are more kinetic stability than the facial isomer. The meridional configuration having the phenyl groups are opposite in each other with trans formation, the phenyl groups in the facial configuration are opposite the pyridyl or pyrazolyl groups. The meridional isomer of the phenylpyridyl-based complexes exhibits broader and red-shifted emission relative to the facial isomer, and vice versa for the phenylpyrazolyl-based complexes. The MLCT transition energies of the phenylpyrazolyl-based complexes are blue-shifted compared to those of the phenylpyridyl-based complexes. The phenylpyridyl-based Ir(III) complexes display strong emission at 77 K and room temperature, while the phenylpyrazolyl-based complexes can only exhibit strong emission at 77 K. The lifetimes of phenylpyrazolyl-based complexes also show longer than that of phenylpyridyl-based complexes.

Tsuchiya *et al.*<sup>58</sup> investigated substituted tris(phenylbenzimidazolinato) Ir(III) complexes in both facial and meridional isomers. Electron-withdrawing and electron-donating groups do not affect the structure of complexes. These carbene

complexes were not isomerized from meridional to facial isomer under UV irradiation. The absorption and phosphorescence energies of all substituted complexes were red-shifted relative to the parent complex for both facial and meridional isomers. The radiative rates of these complexes are not different between the facial and meridional isomers with the same substituent. The radiative decay rates are decreased due to the increase of splitting energy between the singlet state and triplet state. Additionally, the extended separation energy between the metal-centered state and  $^3\text{LC}$  state make the non-radiative decay rate reduced.

Cho *et al.*<sup>59</sup> isolated facial and meridional NHC Ir(III) complexes, *fac/mer*-Ir(dbfmi)<sub>3</sub>, to investigate a difference of photophysical properties between two isomers. The phosphorescence of meridional isomer displays slightly red-shifted emission relative to that of facial complex due to more stabilization of  $^3\text{MCLT}$  in meridional complex. The emission transitions of facial isomer are major characterized by  $^3\text{LC}$  state, whereas the transitions of meridional isomer show dominant character of  $^3\text{MLCT}$ . That could be confirmed by the DFT calculation on spin density distribution. The spin density in the  $T_1$  of facial isomer show metal contribution of 7%, while that of meridional isomer are distributed by metal up to 18%. The quantum yields of facial and meridional isomers in dichloromethane solution are 68% and 53%, respectively. The thermal population of  $^3\text{MC}$  state, which is temperature-dependent non-radiative decay, directly depends on the activation energy barriers of both isomers. The activation energy of facial isomer is higher than that of meridional isomer corresponding to the higher quantum yield of facial isomer.

Sajoto *et al.*<sup>32</sup> reported an approach to achieve efficient blue iridium(III) complexes by replacing the ppy ligand in Ir(ppy)<sub>3</sub> with *N*-heterocyclic carbenes (NHC) ligand. They synthesized homoleptic *fac/mer*-Ir(pmi)<sub>3</sub> and *fac/mer*-Ir(pmb)<sub>3</sub> [pmi = 1-phenyl-3-methylimidazolin-2-ylidene, pmb = 1-phenyl-3-methylbenzimidazolin-2-ylidene]. They found that the emissions of these complexes were blue-shifted from the Ir(ppy)<sub>3</sub>. The emission energy of the complexes increases because the NHC ligand has higher triplet energy than ppy ligand leading to the LUMO destabilization. Furthermore, Chien *et al.*<sup>60</sup> also synthesized homoleptic tris-cyclometalated Ir(III)



complexes bearing imidazolium-based carbene *fac/mer*-Ir(ppyi)<sub>3</sub> [ppyi = 2-pyridyl-N-(phenyl)methylamine]. The absorption and emission wavelengths of them were red-shifted compared with Ir(ppy)<sub>3</sub>. The emissions in range of near-infrared render these complexes not suitable for OLEDs application. However, in terms of their photophysical properties, these complexes can be further studied.

Lo *et al.*<sup>61</sup> reported homoleptic Ir(III) complexes composing of phenyltriazole ligands that can exhibit blue phosphorescence at room temperature. The emission is blue-shifted by substitutions of fluorine atoms to the phenyl ring of the ligands, while the emission is red-shifted by substitutions of trifluoromethyl group to the phenyl ring of the ligands. The phosphorescent quantum yields of these complexes are reduced with increase of emission energy. The calculation of molecular orbitals indicated that the fluorinated complexes increase the LC character on the emissive triplet state resulting in the radiative decay rate decreased. Moreover, non-radiative decay rate was dominant to reduce the phosphorescent quantum yields. They found that the type of complexes could not be explained by the energy gap law because these complexes have strong coupling with more than one of Huang-Rhys factor. Therefore, the quenching of phosphorescence should ascribe to thermal activation of vibrational decay.

Liu *et al.*<sup>62</sup> investigated the geometries and electronic properties of *fac/mer*-Ir(pmb)<sub>3</sub> and *fac/mer*-Ir(ppyi)<sub>3</sub> in the ground and excited states by PBE0 and UPBE0 methods. The HOMOs of Ir(pmb)<sub>3</sub> are composed of *d*(Ir) and  $\pi$ (phenyl), whereas those of Ir(ppyi)<sub>3</sub> are contributed by *d*(Ir) and  $\pi$ (carbene). The LUMOs of all complexes are localized on the carbene ligand. They noted that the lowest-lying absorption bands and phosphorescence of all complexes mainly originate from MLCT character. Although their results are consistent with the experimental results, the agreements are qualitative only. Therefore, this type of complexes should be further investigated for quantitative analysis in a quantum efficiency.

Lu *et al.*<sup>63</sup> designed and synthesized biscarbene Ir(III) complexes with *N,N'* heterocyclic (*N^N*) ligands that employ the wide-range emission covering deep-blue to red colors by tuning the *N^N* ligands. The calculations of molecular orbitals show that

the HOMOs are mainly located on the iridium center and carbene ligands, while the LUMOs are predominantly distributed on the  $N^{\wedge}N$  ligands. Therefore, the  $N^{\wedge}N$  ligands play an important role in the change of phosphorescence colors of these complexes. The maximum emission wavelengths of these complexes are red-shifted at room temperature compared with those at 77 K. The phosphorescence lifetimes of these complexes, which were measured in poly(methyl methacrylate) PMMA film, show short lifetimes (1-4  $\mu$ s) leading to high efficiency.

Shang *et al.*<sup>64</sup> investigated the influence of cyclometalated ligands on the photophysical properties of heteroleptic iridium(III) complexes with acetylacetonate (acac) ligand using DFT and TDDFT methods. The extended  $\pi$ -conjugations on the phenyl ring in these complexes specially affect the energies and electron distribution of HOMO. These complexes exhibit red phosphorescence from orange-red to saturated red colors. More rigid structure on the phenyl rings may lead to low quantum efficiency because of larger  $S_1$ - $T_1$  splitting energy and lower MLCT contribution relative to the parent complex.

Han *et al.*<sup>65</sup> explored an extension of  $\pi$ -conjugations of tris-cyclometalated iridium(III) complexes using DFT and TDDFT methods. The conjugation addition on the pyridyl ring can influence both HOMO and LUMO energies, especially the use of rigid ligand. The absorption and emission energies are nearly correlated with the trend of HOMO-LUMO energy gaps. The phosphorescence wavelengths can vary from green to red colors by only modification on the metalated pyridyl ring, and emissive transitions of all these complexes were characterized by LMCT, LLCT and ILCT. The substitutions of phenyl group on the metalated pyridyl ring make higher  $^3$ MLCT contributions, larger singlet-singlet transition dipole moments and smaller  $S_1$ - $T_1$  splitting energies relative to those of the parent complexes resulting in the increase of radiative decay rates.

Shang *et al.*<sup>64</sup> investigated the effect of substituent groups and  $\pi$ -conjugation on the phosphorescent properties of bis(carbene) Ir(III) complexes with  $N^{\wedge}N$  heterocyclic ligands using DFT and TDDFT methods. The modification on the cyclometalated carbene ( $C^{\wedge}C$ ) ligands are introduced by phenyl, fluorophenyl,

(trifluoromethyl)phenyl groups and rigid structures. Phosphorescence energies were accurately predicted by TDDFT method with M06-2X functional. The emissions of these complexes show blue to green colors, and derive from the transitions of LMCT, LLCT and ILCT characters. The substitution of fluorophenyl group on the C<sup>∧</sup>C ligands produce produces highest <sup>3</sup>MLCT contribution, smallest S<sub>1</sub>-T<sub>1</sub> splitting energy and largest <sup>3</sup>MC-<sup>3</sup>MLCT energy gap leading to high quantum efficiency.

Tronnier *et al.*<sup>66</sup> synthesized cyclometalated NHC platinum(II) complexes with acetylacetonate ligand to explore the effect of extended π systems, so different number of phenyl substituents were applied in the NHC ligands. Extension of π-conjugation systems affect the red-shift of emission compared to a parent complex. These complexes display the emission in blue to green regions with high quantum yields. The color changes to lower emission energies derive from the stabilization of LUMO resulting in the smaller energy gaps. The substitution of phenyl group at the N2 position on the imidazole moiety can effectively increase the quantum yield because of higher contribution of MLCT character. More π-conjugated extension can also increase the quantum yield, but emission color can be intensely changed to red-shift.

Thompson *et al.*<sup>67</sup> proposed an approach to increase the emission efficiency of Ir(ppz)<sub>3</sub> (ppz = 1-phenylpyrazole) by a decrease of the triplet energy. Thus, the quenching state is thermally inaccessible. They prepared a counterpart of the Ir(ppz)<sub>3</sub> complex by replacing the phenyl group of ppz with a fluorene. A bonding interaction of the fluorene is similar to that of the phenyl, but the fluorene has a much lower triplet energy than a phenyl group. Therefore, the quenching energy will not be changed with the fluorene substitution, but the triplet will be lower. The emission of fluorene derivative of Ir(ppz)<sub>3</sub> is red shifted about 50 nm comparing with the Ir(ppz)<sub>3</sub>, and the emission efficiency is increased to 0.47 at room temperature. OLEDs that prepared from this fluorene based emitter have external efficiency in range of 6-7%.

Sasabe *et al.*<sup>68</sup> developed high-efficiency blue OLEDs by using mer-Ir(dbfmi)<sub>3</sub> [dbfmi = *N*-dibenzofuranyl-*N*'-methylimidazole]. It shows blue emission with a maximum wavelength at 445 nm. The phosphorescence lifetime of the Ir(dbfmi)<sub>3</sub> is approximately 12 times longer than that of Bis[2-(4,6-difluorophenyl)pyridinato-

C<sup>2</sup>,N](picolinato)iridium(III)<sup>69</sup> (Irpic). Therefore, triplet-triplet annihilation could occur in the blue OLEDs. To prove long lifetime of Ir(dbfmi)<sub>3</sub>, they performed density functional calculations including the spin-orbit coupling effect. They found that the emissive lifetime is 25 μs for Ir(dbfmi)<sub>3</sub> and 3.3 μs for Ir(ppy)<sub>3</sub> as a reference system. Moreover, the MLCT character of Ir(ppy)<sub>3</sub> is roughly twice as large as in Ir(dbfmi)<sub>3</sub>, which is clearly indicated in emissive lifetimes.

Dobbs *et al.*<sup>58</sup> reported highly efficient phosphorescent homoleptic iridium(III) complexes of cyclometalated 5-aryl-1H-1,2,4-triazoles. They showed the effect of aryl substituents attached to the cyclometalated aryl ring that has an influence on emission wavelength of 453-499 nm. The addition of a phenyl ring to two different positions (meta and para relative to the triazole ring) of the phenyl attached with the iridium center leads to a lower triplet emission energy (red-shifted). The red-shifted emission is caused by the decrease of LUMO energies. Moreover, the substitution at meta or para positions of the cyclometalated aryl ring can lower the non-radiative decay rate. Considering the position of substitution, the substitution at the meta position makes an emission bluer than the para substitution which could be expected from the inductive effect of aromatic substitution.

Xie *et al.*<sup>70</sup> theoretically studied the effect of π-conjugation on the photophysical properties of the cyclometalated Ir(III) complexes with auxiliary carbene ligand. The skeleton of π-conjugation shows significant role to determine the phosphorescent properties. The addition of bridging group on the host ligands can affect a blue-shifted emission compared to a parent complex due to the closely degenerated LUMO and LUMO+1 interaction. The extension by bridging group on the host ligand can also make a more coupling between the S<sub>1</sub> state and triplet states resulting in the highest radiative decay rate. The complex with π-conjugated bridging group, which show a rigid molecule, have larger energy gap between the T<sub>1</sub> state and S<sub>0</sub> state and high-lying <sup>3</sup>MC state bringing about the inaccessible non-radiative decay. Therefore, high quantum efficiency and blue phosphors can be achieved by bridging π-conjugated addition on the main ligands.

Amouri *et al.*<sup>71</sup> synthesized deep-red phosphorescent Ir(III) complexes containing a naphthalimide NHC ligand to investigate the influence of naphthalimide unit on the NHC ligand. They found that the emission characters of these complexes are dramatically changed from character of  $^3\text{MLCT}$  to  $^3\text{LC}$  confirmed by TDDFT calculation. The red-shift of emission energies accompanies with the decrease of excited state lifetime corresponding to the energy-gap law. The spin density of  $T_1$  show main distribution on naphthalimide moiety of NHC ligand and some localization on iridium. The quantum yields of these complexes, were measured in polymeric film, have the value in range of 0.16-0.22.

Luo *et al.*<sup>72</sup> designed cyclometalated NHC Pt(II) complexes with acetylacetonate (acac) ligand to investigate the influence of  $\pi$ -conjugation on the phosphorescence properties using DFT and TDDFT. The extended  $\pi$ -conjugation on the NHC ligand significantly affect the emission wavelengths with red-shift from blue to red colors. The radiative decay rates of  $\pi$ -extended complexes are lower than a parent complex due to the decrease of SOC constants and the increase of  $S_1$ - $T_1$  splitting energies. The SOC constants between  $T_1$  and  $S_0$  are decreased by  $\pi$ -conjugated expansion on NHC ligand, so these complexes can avoid the quenching of vibrational coupling to  $S_0$  state. The energy barriers to  $^3\text{MC}$  state are increased by lower emission energies for extended  $\pi$ -conjugation of complexes resulting in the thermal photodeactivation pathways suppressed. Therefore, the non-radiative processes can be effectively reduced by extension of  $\pi$ -conjugation leading to increase the quantum efficiencies.

## 2.2 Prediction of phosphorescence properties

Unger *et al.*<sup>73</sup> predicted the phosphorescence wavelengths of different metal (Osmium, Iridium and Platinum) complexes with reliable results (within 5% of error) relative to the experiment. The emission wavelengths were calculated from energy difference between lowest triplet state and ground state based on the optimized  $T_1$  geometry. This method is more advantage than the TDDFT method, which has a charge-transfer problem of excited states. The double-zeta type of 6-31G\* basis set is adequate for simulation of electronic structure of the  $T_1$  state. Deviations between calculation and experiment of charged complexes were found to larger values compared with those of neutral complexes. Moreover, emission wavelengths of *N*-heterocyclic carbene complexes show correct prediction.

Xu *et al.*<sup>74</sup> calculated emission energies at optimized  $T_1$  geometries using TDDFT with various exchange-correlation functionals containing different percentage of Hartree-Fock (HF) exchange. The calculated emission energies greatly depend on the percentage of HF exchange in the functionals. The increased percentage of HF exchange tends to increase in the calculated emission energies. The predicted emission energies averaged from different functionals linearly correlate with experimental emission energies. Moreover, the  $\Delta$ SCF protocol, which is the most popular approach to compute the emission energy, was used to compare with the TDDFT method. The  $\Delta$ SCF approach also show good agreement with the experimental data. Nevertheless, the TDDFT method provides a better linear correlation with the experiment in comparison with the  $\Delta$ SCF method.

Peng *et al.*<sup>75</sup> investigated emission spectra, radiative decay and nonradiative decay processes of green and deep blue emitting Ir(III) complexes using a thermal vibration correlation function rate theory associated with the DFT and TDDFT methods. The IL character in emissive transition gradually increased together with the decrease of MLCT character according to blue-shift of emission energy. The radiative decay rates are positive correlated with the MLCT character in the emissive triplet state. The nonradiative decay rate dominantly depends on an intramolecular

reorganization energy. The nonradiative decay rate are decreased with diminution of the reorganization energy. The reorganization energy mainly caused by the vibration of chromophore ligands. Therefore, the large MLCT character and low reorganization energy are necessary for high phosphorescent efficiency of blue emitting complexes.

Jansson *et al.*<sup>56</sup> calculated phosphorescence mechanisms of Ir(ppy)<sub>3</sub> using TDDFT quadratic response methods. The emission transitions from T<sub>1</sub> to S<sub>0</sub> are mainly determined by LMCT character. The strong emission of the Ir(ppy)<sub>3</sub> reasonably originates from the high intensity of S<sub>2</sub>–S<sub>5</sub> transitions because of large SOC constants between the T<sub>1</sub> state and the higher singlet states (S<sub>2</sub>–S<sub>5</sub>). The phosphorescence lifetime calculated at S<sub>0</sub> geometry (2 μs) provides a better agreement with the observed lifetime in acetonitrile (1.9 μs) in comparison with the lifetime calculated at T<sub>1</sub> geometry. The S<sub>0</sub>-T<sub>1</sub> transition moments of the T<sub>1</sub> geometry are quite smaller, so the calculated lifetime at the T<sub>1</sub> geometry show longer than that at the S<sub>0</sub> geometry. The reason is that the higher state potential such T<sub>1</sub> state has intensely anharmonic appearance approaching the shallow minimum potential with respect to the displacement of metal-ligand. Therefore, the S<sub>0</sub>-T<sub>1</sub> transition moments should be predicted at the S<sub>0</sub> geometry for accurate phosphorescence lifetime.

Yunker *et al.*<sup>76</sup> explored a computational approach to reliably predict emission properties of vary cyclometalated Ir(III) complexes using TDDFT method with the zero-order relativistic approximation (ZORA). The vertical excitation energies calculated at the S<sub>0</sub> geometry are better correlation with the experimental emission energies than that calculated at the T<sub>1</sub> geometry. The S<sub>0</sub> geometry were used to calculate the radiative rate that can also produce agreement with the experiment. This work supports Jansson's work<sup>56</sup> that they previously used the S<sub>0</sub> geometry to predict phosphorescence properties. The structural optimization under solvent effect was also considered. The emission energies and radiative rate constants, that were calculated using either gas phase or solvent optimized geometries, are almost identical. Consequently, the geometry optimized in gas phase is sufficient to predict the phosphorescent properties.

Haneder *et al.*<sup>77</sup> demonstrated the importance of the singlet-triplet splitting ( $\Delta E_{ST}$ ) in controlling the emission radiative rate of phosphorescent *N*-heterocyclic carbene complexes emitting in the deep-blue. They performed DFT calculations on the  $\text{Ir}(\text{dpbic})_3$  [dpbic = 1-phenyl-3-phenyl-benzimidazolin-2-ylidene-C,C2']. The increase of the  $\pi$ -conjugation in the ligands is also expected to play a role in tuning the splitting, but such approach could simultaneously influence the emission color purity. The low emission efficiency of  $\text{Ir}(\text{dpbic})_3$  can be determined by the non-radiative channel that relates to the torsional degree of freedom of phenyl group linked to the carbene moiety. They also confirmed that the MLCT character influences the  $\Delta E_{ST}$  controlling the radiative rate of complexes.

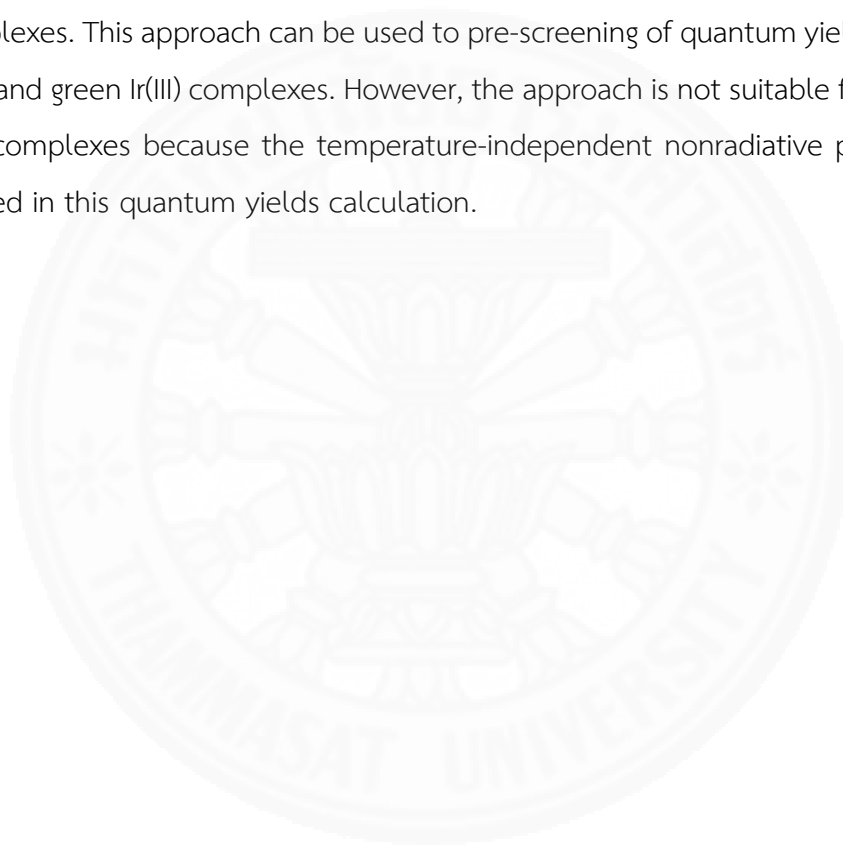
Sajoto *et al.*<sup>78</sup> studied the temperature dependence of high-energy phosphorescent tris-cyclometalated iridium complexes. The temperature-dependent behavior that makes the lower phosphorescent efficiency caused by a thermal activation of nonradiative decay channel. The deactivation takes place via a five coordinate intermediates formed by one metal-ligand bond cleavage. Such intermediates have the electronic structure as a  $^3\text{MC}$  state. One approach to inhibit the bond cleavage is to restrict the degrees of freedom required to dissociation of metal-ligand bond by using rigid ligands such as benzoquinoline.

Zhou *et al.*<sup>79</sup> explored the role of metal-ligand bond elongation from emissive state ( $^3\text{MLCT}$ ) to nonradiative state ( $^3\text{MC}$ ) of blue phosphorescent  $\text{Ir}(\text{III})$  complexes. Because the simple analysis of molecular orbitals does not provide quantitative prediction of nonradiative state, the PES of  $^3\text{MC}$  was searched using the DFT method to deep insight in the observed non-radiative decay rate. The TDDFT with SOC calculation shows that the radiative rate constants of  $^3\text{MC}$  state are two orders of magnitude slower than those of the  $^3\text{MLCT}$  state. The transition barrier energy between the  $^3\text{MLCT}$  state and  $^3\text{MC}$  state is obviously correspond to the observed nonradiative rate constant. Therefore, the thermal population of  $^3\text{MC}$  state is prominent nonradiative process at room temperature for blue phosphor. A metal-ligand bond is shortened in the triplet state, so another metal-ligand bond is lengthened leading to



the metal-ligand bond breaking. This makes the irreversible decomposition of complex to the nonradiative decay.

Escudero<sup>80</sup> first presented an approach to quantitatively predict the phosphorescence quantum yields of blue and green emitting Ir(III) complexes. The calculation of radiative rate of emissive triplet state and PES of thermal deactivation pathways were required to obtain the quantum yields. The calculations of Ir(ppy)<sub>3</sub> were needed as reference before proceeding quantum yields calculation in the other complexes. This approach can be used to pre-screening of quantum yield for unknown blue and green Ir(III) complexes. However, the approach is not suitable for red emitting Ir(III) complexes because the temperature-independent nonradiative processes were ignored in this quantum yields calculation.



## CHAPTER 3

### RESEARCH METHODOLOGY

This chapter describes an inspiration of molecular design for all studied NHC Ir(III) complexes. The methods begin by searching the optimized structure, followed by determination of optical properties including absorption and emission energies. Lastly, the method for quantum efficiency including radiative decay rate, temperature-independent nonradiative decay rate, and temperature-dependent nonradiative decay pathway were also explained in this chapter.

#### 3.1 Molecular designs

Although the *N*-heterocyclic carbene ligand was originally used to achieve blue phosphorescence<sup>32</sup>, the modification of ligand structure can vary emission color from blue to red. Moreover, the structure of ligands also directly affects the quantum efficiency that depends on radiative decay rate and nonradiative decay rate. The NHC Ir(III) complexes of Sajoto's work<sup>32</sup> were first look that are the Ir(pmi)<sub>3</sub> (**1**) and Ir(pmb)<sub>3</sub> (**1a**). The later modification to red emission of Ir(pyip)<sub>3</sub> (**1b**) was also investigated to deeper insight into high energy phosphorescence of the type of complexes.<sup>60</sup> To improve quantum efficiency, the rigid ligands have been considered as followed the complexes **2a** and **2b** to avoid the rupture of metal-ligand bond to <sup>3</sup>MC state. Another approach is the decrease of the emission energy to stay away from the quenching state. To achieve the approach, the increase in the  $\pi$ -conjugation of ligands have been considered by replacing phenyl group with biphenyl and fluorenyl moieties as complexes **3a** and **3b**, respectively. Moreover, the  $\pi$ -conjugation addition on the *N*-heterocyclic carbene moiety as complexes **4a** and **4b**. All investigated complexes are represented in **Figure 3.1**.

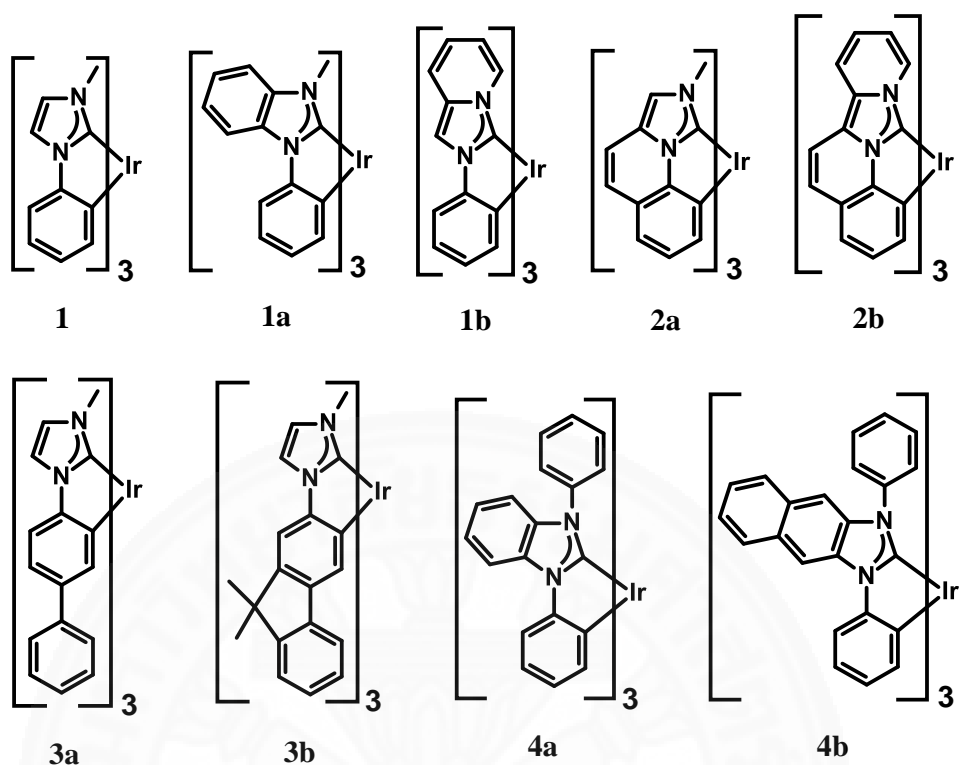


**Figure 3.1** Molecular structures of all studied NHC Ir(III) complexes.

### 3.2 Optimization of $S_0$ and $T_1$ geometries

Geometries of all Ir(III) complexes in ground state ( $S_0$ ) and lowest triplet state ( $T_1$ ) were optimized by restricted and unrestricted density functional theory (RDFT and UDFT). All structures were optimized without any symmetry constraints. The PBE0<sup>81</sup> functional that have proved to be accurately compared with X-ray structure was used to calculate the optimized geometries.<sup>82-84</sup> The LanL2DZ basis set<sup>85</sup> with effective core potential (ECP) was employed for Ir atom, and the 6-31G(d) basis set<sup>86</sup> was applied for light atoms (C, H, and N). Vibrational frequencies were also calculated in the same level of theory to confirm minimum configuration on the potential energy surface that no imaginary frequencies were observed. The B3LYP<sup>40</sup> functional is appropriate to calculate single point (SP) energy on the optimized geometries from PBE0 with the same basis sets for population analysis.

### 3.3 Absorption and emission energies

The absorption energies of singlet-singlet transitions were calculated by using the time-dependent density functional theory (TDDFT) associated with the polarized continuum model (PCM)<sup>45</sup> in dichloromethane (CH<sub>2</sub>Cl<sub>2</sub>) media on the basis of the optimized ground-state equilibrium structures. Emission energies were first evaluated by TDDFT with five popular functionals which are B3LYP, PBE0, CAM-B3LYP<sup>62</sup>, M05-2X<sup>87</sup> and M06-2X<sup>88</sup> at the T<sub>1</sub> geometry. The M06-2X method that is the most consistent with the experimental data was chosen for TDDFT representation. Zero-point energies difference between S<sub>0</sub> and T<sub>1</sub> states at their respective optimized geometries ( $E_{0-0}$ ) and zero-point energies difference between the T<sub>1</sub> and S<sub>0</sub> state at the optimized T<sub>1</sub> geometry ( $E_{\text{vert}}$ ) were also calculated to compare with the energies from TDDFT method ( $E_{\text{TD}}$ ).

The metal contribution (MLCT%) in the transition states<sup>89</sup> can be calculated from the characterization of the HOMO- $x$  → LUMO+ $y$  transitions as partial charge transfer (CT) transitions by using following definition:

$$\text{CT}(\text{M}) = \%(\text{M})\text{HOMO-}x - \%(\text{M})\text{LUMO+}y \quad (1)$$

Here  $\%(\text{M})\text{HOMO-}x$  and  $\%(\text{M})\text{LUMO+}y$  are electronic densities on the metal center in HOMO- $x$  and LUMO+ $y$ . However, the excited states are usually formed by more than one electron excitation. Therefore, the metal charge transfer of the excited-states is formulated as a sum of CT characters of each participating excitation,  $i \rightarrow j$ :

$$\text{CT}_I(\text{M}) = \sum_{i,a} [C_I(i \rightarrow j)]^2 (\%(\text{M})_i - \%(\text{M})_j) \quad (2)$$

Where  $C_I(i \rightarrow j)$  are the appropriate coefficients of the  $I^{\text{th}}$  eigenvector of the CT matrix.

### 3.4 Quantum efficiency

The phosphorescence quantum yield (PLQY) is the main factor of photophysical properties for the complexes that can be expressed as

$$\Phi_{Phos}(T) = \frac{k_r}{k_r + k_{nr} + k_{nr}(T)} \quad (3)$$

It depends on three parameters. First, the radiative rate ( $k_r$ ) which is assumed to be temperature-independent parameter. Therefore, the three substrates of the lowest triplet excited state are equilibrated and other thermal activation of emissive states are not populated. Second, the non-radiative temperature-independent decay rate ( $k_{nr}$ ) depends on the overlap between the ground state ( $S_0$ ) and emissive triplet state ( $T_1$ ) vibrational wave function and follows the energy gap law.<sup>90-92</sup> As  $k_{nr}$  are normally less than  $k_r$  about two times, it can be ignored in quantum yield calculation. Lastly, the temperature-dependent non-radiative rate,  $k_{nr}(T)$ , is the dominating factor that is associated with the thermal population of a non-radiative excited state.

#### 3.4.1 Radiative decay

In a scalar-relativistic behavior, the spin sublevels of the triplet excited states are considered to be degenerated. However, the effect of spin-orbit coupling (SOC) can split the triplet state into three sublevels. Different energy of the three sublevels can be found without the presence of external magnetic field. Therefore, an energy difference between the highest and lowest energy of sublevels is called zero-point splitting energy (ZFS). The phosphorescence radiative decay rate constant ( $k_r^i$ ) from one of the three spin sublevels (indexed by  $i$ ) of the emissive triplet state ( $T_1$ ) can be express in following formula:

$$k_r = k_r(S_0, T_1^i) = \frac{4\alpha_0^3}{3t_0} \Delta E_{S-T}^3 \sum_{j \in (x,y,z)} |M_j^i|^2 \quad (4)$$

where  $\Delta E_{S-T}$  is the transition energy,  $\alpha_0$  is the fine-structure constant,  $t_0 = (4\pi\epsilon_0)^2/m_e e^4$  and  $M_j^i$  is the  $j$  axis projection of the electric dipole transition moment between the ground state ( $S_0$ ) and the  $i^{\text{th}}$  sublevel of the triplet state ( $T_1$ ).

The main contribution to the  $S_0 \rightarrow T_1$  transition moment originates from the first-order corrected wave functions:

$$M_j^i = \sum_{n=0}^{\infty} \frac{\langle S_0 | \hat{\mu}_j | S_n \rangle \langle S_n | \hat{H}_{SO} | T_1^i \rangle}{E(S_n) - E(T_1)} + \sum_{m=1}^{\infty} \frac{\langle S_0 | \hat{H}_{SO} | T_m \rangle \langle T_m | \hat{\mu}_j | T_1^i \rangle}{E(T_m) - E(S_0)} \quad (5)$$

which can be evaluated by the corresponding quadratic response (QR) function.<sup>87, 93</sup> Moreover, the spin-orbit coupling operator ( $\hat{H}_{SO}$ ) in equation (5) can be applied by using the effective single-electron approximation.<sup>94-95</sup> This approximation significantly reduces computational cost because it removes the two-electron spin-orbit integrals. The single-electron SOC operator combined with the effective core potentials (ECPs) basis sets can provide the phosphorescence radiative rate within 15% of the values obtained the full relativistic four-component method.<sup>83</sup>

A thermal population distribution is determined by Boltzmann statistics of the three sublevels, so the total radiative decay rate constant can be showed as follows:

$$k_r = \frac{k_r^1 + k_r^2 \exp(-ZFS_{1,2}/k_B T) + k_r^3 \exp(-ZFS_{1,3}/k_B T)}{1 + \exp(-ZFS_{1,2}/k_B T) + \exp(-ZFS_{1,3}/k_B T)} \quad (6)$$

The values of  $ZFS_{1,2}$  and  $ZFS_{1,3}$  for transition metal complexes are less than  $200 \text{ cm}^{-1}$ .<sup>16</sup> Therefore, at ambient temperature, the observed radiative rate constant ( $k_r$ ) is equal to the algebraic average of the three  $k_r^i$  values

$$k_r = \frac{1}{3} \sum_{i=1}^3 k_r^i \quad (7)$$

The radiative decay rate constants of all complexes were evaluated on the optimized  $S_0$  geometries using linear and quadratic response theories<sup>96-97</sup> in the framework of TDDFT with the B3LYP functional.<sup>56</sup> The SDD with ECP

and 6-31G(d) basis sets were employed for Ir atom and light atoms, respectively. The SOC operator used in the calculations is the effective single-electron approximation suggested by Koseki *et al.*<sup>95</sup> for less time consuming. Spin-orbit coupling (SOC) matrix elements between lowest triplet state and singlet excited states were also calculated with the same method. Calculations implicating SOC operator were performed in DALTON2016 program.<sup>98</sup> Other properties of the radiative decay processes including singlet-triplet splitting energies and transition dipole moment were easily obtained from TD-B3LYP in the Gaussian 09 program.

### 3.4.2 Vibrational coupling to ground state

The non-radiative decay involving vibrational quenching from the emissive triplet state to the ground state can be effectively described based on Fermi's golden rule in the limitation of Condon approximation.<sup>90-92</sup> Under two assumptions, the vibrational wavefunctions of each electronic state are independently harmonic oscillators and parallel of the potential energy surfaces (PES) between  $T_1$  and  $S_0$  states ( $\omega_j^S = \omega_j^T$ ;  $\omega_j^S$  and  $\omega_j^T$  the frequency of the  $j^{\text{th}}$  normal modes of the  $S_0$  and  $T_1$  states, respectively) that are commonly applied to simplify the formal expression into simple and practical form. The Huang-Rhys factor ( $S$ ) of normal modes, which is important parameter of vibrational coupling, was calculated by the Frank-Condon method in frequency calculation with the same method as the optimization. In the low temperature of weak electronic coupling ( $S < 1$  or  $\hbar\omega_M \gg k_B T$ ) along the two assumptions, the non-radiative decay rate of vibrational quenching ( $k_{nr}$ ) according to the energy-gap law<sup>90-92</sup> can be expressed as

$$k_{nr} = \frac{2\pi}{\hbar} \langle S_0 | H_{SO} | T_1 \rangle^2 \left( \frac{1}{2\pi\hbar\omega_M \Delta E'} \right)^{\frac{1}{2}} \exp(-S_M) \exp \left[ -\gamma \frac{\Delta E'}{\hbar\omega_M} + \left( \frac{\gamma+1}{\hbar\omega_M} \right)^2 \lambda_{lf} k_B T \right] \quad (8)$$

$$S_j = \frac{1}{2} \left( \frac{m_j \omega_j}{\hbar} \right) \Delta Q_j^2 \quad (9)$$

$$S_M = \sum_{j \in hf} S_j \quad (10)$$

$$\lambda_M = \sum_{j \in hf} S_j \hbar \omega_j \quad (11)$$

$$\hbar \omega_M = \frac{\lambda_M}{S_M} \quad (12)$$

$$\lambda_{lf} = \sum_{j \in lf} S_j \hbar \omega_j \quad (13)$$

$$\Delta E' = \Delta E_{0-0} - \lambda_{lf} \quad (14)$$

$$\gamma = \ln \left( \frac{\Delta E'}{\lambda_M} \right) - 1 \quad (15)$$

where hf and lf indicate the high-frequency modes ( $1800 > \omega_{hf} > 1000 \text{ cm}^{-1}$ ) and low-frequency modes ( $\omega_{lf} \leq 1000 \text{ cm}^{-1}$ ), respectively,  $m_j$  is the reduced mass of the  $j^{\text{th}}$  normal modes,  $\Delta Q_j$  is the equilibrium displacement along the  $j^{\text{th}}$  normal mode coordinate, and  $\Delta E_{0-0}$  is the zero-point energy difference between the  $T_1$  and  $S_0$  states. The subscript “M” designates one dominant accepting mode which is used to calculate in the equation (8).

### 3.4.3 Thermal population of metal-centered state

The phosphorescence quantum yield (PLQY) strongly depends on temperature dependent. Most complexes can highly emit at 77 K, while the complexes can be quenched at 298 K.<sup>78</sup> The OLEDs should work at ambient temperature, the temperature-dependent behavior of complexes is important to design more efficient phosphors.

The temperature-dependent non-radiative photodeactivation pathways of complexes including Ir(III)<sup>96, 99</sup> and Pt(II)<sup>95, 97</sup> complexes have been studied by computational approaches. These researches described the role of metal centered (<sup>3</sup>MC) in the non-radiative pathways. In **Figure 3.2**, The pseudo-octahedral Ir(III) complexes at  $T_1$  state with predominant <sup>3</sup>MLCT character usually cross a barrier (the transition state; TS) to populate the lowest <sup>3</sup>MC state which commonly shows a trigonal bipyramidal geometry. If the <sup>3</sup>MC state is populated, two main processes can



occur as follows: (i) reversibly back to the  $^3\text{MLCT}$  state or (ii) irreversibly relax to the ground state ( $S_0$ ) geometry. The energy barrier between the  $S_0$  and  $^3\text{MC}$  is determined by minimum energy crossing point (MECP) which displays a more distorted trigonal bipyramidal geometry.

The temperature-dependent non-radiative rate in equation (16),  $k_{\text{nr}}(T)$ , can be expressed into a Boltzmann model<sup>100</sup>,

$$k_{\text{nr}}(T) = A \exp(-E_{\text{lim}}/k_{\text{B}}T) \quad (16)$$

where  $E_{\text{lim}}$  is the activation energy of the limiting step and  $k_{\text{B}}$  is the Boltzmann constant. To achieve the pathways, the DFT calculation are often used for optimizing the ground state ( $S_0$ ) and lowest triplet state ( $T_1$ ) because the DFT calculation can reach a continuous adiabatic system of potential energy surfaces (PES) of the excited states.<sup>95, 99</sup>

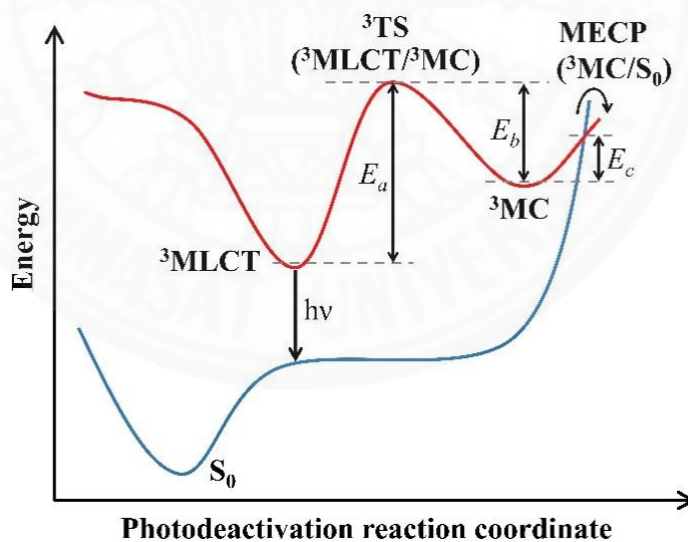


Figure 3.2 Temperature-dependent nonradiative channels of Ir(III) complexes.<sup>96</sup>

There are two scenarios during photodeactivation pathways. First, the formation of the  $^3\text{MC}$  state is the rate limiting step. Therefore, the large values of  $E_a$  ( $E_a \gg E_c$ ) lead to suppression of the temperature-dependent non-radiative channels. Moreover, it can be divided into two possible subkinetic cases: (i) if  $E_c$  is less than  $E_b$ , the population of the  $^3\text{MC}$  state will not be favored to reversible backward reaction. Then, the complexes efficiently undergo the irreversible pathway to the  $S_0$  state. (ii) if  $E_c$  is greater than or equal to  $E_b$ , the barrier to  $^3\text{MLCT}$  state is lowered. A pre-equilibrated between  $^3\text{MLCT}$  and  $^3\text{MC}$  can be reached, so the back reaction to  $^3\text{MLCT}$  state is as preferred as the irreversible relaxation to the  $S_0$  state. Second, the barrier of MECP is the rate limiting step ( $E_c \gg E_a$ ). This case is less benefit to improve the PLQY of phosphors.

The  $^3\text{MC}$  state structures can be located by performing an unrestricted triplet optimization. A starting structure for  $^3\text{MC}$  state optimization can be considered from spin density of  $^3\text{MLCT}$  state. Because lobes of  $d$  orbitals directly point to the carbene ligands in the octahedral geometry of  $^3\text{MLCT}$  state, it raises the energy of the unoccupied  $d$  orbitals. On the other hand, the carbene moiety is moved away from iridium core leading to the lower energy of the unoccupied  $d$ -orbitals.<sup>30</sup> Therefore, the starting  $^3\text{MC}$  structures were constructed by rotation of carbene moiety about 90 degrees from pyridyl group so that the Ir-C (carbene moiety) bonds were elongated. Consequently, the  $^3\text{MC}$  structures after unrestricted optimization should be distorted trigonal bipyramidal.

The minimum energy crossing point (MECP) between the  $S_0$  state and  $^3\text{MC}$  state of potential energy surface was optimized by using the Harvey's algorithm<sup>98</sup> as implemented in the ORCA software.<sup>101</sup> The hybrid functional B3LYP combined with the Def2-SVP basis set (for light atoms) and the ECP-60-MWB Stuttgart/Dresden pseudopotential (for Iridium center) were used for the optimization of MECP. Furthermore, the single point calculation for MECP were performed by B3LYP/6-31G(d) method for providing relative energies.

## CHAPTER 4

### RESULTS AND DISCUSSION

#### 4.1 Optimized geometries

The optimized ground state structure of **1** is depicted in **Figure 4.1** along with number of some key atoms. The main geometric parameters of **1a** and **1b** that were also compared with the available X-ray data<sup>32, 60</sup> are given in **Table 4.1**. Additionally, the calculated structure and X-ray structure were overlaid for comparison as depicted in **Figure 4.2**. The percentage errors of bond length between the calculation and experiment are in the range of 0.041–11% for **1a** and **1b**, so these calculations show agreement with the experimental values. The discrepancy can be occurred because the calculation was performed on the isolated molecule unlike a crystal packing structure in the experiment.

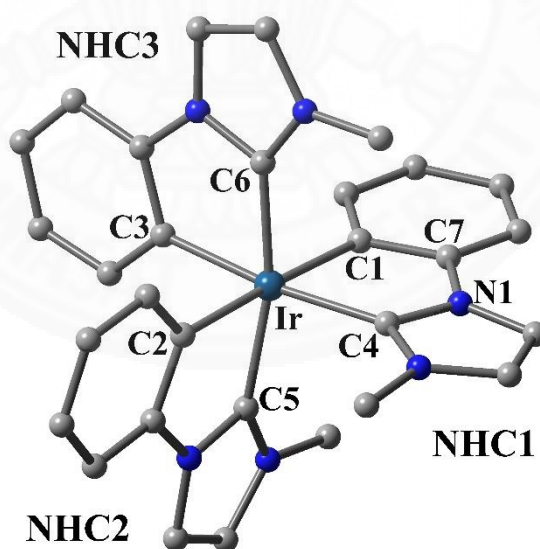


**Figure 4.1** Optimized structure of ground state for complex **1**.

**Table 4.1** Structural parameters of **1a** and **1b** complexes comparing with the experimental data including percentage of error.

	<b>1a</b>			<b>1b</b>		
	exp <sup>a</sup>	calc	%error <sup>b</sup>	exp <sup>a</sup>	calc	%error <sup>b</sup>
Ir-C1	2.098	2.109	0.53	2.259	2.104	6.9
Ir-C2	2.087	2.090	0.17	2.081	2.095	0.67
Ir-C3	2.078	2.073	0.23	2.093	2.073	0.96
Ir-C4	2.043	2.049	0.27	1.844	2.055	11
Ir-C5	2.031	2.028	0.16	1.972	2.032	3.0
Ir-C6	2.019	2.020	0.041	1.965	2.025	3.1

<sup>a</sup> The experimental values was given from ref. 32 and 60.

<sup>b</sup> %error =  $|x(\text{calc}) - x(\text{exp})| / x(\text{exp})$ .

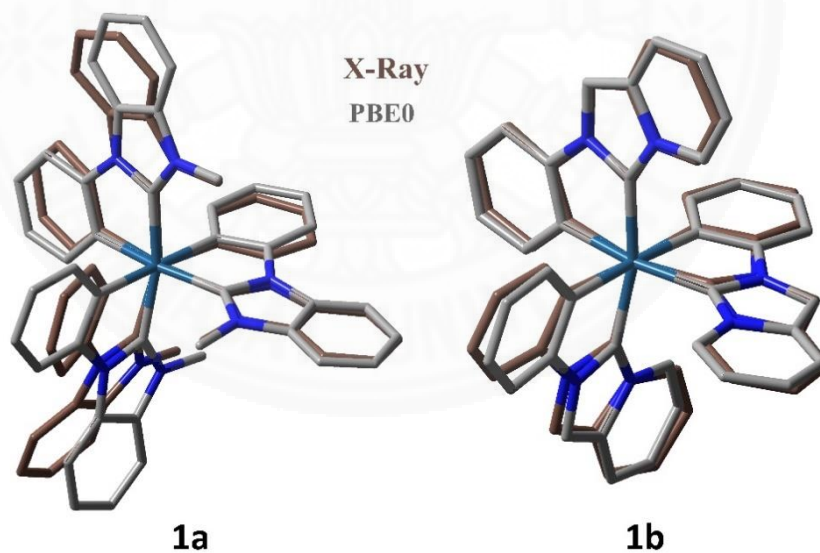


**Figure 4.2** The overlap between X-ray (brown) and PBE0 calculated (gray) structures for **1a** and **1b**.

The main geometrical parameters relating to the iridium atom in the ground state ( $S_0$ ) and the lowest triplet excited state ( $T_1$ ) are listed in **Table 4.2** for all complexes. All Ir(III) complexes display a distorted octahedral geometry for both  $S_0$  and  $T_1$  states. At the ground state, the bond lengths of Ir-C<sub>carbene</sub> (C<sub>carbene</sub>: C4–C6) with the values of 2.016 to 2.071 Å are shorter than those of Ir-C<sub>phenyl</sub> (C<sub>phenyl</sub>: C1–C3) being in range of 2.066–2.115 Å due to electron donor strength of carbene moiety. The modifications of NHC in **1b**, **3a** and **3b** does not make obvious changes in iridium-ligand bond lengths (not over 0.007 Å) in comparison with the parent complex (**1**). The bond lengths of Ir-C5 in **1a**, **4a** and **4b** having the benzimidazolyl groups are slightly shorter (ca. 0.010 Å) with respect to **1**, but they may increase the probability of metal to ligand charge transfer with stronger interaction between Ir(III) center and NHC ligand. In contrast to previous complexes, the bond lengths of Ir-C<sub>phenyl</sub> and Ir-C<sub>carbene</sub> in **2a** and **2b** modified with bridging vinyl groups are elongated in comparison with **1**, particularly the Ir-C6 bond length (variations of 0.026 Å for **2a** and 0.020 Å for **2b**). The weaker bond between iridium and NHC ligand on the **2a** and **2b** indicating that the bridging vinyl groups cause extended  $\pi$ -electron delocalization resulting in the increase of ligand-centered (LC) character. The bond angle changes with respect to **1** are within 1.50 degree for all complexes except C4-Ir-C5 angles of the **4a** and **4b**, which are deviated from those of the **1** by 5.51 and 5.37 degree, respectively. These deviations can be ascribed to the steric effect of the aryl group replacing the methyl group on the carbene moiety in the complexes, which forces the structure of complex to confine within limited space.

**Table 4.2** Selected bond distances (Å), bond angles, and dihedral angles (degree) of the  $S_0$  and  $T_1$  optimized geometries for the complexes.

	<b>1</b>		<b>1a</b>		<b>1b</b>		<b>2a</b>		<b>2b</b>		<b>3a</b>		<b>3b</b>		<b>4a</b>		<b>4b</b>	
	$S_0$	$T_1$	$S_0$	$T_1$	$S_0$	$T_1$	$S_0$	$T_1$	$S_0$	$T_1$	$S_0$	$T_1$	$S_0$	$T_1$	$S_0$	$T_1$	$S_0$	$T_1$
Ir-C1	2.105	2.128	2.109	2.107	2.104	2.110	2.115	2.109	2.111	2.113	2.103	2.096	2.107	2.108	2.107	2.126	2.109	2.104
Ir-C2	2.096	2.056	2.090	2.096	2.095	2.098	2.109	2.114	2.107	2.110	2.095	2.097	2.095	2.098	2.091	2.023	2.094	2.092
Ir-C3	2.076	2.010	2.073	2.009	2.073	2.086	2.086	2.098	2.084	2.097	2.076	2.077	2.078	2.058	2.066	2.052	2.068	2.063
Ir-C4	2.057	2.119	2.049	2.080	2.055	2.018	2.071	2.053	2.065	2.046	2.058	2.052	2.056	2.063	2.052	2.075	2.047	2.067
Ir-C5	2.039	2.045	2.028	2.036	2.032	2.034	2.047	2.070	2.042	2.056	2.040	2.041	2.037	2.039	2.029	2.104	2.024	2.023
Ir-C6	2.021	2.038	2.020	2.058	2.025	2.028	2.047	2.006	2.041	2.016	2.022	2.025	2.022	2.019	2.019	2.016	2.016	2.016
C1-Ir-C4	77.89	77.56	77.63	77.01	77.40	78.40	78.99	79.13	78.68	79.40	77.95	78.87	77.89	77.78	77.68	77.11	77.74	77.48
C1-Ir-C3	93.12	94.20	92.84	92.25	93.24	92.21	92.63	93.92	92.68	94.62	92.76	92.22	92.92	92.54	91.85	90.04	91.84	92.08
C2-Ir-C3	88.74	95.32	87.71	90.93	89.98	89.40	89.64	86.84	90.83	88.20	89.21	89.25	88.69	89.28	86.80	91.32	86.33	86.67
C4-Ir-C5	91.81	88.69	90.69	90.42	91.81	92.98	92.35	92.31	93.21	93.73	92.14	92.38	92.11	92.10	86.30	79.86	86.44	86.05
C4-Ir-C6	99.31	99.36	100.89	97.87	99.59	99.89	98.41	97.73	97.70	97.34	99.18	98.75	99.05	98.55	104.00	109.10	103.69	103.25
C1-C7- N1-C4	-2.23	-1.42	-7.37	-6.61	-1.88	-1.40	-1.19	-1.07	-0.68	-0.40	-1.96	-1.34	-2.12	-2.21	-9.90	-10.85	-9.22	-10.87

The  $T_1$  excited state essentially involves in the phosphorescence process, so the optimized structure of the  $T_1$  state should be considered together with those of the  $S_0$  state. The deviations of bond lengths between the  $S_0$  and  $T_1$  geometries are shown in **Figure 4.3**. The bond length changes of most complexes except for the **1**, **1a** and **4a** are below  $0.042 \text{ \AA}$ . The bond lengths of Ir-C4 and Ir-C6 in  $T_1$  are slightly contracted (within  $0.042 \text{ \AA}$ ) for the **1b**, **2a** and **2b** indicating that the transitions of  $S_0$  to  $T_1$  state more relate to the carbene moiety in the complexes compared with the **1** due to extension of  $\pi$ -conjugation system. The bond distances of the **1**, **1a** and **4a** significantly deviate from the  $S_0$  to  $T_1$  state with the values over  $0.060 \text{ \AA}$  by contraction of Ir-C<sub>phenyl</sub> bonds along with elongation of Ir-C<sub>carbene</sub> bonds. The large structural distortions of the **1**, **1a** and **4a** highly influence on the nonradiative decay involving vibrational quenching. However, there are the other factors, which must be further investigated to evaluate the non-radiative decay rate.

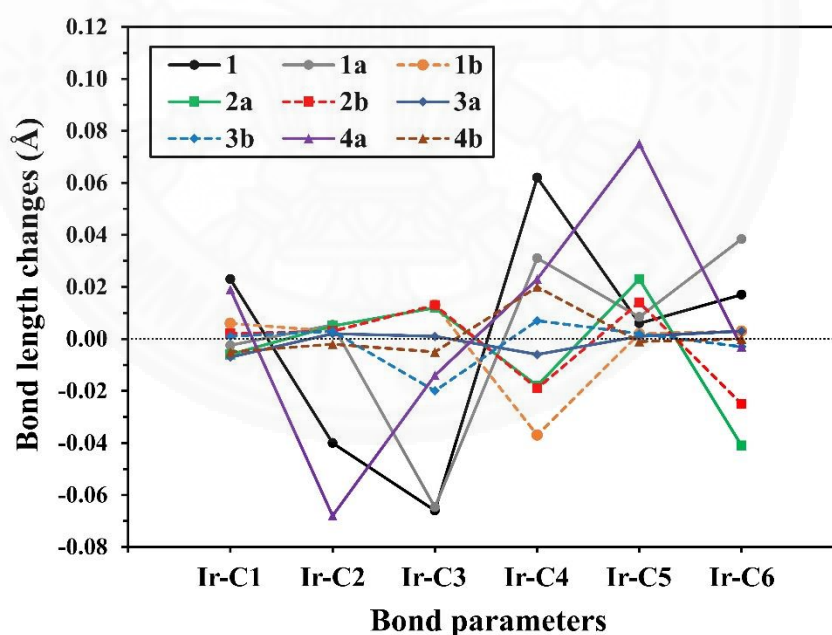


**Figure 4.3** Calculated bond length variations between the  $S_0$  and  $T_1$  for the Ir(III) complexes (the negative values indicate the bond distances contracted in the  $T_1$  state, while the positive ones represent elongation of bonds in the  $T_1$  state).

## 4.2 Electronic properties

The frontier molecular orbitals (FMOs) that closely correlate with the absorption and emission was explored for the Ir(III) complexes. The energy levels and contour plots of HOMO and LUMO for the complexes are depicted in **Figure 4.4**, and the detail of the molecular orbitals in term of energies and percentage compositions of the NHC ligand and iridium orbitals are listed in **Table A1–A9**. The HOMO of the complexes is localized on 30–40% iridium d-orbitals and 60–70% NHC ligand  $\pi$ -orbitals except for those of **2b**, which is mainly distributed by 84%  $\pi$ -orbitals of ligands because of high  $\pi$ -conjugation system in this complex. The HOMO energy, which is involved with the phenyl moiety in the complexes, are not significantly varied (not more than 0.20 eV) from those of the **1**. The little variations of bond lengths between iridium and phenyl moiety in the NHC ligands from previous section cause the small changes in the energy levels of HOMO. The d-orbital compositions of HOMO–1 are reduced by 0–15% from those of HOMO for all complexes excluding the **4b** (reduced by 22%). The HOMO–1 energies of the **2a** and **2b** are extremely close to the HOMO energies of them (difference value of 0.04 eV) on account of the extended  $\pi$ -conjugation in the bridging vinyl groups. The energy differences between HOMO and HOMO–1 of other complexes are approximately in the range of 0.30–0.40 eV, while the **1b** is excluded to 0.08 eV.



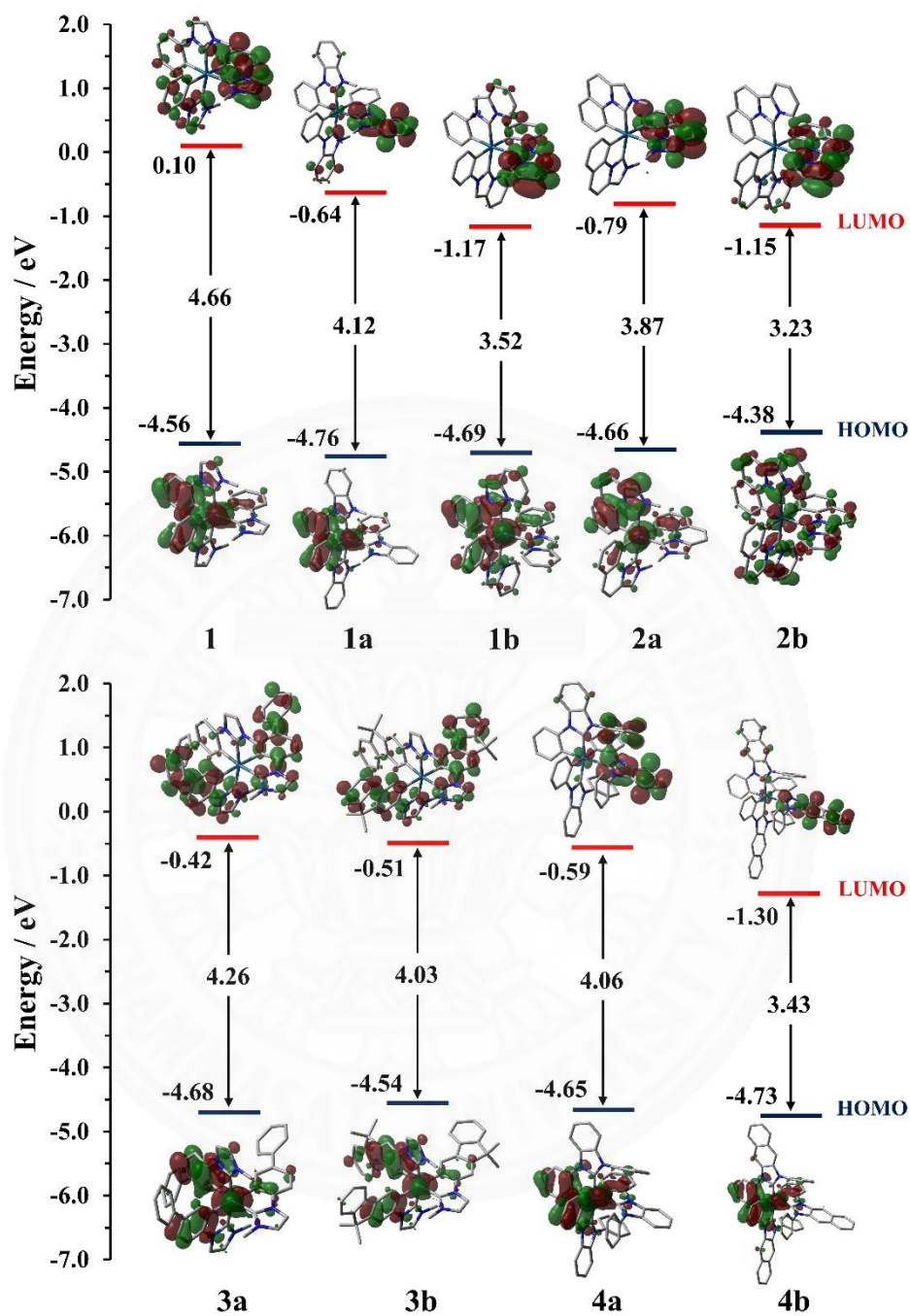
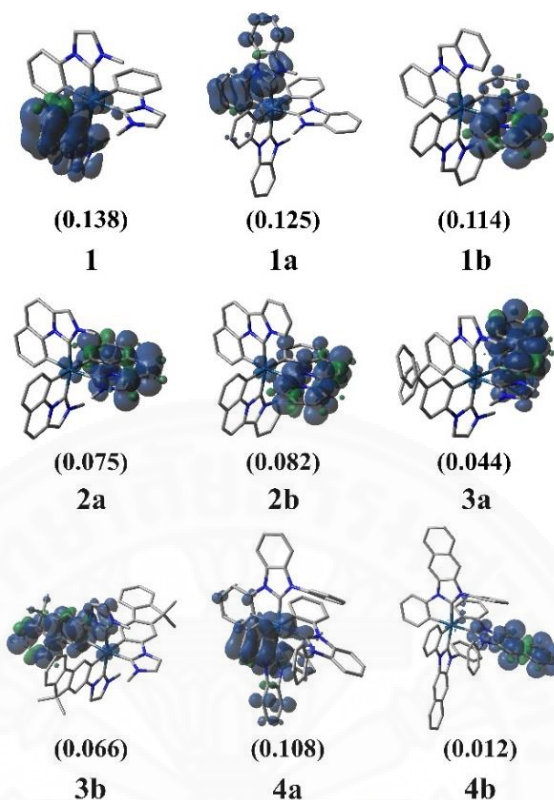


Figure 4.4 Energy levels, energy gaps (in eV), and orbital distribution of HOMO and LUMO for the Ir(III) complexes.

The LUMO of all complexes is mainly distributed by  $\pi$ -orbitals of NHC ligands with more than 95% contributions. The  $\pi$ -orbitals contribution on the NHC ligand of the complexes can be either a carbene moiety or both moieties (carbene and phenyl). The  $\pi$ -orbitals of the parent complex **1** are localized on both moieties, while those of **1a** and **1b** modified by benzimidazolyl group only localized on carbene moiety. The additions of  $\pi$ -conjugation in the phenyl moiety for **2a**, **2b**, **3a** and **3b** cause the  $\pi$ -orbitals more localizing on the phenyl moiety. For **4a** and **4b**, the delocalization of  $\pi$ -orbitals on the carbene moiety are the same case as the **1a** which are only modified on the carbene moiety. The LUMO energy of all modified complexes is more stabilized in comparison with the **1**. The deviation of LUMO energy relating to the **1** are reduced by 0.50 to 1.00 eV for **1b** (0.74), **2a** (0.89), **3a** (0.52), **3b** (0.61) and **4a** (0.69), while the higher values of deviation (more than 1.00 eV) are found in **1b** (1.27), **2b** (1.25) and **4b** (1.40) due to large  $\pi$ -conjugation system in the complexes. More stabilization of the LUMO energy of the modified complexes directly reduces the energy gap compared with the **1**. The energy gaps of the complexes are decreased in order of **1** > **3a** > **1a** > **4a** > **3b** > **2a** > **1b** > **4b** > **2b**. The modifications of the complexes are therefore expected to red-shift in the absorption and emission spectra.

Spin density distributions of the complexes, which were also analyzed on the  $T_1$  optimized geometries, are depicted in **Figure 4.5**. The spin densities of all complexes are mainly distributed by one NHC ligand and iridium atom. Proportions of the iridium atom that are provided in the parentheses usually indicate the metal to ligand charge transfer ( $^3\text{MLCT}$ ) character for transition of emissive triplet state. The iridium proportion of all modified complexes are less than that of the **1** caused by the additional conjugation in the NHC ligands. The modification in the phenyl moiety of the NHC ligands of **2a**, **2b**, **3a** and **3b** highly influence on the proportion of the iridium by more delocalization on the NHC ligands relating to the **1**. Additionally, the lowest proportion of the iridium atom are found in the **4b** having high  $\pi$ -conjugation on the carbene moiety. The **1**, **1a**, **1b**, and **4a** that possess metal proportion in the spin density more than one can be expected to have dominant  $^3\text{MLCT}$  character in the phosphorescence emission.



**Figure 4.5** Spin density at the optimized  $T_1$  geometries for the Ir(III) complexes (isovalue = 0.002).

### 4.3 Absorption energies

Electronic transitions of singlet-singlet excitation were calculated at the optimized  $S_0$  geometries by including the solvent effect with PCM in  $\text{CH}_2\text{Cl}_2$  media. The simulated normalized absorption spectra of all complexes are plotted in **Figure 4.6**, and the selected singlet excited states in details including oscillator strength ( $f$ ), absorption energies, dominant contributions, and main characters are listed in **Table A10** associated with the experimental data<sup>32, 60</sup> of **1**, **1a** and **1b**. The calculated absorptions of **1** are in agreement with the experiment values in the range of 260–290 nm, but the calculation of absorption in lowest singlet absorption at 307 cannot reproduce the experiment absorption with extending to 335 nm. The difference between experiment and calculation for **1** is caused by the SOC effect to singlet-triplet

transition ignored in the calculation.<sup>32</sup> The calculated dominant peak in the low energy regions at 285 and 379 nm for **1a** and **1b** are also agreed with the experimental data at 304 and 375 nm, respectively. The calculation at the TD-PBE0 method could be reasonably applied for the rest complexes. The simulated absorption spectra have strong intensity at high energy and lower intensity at low energy. The lowest-lying singlet transition energy that is the vertical excitation energy from ground state ( $S_0$ ) to the first singlet excited state ( $S_1$ ) can be determined to evaluate shift of modified NHC Ir(III) complexes (see **Table A11–A14**). The calculated lowest-lying absorption of all modified complexes exhibit a red-shift in comparison with that of parent complex **1** because of more  $\pi$ -conjugation in the NHC ligand of the complexes. The lowest-lying absorption wavelengths follow the order of **1** (307 nm) < **1a** (326 nm) < **3a** (332 nm) < **4a** (340 nm) < **3b** (350 nm) < **2a** (355 nm) < **4b** (385 nm) < **1b** (390 nm) < **2b** (427 nm), which is nearly correlated with the order of HOMO-LUMO energy gaps in the previous part. The consistency in both orders is caused by the main contribution of HOMO  $\rightarrow$  LUMO in the  $S_0$ - $S_1$  transition for all complexes, which have MLCT (metal to ligand charge transfer), LLCT (ligand to ligand charge transfer) and IL (intraligand) characters.

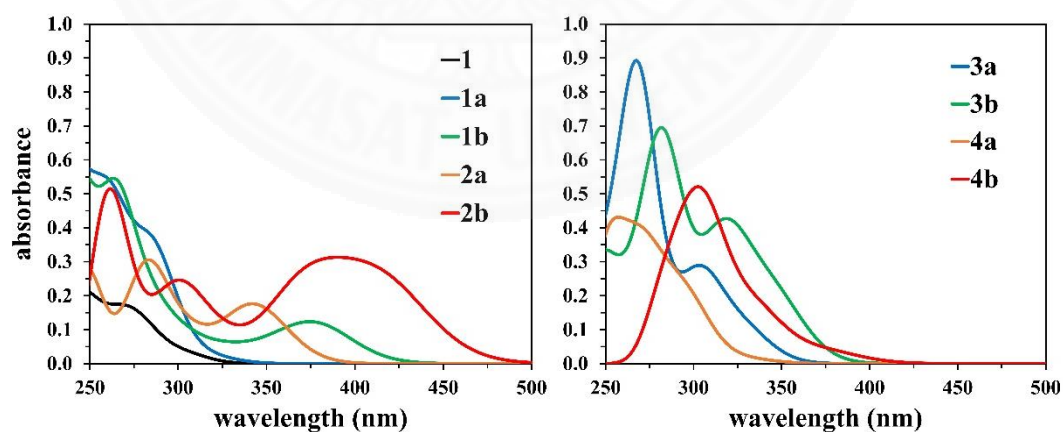


**Figure 4.6** Simulated absorption spectra of the complexes in  $\text{CH}_2\text{Cl}_2$  media (FWHM =  $3000\text{ cm}^{-1}$ ).

#### 4.4 Emission energies

Basis on the geometries of the triplet state, emission energies of the complexes were calculated via aforementioned three choices, which are  $E_{0-0}$  (PBE0),  $E_{\text{vert}}$  (PBE0), and  $E_{\text{TD}}$  (M06-2X). The  $E_{0-0}$  and  $E_{\text{vert}}$  with PBE0 functional that are  $\Delta\text{SCF}$  method have applied to predict the emission properties for similar systems. For TDDFT method, the emission energies were actually predicted by different functionals; B3LYP, CAM-B3LYP, PBE0, M05-2X, and M06-2X. All results of TDDFT calculations in the emission properties are represented in the **Figure 4.7**. The comparison between different functionals in TDDFT calculation and experiment shows the M06-2X functionals are the best one candidate in TDDFT method for comparing with the other methods ( $E_{0-0}$  and  $E_{\text{vert}}$ ). Each complex has similar emission characters although different functionals are used in the TDDFT method. The character of emission will be discussed later.

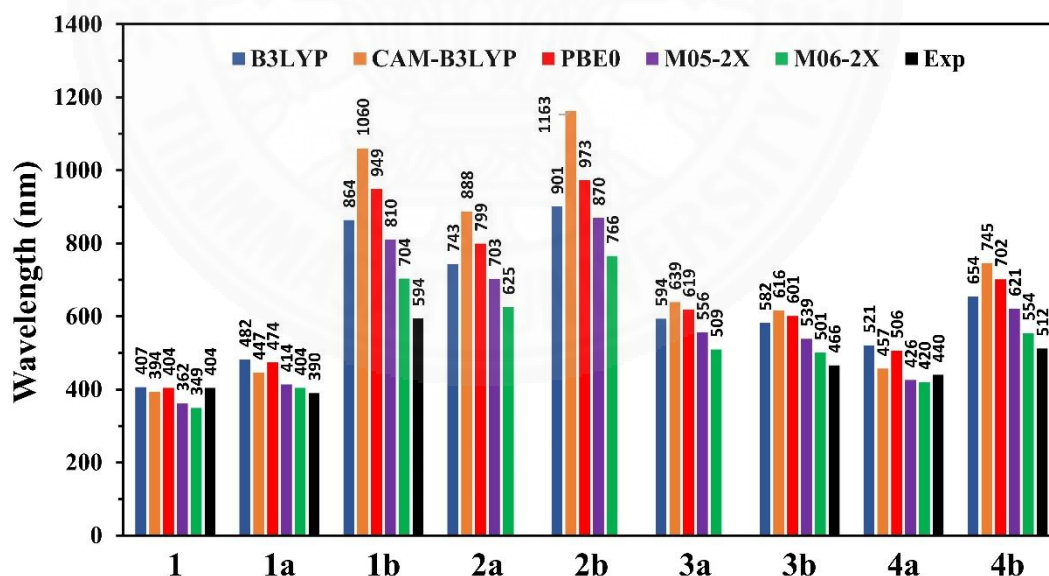


**Figure 4.7** Calculated lowest triplet energy wavelengths (nm) of TDDFT method with B3LYP, CAM-B3LYP, PBE0, M05-2X, and M06-2X functionals for all Ir(III) complexes associated with the experimental data<sup>32, 60</sup> of series **1**, **3b** and series **4**.

The lowest triplet energies in the different three ways of calculation are depicted in the **Figure 4.8** as bar graphs coupled with the experimental data of series **1**, **3b**, and series **4**. The vertical energies ( $E_{\text{vert}}$ ) of the complexes obviously overestimated prediction with respect to the experiment, while  $E_{0-0}$  and  $E_{\text{TD}}$  are better methods to predict the emissive triplet energies. The mean absolute error (MAE) in statistics that was used to evaluate difference between prediction and observation for quantitative analysis. The MAEs of  $E_{0-0}$ ,  $E_{\text{vert}}$ , and  $E_{\text{TD}}$  are 19.0, 100.1, and 45.9, respectively. The MAE of  $E_{0-0}$  are the smallest value; therefore, the  $E_{0-0}$  should be the best method to predict the emissive triplet energies for similar system of complexes unknown in the experiment. In addition, the  $R^2$  of  $E_{0-0}$  method was determined via correlation between the calculation and the experiment as shown in **Figure 4.9**, which displays the value up to 98.5%. Higher temperature clearly causes a red shift of the observed maximum emission wavelength for common Ir(III) complexes, so it should be match with the vertical transition or TDDFT transition. Conversely, in this case of the system, the calculated 0-0 transitions of the complexes are consistent with the experimental data in 298 K, implying that the phosphorescent emissions are mainly involved with low frequencies less than  $1000 \text{ cm}^{-1}$ .<sup>75</sup> Therefore, the displacement vectors of dominant normal modes in low frequencies should be the out-of-plane vibrations of the ligand and metal-ligand bonds/internal ligand vibrations.<sup>75</sup> The maximum emission wavelengths of the investigated Ir(III) complexes can be more endured the red shift produced by high temperature.

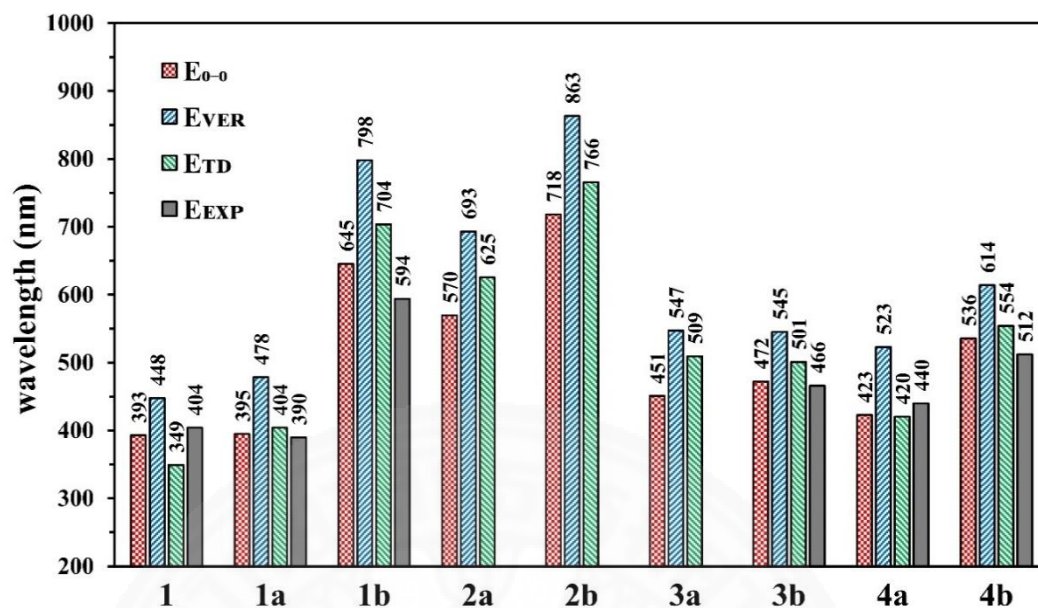


Figure 4.8 Calculated lowest triplet energy wavelengths (nm) for all Ir(III) complexes associated with the experimental data<sup>32, 60</sup> of series 1, 3b and series 4.

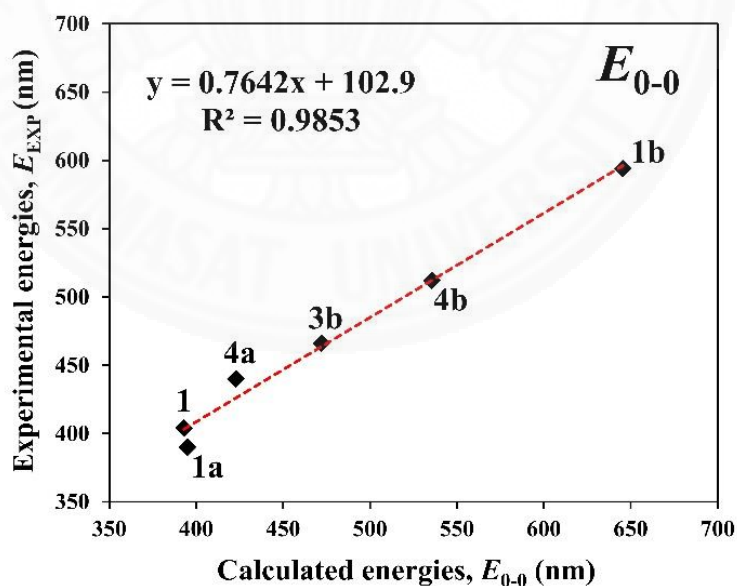


Figure 4.9 Correlation of calculated  $E_{0-0}$  and experimental emission energies (nm) for series 1, 3b and series 4.

From above reason, the 0-0 transition can be applied to compare among these complexes. The emission wavelength of **1b** are red-shifted to 645 nm with respect to **1** because of this position can stabilize the carbene moiety to lower the emission energy. Conversely, the emission wavelength of **1a** is almost the same as that of **1**, so it shows that the conjugation addition in this position not significantly affects the emission energy. However, the modifications of **1a** have an effect on the radiative rate constant, which they will be discussed in the next section. The modification by addition of bridging vinyl group on **1** and **1b** will be the **2a** and **2b**, respectively. The emission wavelength of the **2a** is red shifted from the **1** to 570 nm, and that of the **2b** is the lowest energies in the system by red shift from **1b** to be 718 nm. The bridging vinyl groups can permit more delocalization between phenyl and carbene moieties, resulting in stabilization of the triplet energies. Adjustments in structure of **1** with fluorene groups on phenyl moieties of the complex to **3a** and **3b**, the both have the red shift in emission in comparison with the **1**. The wavelength of **3b** is more red-shifted than that of **3a** because dimethyl-methylene group make hardly rotation of aryl ring. It leads to the higher electron delocalization that can stabilize the emissive triplet energy. The **3a** and **3b** show the wavelength of 451 and 472 nm, respectively, which are still the blue region of phosphorescence. Next, the **4a** are modification of **1a** to improve the quantum efficiency. The aryl group on carbene moiety in the **4a** causes red shift from 395 nm to 423 nm due to higher donating effect of aryl ring compared with that of methyl group. The increase of  $\pi$ -conjugation on the carbene moiety in the **4a** that is called the complex **4b** can be activated to be more red-shift to wavelength of 536 nm. The expansion of  $\pi$ -conjugation from **1** to **1a** does not affect the emission energies, but the secondary  $\pi$ -conjugation was modified on carbene moiety of **4b** providing a color change from blue (423 nm) to green (536 nm) emission in comparison with **4a**.

The transition characters of emission were obtained by TDDFT calculation based on the optimized  $T_1$  geometries. They are defined by electron density difference maps (EDDMs) between the first triplet state ( $T_1$ ) and the ground state ( $S_0$ ) at the optimized  $T_1$  geometry in dichloromethane solution displaying in **Figure 4.10**. In a wide



perspective, the hole (purple regions) are mostly distributed on the some NHC ligands and the Iridium atom, while the electron (turquoise regions) are mainly excited to one NHC ligand. In more details, the complex **1** has the excited electron on both phenyl and carbene moieties. Conjugated addition on the carbene moieties of **1a** and **1b** make the electron exciting to the carbene moiety on NHC ligand more than that of **1**. The bridging group of **2a** can induce the electron excitation to the whole of NHC ligand, whereas the character of **2b** is as same as that of **1b** due to the high conjugation on carbene moiety. The electrons are excited to the extended groups on phenyl moiety such in the **3a** and **3b**. The **4a** and **4b**, which are modification of the **1a**, has the same character as the **1a**. Consequently, the phosphorescence of the complexes is primarily derived from the intra-ligand  $\pi$ - $\pi^*$  transition of the NHC ligand ( $^3$ ILCT character) and some d orbital of Iridium atom to  $\pi^*$  orbital of the NHC ligands ( $^3$ MLCT character). These characters distinctly correspond to the spin density of  $T_1$  shown in **Figure 4.5**.

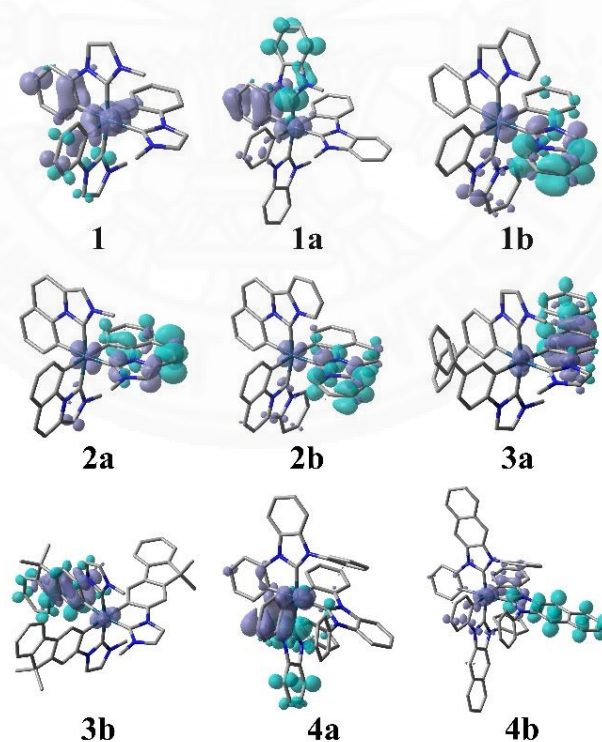


**Figure 4.10** Electron density difference maps (EDDMs) of the emission transition for all complexes (isovalue = 0.002). Purple and turquoise colors indicate regions of decrease and increase in electron density, respectively.

#### 4.5 Radiative decay

The radiative rate constants were calculated by TD-B3LYP with SOC treatment through linear and quadratic theories. First, the calculated radiative decay rates of *mer*-Ir(pmi)<sub>3</sub> (**1**), *mer*-Ir(pmb)<sub>3</sub> (**1a**), *fac*-Ir(pmi)<sub>3</sub>, and *fac*-Ir(pmb)<sub>3</sub> were performed on the optimized singlet and triplet geometries for testing the method appropriated with this system. To compare computation based on  $S_0$  and  $T_1$  geometries, the correlations between calculation and observation of the radiative rate constants were plotted in **Figure 4.11**. The R-squared of linear correlations show the values of 0.994 and 0.976 for  $S_0$  and  $T_1$  geometries, respectively. The result is consistent with the Minaev's work describing that the shallow minimum and anharmonicity potential surface of the  $T_1$  state causes low density of probability in vibrational wave function at the  $T_1$  geometry.<sup>56</sup> Commonly, the maximum density of probability of vibrational wave function for emissive triplet state is between the  $S_0$  and  $T_1$  structures.<sup>56, 76</sup> It is for this reason that the  $S_0$ - $T_1$  transition moments of the  $T_1$  geometry are quite smaller than those of the  $S_0$  geometry. Therefore, the observed radiative rates could be expected to close with the radiative rates at  $S_0$  geometry more than  $T_1$  geometry. From above rational explanation, the radiative rate constants of the rest complexes were performed at  $S_0$  geometry to precise prediction.

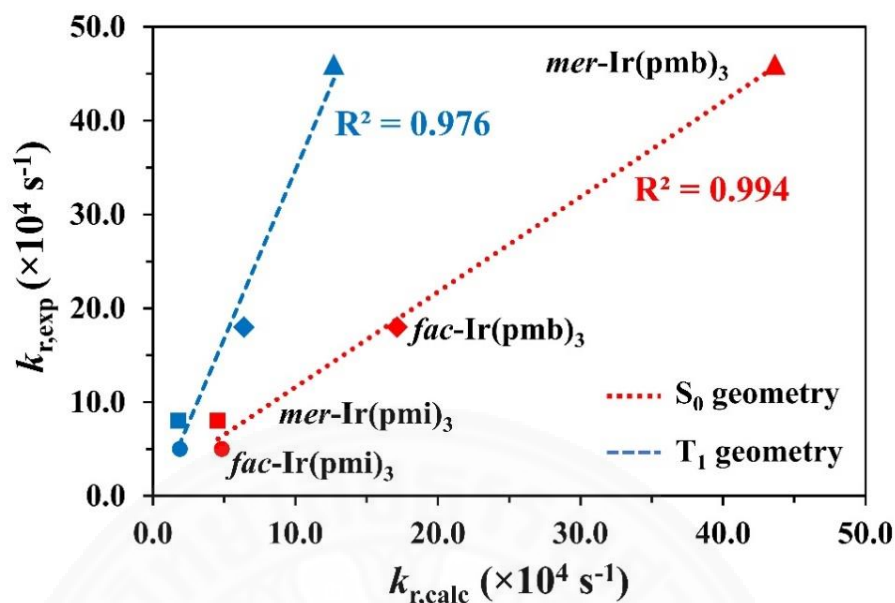


**Figure 4.11** Correlation of radiative rate constants between the experiment<sup>32, 78</sup> and the calculation based on the  $S_0$  and  $T_1$  geometries.

According to equation (4), the radiative rate constant strongly depends on the  $S_0$ - $T_1$  transition energy ( $E_{0-0}$ ) and transition moment ( $M$ ). The 0-0 transition from the previous could be applied to determine the  $S_0$ - $T_1$  transition energy, and transition moment was provided by averaged sublevels of lowest triplet state of transition moments ( $M_x$ ,  $M_y$ ,  $M_z$ ) defined as  $M_{ave}$ . The values of  $E_{0-0}$ ,  $M_{ave}$ , radiative rate constant ( $k_r$ ), and radiative lifetime ( $\tau_r$ ) are listed in the **Table 4.3**. The transition energies of **1** and **1a** are almost equal; however, the transition moment of **1a** are higher than **1** approximately three times. Thus, the transition moment with highest value directly leads to the highest radiative rate constant for the **1a**. The modification of **1b** shows the intensive decrease of both  $S_0$ - $T_1$  transition energy and transition moment resulting in the lower radiative rate of the **1b** compared with the **1**. The bridging vinyl groups modified in **2a** and **2b** distinctly depress the transition moment to the values of 0.024 and 0.023, respectively, leading to very small values in order of  $10^2$  for the radiative rate constants. More transition energy of the **2a** (2.18 eV) provides slightly higher  $k_r$  in comparison with that of **2b** (1.73 eV). Addition of fluorene groups in **3a** and **3b** makes lower transition energy and transition moment with respect to **1**.

Comparing between **3a** and **3b**, an increase of rigid ligand of dimethyl fluorenyl group in **3b** causes the lower transition energy and moment values than the **3a**; therefore, the  $k_r$  of **3b** ( $6.8 \times 10^3 \text{ s}^{-1}$ ) is less than that of **3a** ( $1.3 \times 10^3 \text{ s}^{-1}$ ). Complexes in series **4**, which are specific modification of **1a**, can be directly controlled by the  $\pi$ -conjugation on the carbene moieties as same as **1a**. The substitution of aryl groups of **4a** provides a small difference in transition moment with **1a**; however, the radiative rate constant of **4a** are significantly decrease due to its lower transition energy approximately 0.2 eV. The addition with high  $\pi$ -conjugation on the carbene moiety from **4a** to **4b** highly decreases the transition energy from 2.93 to 2.32 eV, in addition, extremely reduces about 3 times of transition moment to 0.086 Debye. The  $k_r$  of **4b** is still higher than those of **1b** and series **2** with low energy region emissions. Therefore, in the view of only calculation in the radiative rate constant, emission color adjustment in the system should be modified through the **1a** for higher radiative rate.

**Table 4.3**  $S_0$ - $T_1$  transition energy  $E_{0-0}$  (eV), averaged  $S_0$ - $T_1$  transition moment  $M_{\text{ave}}$  (Debye), radiative decay rate constants  $k_r$  ( $\text{s}^{-1}$ ), and radiative lifetime  $\tau_r$  ( $\mu\text{s}$ ) for the complexes.

	$E_{0-0}$	$M_{\text{ave}}^a$	$k_r$	$\tau_r^b$
<b>1</b>	3.15	0.094	$4.6 \times 10^4$	21.86
<b>1a</b>	3.14	0.29	$4.4 \times 10^5$	2.292
<b>1b</b>	1.92	0.048	$2.7 \times 10^3$	369.4
<b>2a</b>	2.18	0.024	$9.5 \times 10^2$	1058
<b>2b</b>	1.73	0.023	$4.7 \times 10^2$	2134
<b>3a</b>	2.75	0.063	$1.3 \times 10^4$	74.48
<b>3b</b>	2.63	0.048	$6.8 \times 10^3$	147.8
<b>4a</b>	2.93	0.26	$2.8 \times 10^5$	3.570
<b>4b</b>	2.32	0.086	$1.5 \times 10^4$	65.84

$$^a M_{\text{ave}} = \sqrt{(|M^x|^2 + |M^y|^2 + |M^z|^2)/3}$$

<sup>b</sup>  $\tau_r$  is the radiative lifetime in the high-temperature limit.

The  $S_0$ - $T_1$  transition moment is originally produced from perturbation theory according to the equation (5), which the second term is usually ignored due to relatively large energy gaps between the  $S_0$  and  $T_1$  states. The first term could be only considered to get more insight in the radiative processes of the complexes. The transition dipole moments, the SOC matrix elements, and the singlet-triplet splitting energies of each complex at their  $S_0$  geometries are listed in **Table A15–A18**. Although the modification from **1** to **1a** mostly causes decrease of the transition dipole moments and the SOC matrix elements, the singlet-triplet splitting energies of **1a** are the lowest values among the other complexes. Therefore, they mainly cause the highest radiative rate constant of the **1a**. The **1b**, **2a** and **2b** slightly provide difference of transition dipole moments and higher SOC matrix elements in some singlet states with respect to **1**, but they have critical low values of the radiative rate constants. The important reason is mainly involved in very high singlet-triplet splitting energies in range of 0.76–1.00 eV from  $S_1$  to  $S_6$  states (see **Figure 4.12**). The fluorene groups addition of **3a** and **3b** make higher singlet-triplet splitting energies and lower SOC matrix elements. They are crucial factors to obtain lower radiative rate than that of **1**, even though the transition dipole moments of **3a** and **3b** are quite higher than those of **1**. The **4a** modified from **1a** has lower radiative rate constant than that of **1a** caused by majority of singlet transition dipole moment, while singlet-triplet splitting energies and SOC matrix elements of both complexes are difficult to clearly distinguish. The  $\pi$ -conjugation extension of **4b** obviously affects increase of singlet-triplet splitting energies and decrease of SOC matrix elements with respect to **4a** leading to lower radiative rate constant in **4b**. Although transition dipole moments of **4b** are higher than those of **4a**, they are not main factor to determine the radiative rate constant. From above results, the singlet-triplet splitting energies and the SOC matrix elements are key factors to control the radiative rate constant, specially the  $S_1$ - $T_1$  splitting energies. Therefore, the relationship between the  $S_1$ - $T_1$  splitting energy and the radiative rate constant could be considered as represented in **Figure 4.13**.

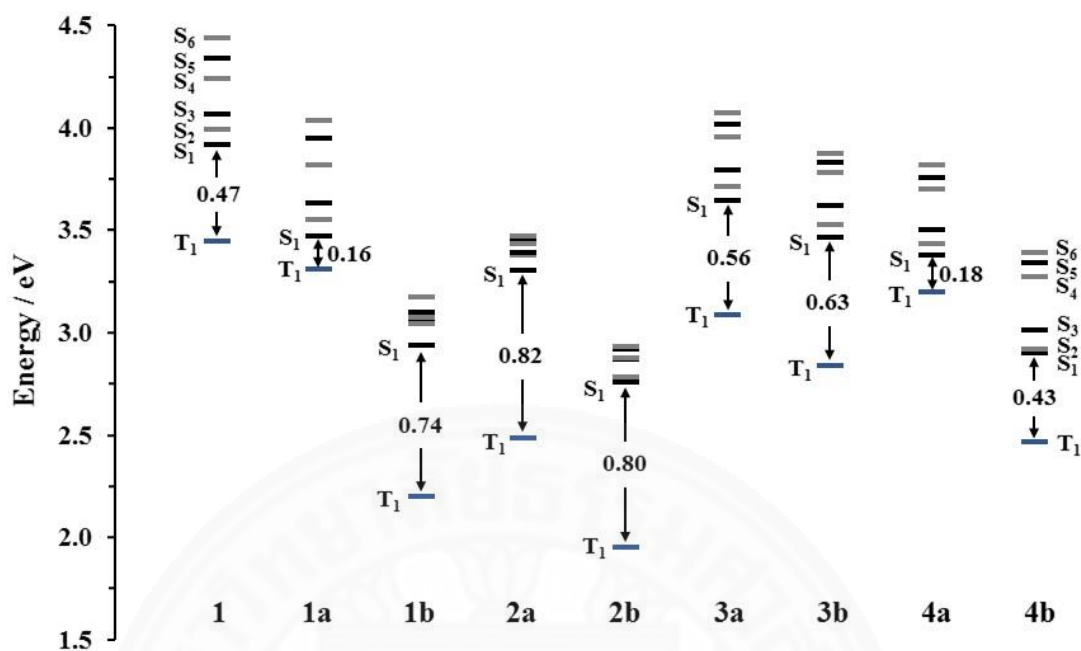


Figure 4.12 The splitting energies between lowest triplet state ( $T_1$ ) and higher singlet states ( $S_1$ - $S_6$ ) for all complexes.

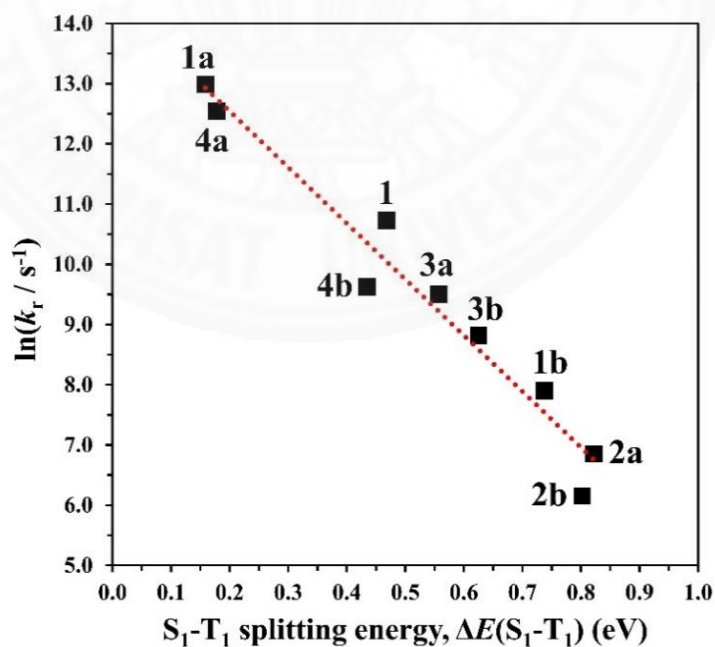


Figure 4.13 Radiative decay rate versus  $S_1$ - $T_1$  splitting energy for all complexes.

#### 4.6 Nonradiative decay of vibrational coupling to ground state

The nonradiative rate constant ( $k_{nr}$ ) following the energy-gap law is determined by deformation of structure between  $S_0$  and  $T_1$  states in the weak coupling condition. The Huang-Rhys factor that defines the molecular deformation was thus calculated for all complexes.<sup>72, 75</sup> The necessary parameters in  $k_{nr}$  determination following equation (8) are listed in **Table 4.4**. The **1**, **1a**, **3a** and **4a** have significant structural deformations, which they cause a large Duschinsky effect leading to unreliable Huang-Rhys factors and reorganization energies. Because the parameters of Huang-Rhys factor and reorganization energies are distinctly incorrect, the non-radiative rate constants could not be determined for **1**, **1a**, **3a** and **4a**. The rest complexes that have more  $\pi$ -conjugations in the ligand skeletons normally display low structural distortion between  $S_0$  and  $T_1$  states allowing weak coupling limit. The calculated  $k_{nr}$  in the order **1b** > **2b** > **4b** > **2a** > **3b** at 298 K inversely relate to the 0-0 transition energies with sequence of **2b** < **1b** < **2a** < **4b** < **3b**. The  $k_{nr}$  of **1b** is more than that of **2b** about 2 times due to the major effect of both structural reorganization energy and SOC constant. Although the higher  $E_{0-0}$  and the lower  $\lambda_v$  of **4b** should effectively make the higher  $k_{nr}$  more than that of **2a**, the large SOC constant of **4b** is main factor to bring about the higher  $k_{nr}$ . The SOC matrix elements, which play important role to the non-radiative rate constant, show extremely high values in **1a** and **4a**. Therefore, the complexes of **1a** and **4a** have a tendency to provide the strong non-radiative rate decay. The complexes of **1**, **1a**, **3a** and **4a** being not available on  $k_{nr}$  have quite big  $E_{0-0}$  resulting in low vibrational coupling to their ground states. They have more <sup>3</sup>MLCT character of excited state causing higher reorganization energy in low-frequency modes ( $\lambda_{lf}$ ). The  $\lambda_{lf}$  has more influence on the non-radiative rate constant when increased temperature; however, this parameter of **1**, **1a**, **3a** and **4a** are not available in the energy-gap law. The temperature dependence of  $k_{nr}$  for these complexes is usually describe to the presence of thermal population in the <sup>3</sup>d-d excited state.

**Table 4.4** Calculated 0-0 transition energies ( $E_{0-0}$ ,  $\text{cm}^{-1}$ ), Huang-Rhys factors of the hf ( $S_M$ ) and lf ( $S_{lf}$ ) modes, reorganization energies ( $\text{cm}^{-1}$ ) of the hf ( $\lambda_M$ ) and lf ( $\lambda_{lf}$ ) modes, intramolecular reorganization energies ( $\lambda_v$ ), values of  $\langle S_0 | H_{S_0} | T_1 \rangle^2$  ( $\text{cm}^{-2}$ ), and calculated  $k_{nr}$  ( $\text{s}^{-1}$ ) at 298 K for the Ir(III) complexes.

	$E_{0-0}$	$S_M$	$S_{lf}$	$\lambda_M$	$\lambda_{lf}$	$\lambda_v^a$		$\langle S_0   H_{S_0}   T_1 \rangle^2$	$k_{nr}$ (298 K)
						FC	SS		
<b>1</b>	25448	2.10	5.87	n/a <sup>b</sup>	n/a <sup>b</sup>	n/a <sup>b</sup>	3113	3505.49	n/a <sup>b</sup>
<b>1a</b>	25324	2.23	17.0	n/a <sup>b</sup>	n/a <sup>b</sup>	n/a <sup>b</sup>	4420	15029.6	n/a <sup>b</sup>
<b>1b</b>	15495	1.89	1.23	2845	383	3235	2964	275.914	$5.50 \times 10^6$
<b>2a</b>	17559	1.97	1.40	2940	355	3420	3127	13.4736	$2.28 \times 10^4$
<b>2b</b>	13927	1.51	1.35	2296	380	2680	2342	101.191	$2.56 \times 10^6$
<b>3a</b>	22192	16.3	46.1	n/a <sup>b</sup>	n/a <sup>b</sup>	n/a <sup>b</sup>	3904	680.495	n/a <sup>b</sup>
<b>3b</b>	21187	1.57	1.34	2413	669	3084	2842	704.412	$3.93 \times 10^3$
<b>4a</b>	23653	2.60	53.5	n/a <sup>b</sup>	n/a <sup>b</sup>	n/a <sup>b</sup>	4526	121104	n/a <sup>b</sup>
<b>4b</b>	18674	1.38	2.28	2076	413	2491	2383	1669.35	$2.99 \times 10^4$

<sup>a</sup>  $\lambda_v$  was obtained from different two ways including Frank-Condon (FC) and state specific (SS).

<sup>b</sup> Huang-Rhys factors of the complexes is not reliable, so it could not be used to calculate the reorganization energies and the nonradiative rate constants.

#### 4.7 Non-radiative decay of thermal population on metal-centered state

The temperature dependence non-radiative decay is photodeactivation process from the emissive triplet state (<sup>3</sup>MLCT) to the *d-d* state or the metal center (<sup>3</sup>MC) state, which continuously relaxes to the ground state without radiative decay.<sup>102</sup> The pathway naturally occurs in the high energy of emissive triplet state for the Ir(III) complexes at ambient temperature. The <sup>3</sup>MC states of the complexes are thus necessary to investigation of the deactivation pathway. The structural geometries of <sup>3</sup>MC states were optimized from starting geometry created by breaking Ir-C<sub>carbene</sub> bond and rotating the carbene moiety to 90° of dihedral angle relative to the phenyl moiety. The five-coordinate species of <sup>3</sup>MC geometries could be obtained, and clearly show a



distorted trigonal bipyramid (TBP) as displayed in **Figure 4.14**. The breaking Ir-C<sub>carbene</sub> bond of the complexes that listed in **Table 4.5** is over 3.000 Å but those of **2a** and **2b**. This bond directly relates with the dihedral angle between phenyl and carbene moieties of the monodentate ligand showing more than 50° except those of **2a** and **2b** (ca. 10°). The vinyl bridging ligands in **2a** and **2b** cause more rigid in the ligands leading to little rotation of the dihedral angle and shorten distance of breaking Ir-C<sub>carbene</sub> relative to that of the other complexes. Conversely, the steric effect of **4a** and **4b** affects the <sup>3</sup>MC geometries by larger Ir-C<sub>carbene</sub> (> 3.800 Å) and higher dihedral angle rotation between phenyl and carbene moieties for the monodentate ligand. The <sup>3</sup>MC structures of **4a** and **4b** could not be optimized by breaking Ir-C<sub>carbene</sub> bond of the NHC1 ligand due to the steric effect of aryl group on the carbene moiety. Although the geometries of <sup>3</sup>MC could be obtained from the breaking bond of the NHC2 ligand instead of the NHC1 ligand, the structure and density of this state should be expected to the same. The calculated spin densities of the TBP geometry that are distributed along the equatorial plane for all complexes as depicted in **Figure A1** are mainly localized on the Iridium atom in accordance with the nature of <sup>3</sup>MC state.

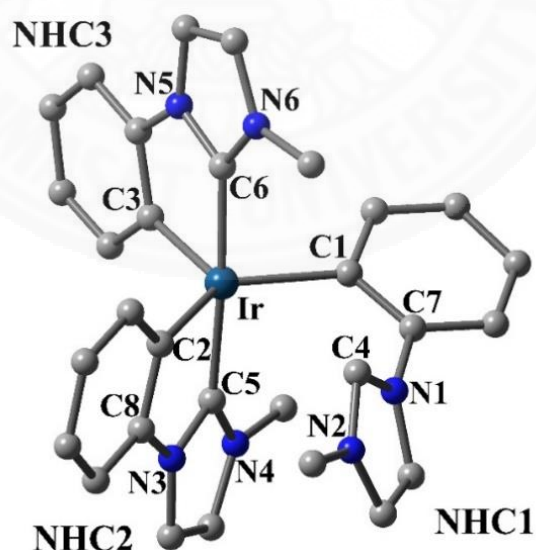


**Figure 4.14** Optimized <sup>3</sup>MC geometry of **1** by elongation of Ir-C4 bond length.

**Table 4.5** Structural parameters including bond lengths (Å), bond angles (°), and dihedral angles (°) of  $^3\text{MC}$  state for the complexes.

	<b>1</b>	<b>1a</b>	<b>1b</b>	<b>2a</b>	<b>2b</b>	<b>3a</b>	<b>3b</b>	<b>4a</b>	<b>4b</b>
Ir-C1	2.085	2.088	2.082	2.096	2.101	2.085	2.087	2.026	2.023
Ir-C2	2.053	2.046	2.050	2.076	2.068	2.053	2.052	2.072	2.071
Ir-C3	2.060	2.046	2.058	2.104	2.094	2.059	2.060	2.067	2.068
Ir-C4	3.347	3.358	3.336	2.994	2.895	3.364	3.341	2.045	2.040
Ir-C5	2.018	2.010	2.017	2.037	2.032	2.019	2.017	3.828	3.810
Ir-C6	2.022	2.012	2.015	2.030	2.029	2.024	2.022	2.014	2.012
C1-Ir-C2	131.71	131.18	131.59	138.28	139.64	130.66	132.04	123.82	123.41
C2-Ir-C3	118.37	116.98	118.89	116.51	117.76	119.03	117.64	86.10	85.69
C1-C7- N1-C4	-52.79	-55.19	-54.30	-10.15	-11.4	-53.18	-52.46	80.99	80.07

The temperature dependence deactivation pathways of the complexes are depicted in **Figure 4.15**, which start with the  $^3\text{MLCT}$  of octahedral geometry. The process has two energy barriers, which are transition state ( $^3\text{TS}$ ) ( $^3\text{MLCT}/^3\text{MC}$ ) and minimum energy crossing point (MECP) ( $^3\text{MC}$  and  $S_0$ ). The energy of  $^3\text{MLCT}$  state ( $E_{0-0}$ ) can be varied by the modified ligand in wider range than the energy of  $^3\text{MC}$  state ( $E_{\text{MC}}$ ) because the  $^3\text{MC}$  state involves the metal distribution more than ligand. Therefore, the modifications of ligand of the complexes have less effect on the energies of  $^3\text{MC}$  states. The important parameters of deactivation pathway are listed in **Table 4.6**, which show the energy barriers including  $E_a$ ,  $E_b$ , and  $E_c$  defined in **Figure 3.2**. The  $E_a$  is significantly higher than the  $E_c$ , so the energy barrier between  $^3\text{MLCT}$  state and  $^3\text{MC}$  state is rate-limiting step of the process for all complexes. The  $E_a$  is gradually increased with decrease in the  $E_{0-0}$  as plotting in **Figure 4.16a**, indicating that the barrier energy of  $^3\text{TS}$  states strongly depends on the  $E_{0-0}$ . The **4b**, **2a**, **1b** and **2b** that have emission color from green to red are thus inaccessible to thermal population at the ambient temperature. The lowest  $E_a$  of **1a** that is just 2.11 kcal/mol effectively affects the

thermal deactivation at room temperature. This calculated result is consistent with the experiment with a very high  $k_{nr}$  at 298 K ( $65 \times 10^6 \text{ s}^{-1}$ ).<sup>32</sup> The **3a**, **3b** and **4a** still being blue phosphors have the  $E_a$  over 15.00 kcal/mol; therefore, temperature dependent  $k_{nr}$  of these complexes is efficiently reduced to improve the quantum efficiency.

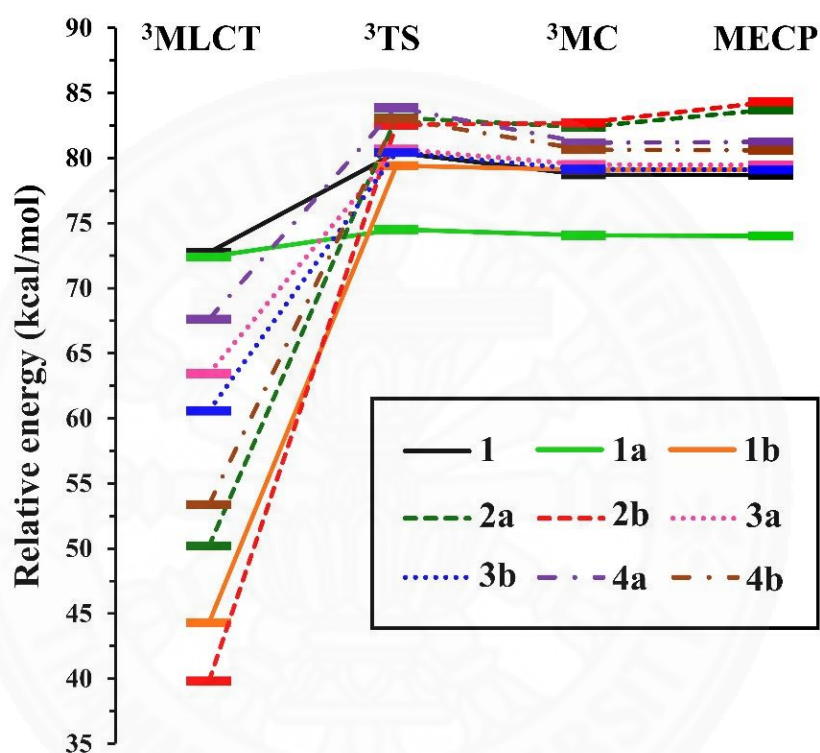


**Figure 4.15** Relative energy profile of temperature-dependent non-radiative pathways through <sup>3</sup>MC state for all complexes. The reference is the ground state.

**Table 4.6** Emission energy  $E_{0-0}$  and activation energy  $E_a$ ,  $E_b$  and  $E_c$  (kcal/mol) of the metal-centered state decay for all complexes.

	$E_{0-0}$	$E_{MC}$	$E_a$	$E_b$	$E_c$
1	72.76	78.72	7.66	1.70	-0.03
1a	72.40	74.05	2.11	0.46	-0.04
1b	44.30	79.10	35.11	0.32	0.01
2a	50.20	82.38	32.89	0.72	1.35
2b	39.82	82.70	42.73	-0.16	1.62
3a	63.45	79.50	17.23	1.18	-0.06
3b	60.58	79.15	19.85	1.28	-0.05
4a	67.63	81.18	16.25	2.70	0.07
4b	53.39	80.64	29.63	2.38	-0.05

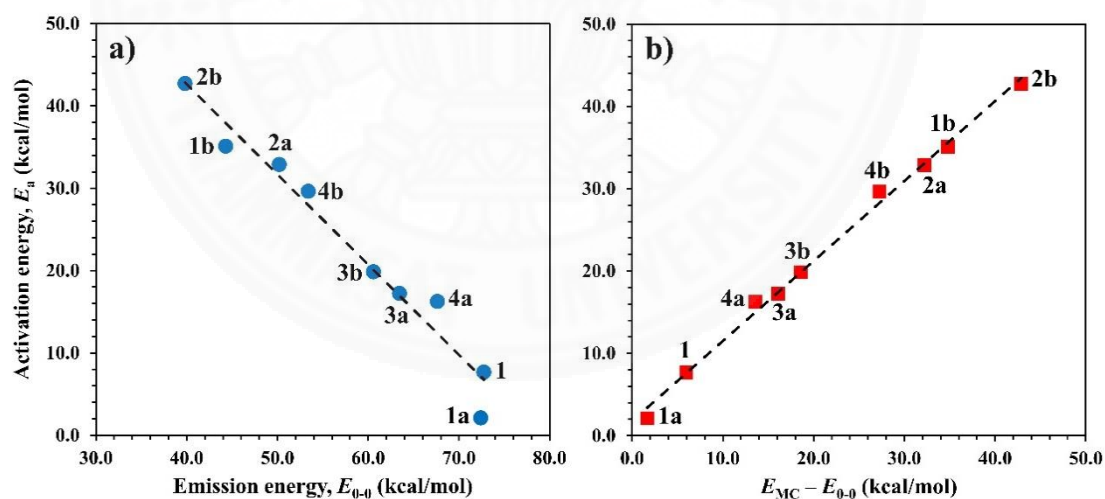


**Figure 4.16** Plot of a) the emission energy ( $E_{0-0}$ ) versus the activation energy ( $E_a$ ) and b) the energy difference between MC state and MLCT state ( $E_{MC}-E_{0-0}$ ) versus the activation energy for all complexes.

The energy difference between  $E_{MC}$  and  $E_{0-0}$  is equally increased together with the  $E_a$  plotted in **Figure 4.16b** indicating that the energy of  $^3TS$  state is slightly different with that of  $^3MC$  state. In other words, the activation energy of  $E_a$  is steadily decreased as the energy of  $^3MLCT$  state ( $E_{0-0}$ ) gradually increased relative to the energy of  $^3MC$  state. The population on the  $^3MC$  state, the  $E_b$  and  $E_c$  become important parameters to consider the path of back transition to the ground state. The  $E_b$  that is difference between the energy of  $^3TS$  and  $^3MC$  presents small value within 2.70 kcal/mol for all complexes. The spin density of  $^3TS$  state has more distribution on the Iridium atom than those of  $^3MLCT$  state for all complexes as displayed in **Figure A2**. Although the low energy of  $E_b$  can make the back reaction to the  $^3MLCT$  state, the  $E_c$  of most complexes except **1a** and **1b** are almost zero or less than zero leading to fast relaxation to ground state. When the  $^3MC$  state is thermally accessed, the complexes will rapidly relax by intersystem crossing through MECP to the ground state. Some complexes found on **2a** and **2b**, the  $E_c$  is more than the  $E_b$  indicating the back reaction to the  $^3MLCT$  can be occasionally occurred. Nevertheless, the population on  $^3MC$  state of **2a** and **2b** is quite neglected due to extremely high  $E_a$ . Adjustment of the ligands by  $\pi$ -conjugated addition can inhibit the thermal deactivation process, but emission energy will be altered to lower energy.

#### 4.8 Quantum yield calculation

Phosphorescent quantum yield could be calculated according to equation (3) which depends on both radiative and nonradiative rate constants. Naturally, the nonradiative rates of green and red phosphors mainly depend on temperature-independence, following the energy-gap law<sup>90-91</sup>, while those of blue phosphor are predominantly affected by temperature-dependent pathway through  $^3MC$  state.<sup>100, 102</sup> As **Table 4.7**, the green phosphor (**4b**) has moderate quantum yield of 0.33, whereas the red phosphors have very low quantum yield of lower than 0.05. The quantum yield of **4b** as blue phosphor show good quantum yield with value of 0.63. For other blue phosphors (**1**, **1a**, **3a**, and **4a**), their quantum yields could not be achieved

because the nonradiative cannot be directly obtained from equation (8). If one can be determined the pre-exponential factor and activation energy ( $E_a$ ) in equation (16), the temperature-dependent nonradiative rate will be directly obtained by Arrhenius equation. Unfortunately, the calculation of pre-exponential factor is quite difficult because it involves nonadiabatic transition of MECP state. Therefore, pre-exponential factor can be defined as rate constant of  $^3MC$  state to  $S_0$ . There is one report to indirectly predict the quantum yield from activation energy.<sup>80</sup> However, this protocol must have the reference values from the  $Ir(ppy)_3$  to predict the quantum yield as same as the experimental method.<sup>80</sup> Therefore, the prediction of quantum yield of blue phosphor could be considered to a further work.

**Table 4.7** Summary of phosphorescent quantum efficiencies of the complexes.

	$\lambda_{em}$ (nm)	Expected colour	$k_r$ ( $\times 10^4 s^{-1}$ )	$k_{nr}$ ( $\times 10^4 s^{-1}$ )	$E_a$ (kcal/mol)	Quantum yield
<b>1</b>	393	Near-UV	4.6	n/a	7.66	n/a
<b>1a</b>	395	Near-UV	44	n/a	2.11	n/a
<b>1b</b>	645	Red	0.27	550	35.1	0.00049
<b>2a</b>	570	Yellow	0.095	2.28	32.9	0.040
<b>2b</b>	718	Red	0.047	256	42.7	0.00018
<b>3a</b>	451	Blue	1.3	n/a	17.2	n/a
<b>3b</b>	472	Blue	0.68	0.393	19.8	0.63
<b>4a</b>	423	Blue	28	n/a	16.2	n/a
<b>4b</b>	536	Green	1.5	2.99	29.6	0.33

## CHAPTER 5

### CONCLUSIONS AND RECOMMENDATIONS

The homoleptic Iridium(III) complexes with modified *N*-heterocyclic carbene ligands were investigated by DFT and TDDFT methods for simultaneously obtaining wide-range emission colors and improving quantum efficiency. The extended  $\pi$ -electron delocalization on the carbene moiety in NHC ligands more affect the bond length contraction between metal atom and ligand than the modification on the phenyl moiety in NHC ligands. Energy gaps of the Iridium(III) complexes obviously depend on the LUMO energies because the modified NHC in the complexes have not significant influence on the HOMO energies. The absorption spectra of the modified NHC Iridium(III) complexes show a red-shift with respect to that of parent complex (**1**). The emission energies of the complexes calculated by different three methods that are  $E_{0-0}$ ,  $E_{\text{vert}}$ , and  $E_{\text{TD}}$ . The method of  $E_{0-0}$  can precisely evaluate emission wavelength with respect to the observed wavelength, while the  $E_{\text{vert}}$  and the  $E_{\text{TD}}$  methods overestimate the value of experiment. The  $\pi$ -conjugated addition on the phenyl moiety in NHC ligands can achieve a blue phosphorescence, while the modification on the carbene moiety can adjust from blue to red emission. The radiative rate constant of these complexes extremely depends on the  $S_1$ - $T_1$  splitting energy. The **1a** and complexes in series **4** (**4a** and **4b**) that modified from the **1a** have the higher radiative rate than other complexes. The nonradiative rate following the energy-gap law in the weak coupling conditions inversely correlates with the emission energy for the complexes. However, this nonradiative rate cannot describe the complexes that have severe structural deformation (**1**, **1a**, **3a** and **4a**). This can be solved by additional determination of the photo-deactivation pathway from the  $^3\text{MLCT}$  to  $S_0$  through  $^3\text{MC}$ , which is temperature dependence non-radiative decay, to clearly realize the quenching of all complexes. The activation energy of  $^3\text{TS}$  ( $E_a$ ) is the rate-limiting step in the process, and it linearly depends on the  $^3\text{MLCT}$  energy ( $E_{0-0}$ ). The complexes that show green to red emission (**4b**, **2a**, **1b** and **2b**) can certainly inhibit the thermal population of  $^3\text{MC}$  at the ambient temperature. Conversely, the complexes of **3a**, **3b**

and **4a** still produce blue emission, but they can quite avoid thermal accessible quenching for quantum efficiency improvement. The extended  $\pi$ -conjugation on the NHC ligand makes the efficient blue to green phosphors, but extremely low quantum yields were found in the red phosphors.

For further investigation, first, the modification of NHC ligand should be performed through the **1a** for increasing the radiative rate constant. For example, the  $\pi$ -conjugation on the phenyl moiety should be modified via complex **1a** shown as **Figure 4.17**. The **L1** and **L2** are expected to blue phosphors with higher radiative rates. A higher quantum yield of red phosphor can be provided by molecular design as a **L3**. Next, the bridging group in the ligand should be non-conjugated system to increase the radiative rate and to decrease the nonradiative rate according to energy-gap law. Additionally, this modification can be expected to higher emission energies as **L4** and **L5**. Finally, the ligand should be further investigated as ancillary ligand together with the main phenylpyridinyl (ppy) ligand in heteroleptic Ir(III) complexes.

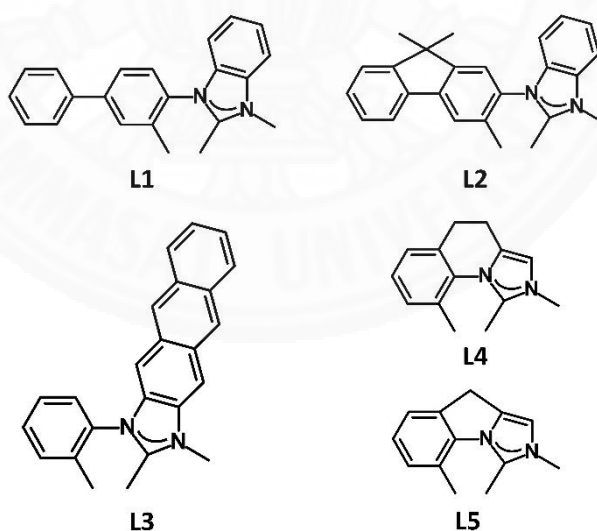


**Figure 5.1** Further modified NHC ligands to improve the quantum efficiency.



## REFERENCES

1. Chi, Y.; Chou, P. T., *Chem. Soc. Rev.* **2010**, *39* (2), 638-55.
2. Di Marco, G.; Lanza, M.; Mamo, A.; Stefio, I.; Di Pietro, C.; Romeo, G.; Campagna, S., *Anal. Chem.* **1998**, *70* (23), 5019-5023.
3. Amao, Y.; Ishikawa, Y.; Okura, I., *Anal. Chim. Acta* **2001**, *445* (2), 177-182.
4. DeRosa, M. C.; Mosher, P. J.; Yap, G. P. A.; Focsaneanu, K. S.; Crutchley, R. J.; Evans, C. E. B., *Inorg. Chem.* **2003**, *42* (16), 4864-4872.
5. Lo, K. K.-W.; Chung, C.-K.; Lee, T. K.-M.; Lui, L.-H.; Tsang, K. H.-K.; Zhu, N., *Inorg. Chem.* **2003**, *42* (21), 6886-6897.
6. Silavwe, N. D.; Goldman, A. S.; Ritter, R.; Tyler, D. R., *Inorg. Chem.* **1989**, *28* (7), 1231-1236.
7. Demas, J. N.; Harris, E. W.; Flynn, C. M.; Diemente, D., *J. Am. Chem. Soc.* **1975**, *97* (13), 3838-3839.
8. Demas, J. N.; Harris, E. W.; McBride, R. P., *J. Am. Chem. Soc.* **1977**, *99* (11), 3547-3551.
9. Gao, R.; Ho, D. G.; Hernandez, B.; Selke, M.; Murphy, D.; Djurovich, P. I.; Thompson, M. E., *J. Am. Chem. Soc.* **2002**, *124* (50), 14828-14829.
10. Parker, S. T.; Slinker, J. D.; Lowry, M. S.; Cox, M. P.; Bernhard, S.; Malliaras, G. G., *Chem. Mater.* **2005**, *17* (12), 3187-3190.
11. Bolink, H. J.; Cappelli, L.; Coronado, E.; Parham, A.; Stössel, P., *Chem. Mater.* **2006**, *18* (12), 2778-2780.
12. Nazeeruddin, M. K.; Wegh, R. T.; Zhou, Z.; Klein, C.; Wang, Q.; De Angelis, F.; Fantacci, S.; Grätzel, M., *Inorg. Chem.* **2006**, *45* (23), 9245-9250.
13. Su, H. C.; Fang, F. C.; Hwu, T. Y.; Hsieh, H. H.; Chen, H. F.; Lee, G. H.; Peng, S. M.; Wong, K. T.; Wu, C. C., *Adv. Funct. Mater.* **2007**, *17* (6), 1019-1027.
14. Baldo, M. A.; O'Brien, D. F.; You, Y.; Shoustikov, A.; Sibley, S.; Thompson, M. E.; Forrest, S. R., *Nature* **1998**, *395* (6698), 151-154.
15. Adachi, C.; Baldo, M. A.; Thompson, M. E.; Forrest, S. R., *J. Appl. Phys.* **2001**, *90* (10), 5048-5051.

16. Yersin, H.; Rausch, A. F.; Czerwieniec, R.; Hofbeck, T.; Fischer, T., *Coord. Chem. Rev.* **2011**, *255* (21-22), 2622-2652.
17. Hofbeck, T.; Yersin, H., *Inorg. Chem.* **2010**, *49* (20), 9290-9.
18. Hay, P. J., *J. Phys. Chem. A* **2002**, *106* (8), 1634-1641.
19. You, Y.; Nam, W., *Chem. Soc. Rev.* **2012**, *41* (21), 7061-84.
20. Gildea, L. F.; Williams, J. A. G., 3 - Iridium and platinum complexes for OLEDs A2 - Buckley, Alastair. In *Organic Light-Emitting Diodes (OLEDs)*, Woodhead Publishing: 2013; pp 77-113.
21. Goldstein, D. C.; Cheng, Y. Y.; Schmidt, T. W.; Bhadbhade, M.; Thordarson, P., *Dalton Trans.* **2011**, *40* (9), 2053-2061.
22. Leslie, W.; Batsanov, A. S.; Howard, J. A. K.; Gareth Williams, J. A., *Dalton Trans.* **2004**, (4), 623-631.
23. Liu, T.; Zhang, H.-X.; Xia, B.-H., *J. Organomet. Chem.* **2008**, *693* (6), 947-956.
24. Tang, K.-C.; Liu, K. L.; Chen, I. C., *Chem. Phys. Lett.* **2004**, *386* (4), 437-441.
25. Hedley, G. J.; Ruseckas, A.; Samuel, I. D. W., *Chem. Phys. Lett.* **2008**, *450* (4), 292-296.
26. Li, J.; Djurovich, P. I.; Alleyne, B. D.; Yousufuddin, M.; Ho, N. N.; Thomas, J. C.; Peters, J. C.; Bau, R.; Thompson, M. E., *Inorg. Chem.* **2005**, *44* (6), 1713-1727.
27. Dixon, I. M.; Collin, J.-P.; Sauvage, J.-P.; Flamigni, L.; Encinas, S.; Barigelletti, F., *Chem. Soc. Rev.* **2000**, *29* (6), 385-391.
28. Kim, S.-Y.; Kim, J.-H.; Ha, Y.; Lee, S.-H.; Seo, J.-H.; Kim, Y.-K., *Curr. Appl. Phys.* **2007**, *7* (4), 380-383.
29. Dedeian, K.; Shi, J.; Forsythe, E.; Morton, D. C.; Zavalij, P. Y., *Inorg. Chem.* **2007**, *46* (5), 1603-1611.
30. Abrahamsson, M.; Lundqvist, M. J.; Wolpher, H.; Johansson, O.; Eriksson, L.; Bergquist, J.; Rasmussen, T.; Becker, H.-C.; Hammarström, L.; Norrby, P.-O.; Åkermark, B.; Persson, P., *Inorg. Chem.* **2008**, *47* (9), 3540-3548.
31. Tamayo, A. B.; Alleyne, B. D.; Djurovich, P. I.; Lamansky, S.; Tsyba, I.; Ho, N. N.; Bau, R.; Thompson, M. E., *J. Am. Chem. Soc.* **2003**, *125* (24), 7377-7387.

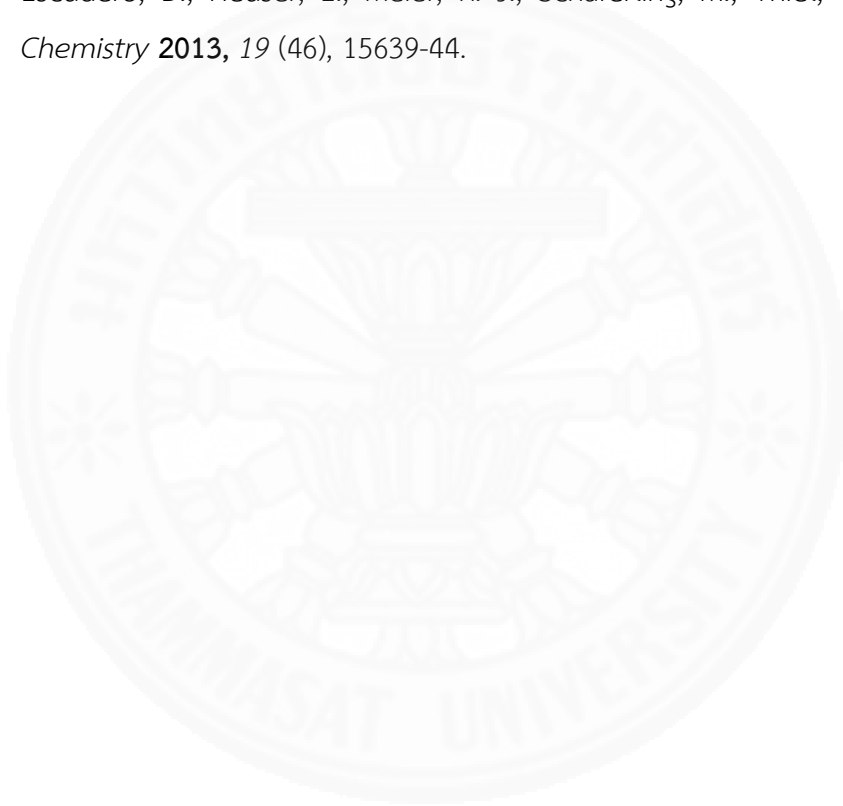
32. Sajoto, T.; Djurovich, P. I.; Tamayo, A.; Yousufuddin, M.; Bau, R.; Thompson, M. E.; Holmes, R. J.; Forrest, S. R., *Inorg. Chem.* **2005**, *44* (22), 7992-8003.
33. Hahn, F. E.; Jahnke, M. C., *Angew. Chem. Int. Ed.* **2008**, *47* (17), 3122-3172.
34. Fortman, G. C.; Nolan, S. P., *Chem. Soc. Rev.* **2011**, *40* (10), 5151-5169.
35. Mercs, L.; Albrecht, M., *Chem. Soc. Rev.* **2010**, *39* (6), 1903-12.
36. Holmes, R. J.; Forrest, S. R.; Sajoto, T.; Tamayo, A.; Djurovich, P. I.; Thompson, M. E.; Brooks, J.; Tung, Y. J.; D'Andrade, B. W.; Weaver, M. S.; Kwong, R. C.; Brown, J. J., *Appl. Phys. Lett.* **2005**, *87* (24), 243507.
37. You, Y.; Park, S. Y., *Dalton Trans.* **2009**, (8), 1267-1282.
38. Chi, Y.; Chou, P.-T., *Chem. Soc. Rev.* **2010**, *39* (2), 638-655.
39. Runge, E.; Gross, E. K. U., *Phys. Rev. Lett.* **1984**, *52* (12), 997-1000.
40. Becke, A. D., *J. Chem. Phys.* **1993**, *98* (7), 5648-5652.
41. Vlček Jr, A.; Zális, S., *Coord. Chem. Rev.* **2007**, *251* (3-4), 258-287.
42. Bauernschmitt, R.; Ahlrichs, R., *Chem. Phys. Lett.* **1996**, *256* (4-5), 454-464.
43. Furche, F.; Ahlrichs, R., *J. Chem. Phys.* **2004**, *121* (24), 12772-12773.
44. Fantacci, S.; De Angelis, F.; Selloni, A., *J. Am. Chem. Soc.* **2003**, *125* (14), 4381-4387.
45. Crescenzi, O.; Pavone, M.; De Angelis, F.; Barone, V., *J. Phys. Chem. B* **2005**, *109* (1), 445-453.
46. Miertuš, S.; Scrocco, E.; Tomasi, J., *Chem. Phys.* **1981**, *55* (1), 117-129.
47. Klamt, A.; Schuurmann, G., *J. Chem. Soc., Perk. Trans. 2* **1993**, (5), 799-805.
48. van Lenthe, E.; Snijders, J. G.; Baerends, E. J., *J. Chem. Phys.* **1996**, *105* (15), 6505-6516.
49. Smith, A. R. G.; Burn, P. L.; Powell, B. J., *Chem. Phys. Chem.* **2011**, *12* (13), 2429-2438.
50. Smith, A. R.; Riley, M. J.; Burn, P. L.; Gentle, I. R.; Lo, S. C.; Powell, B. J., *Inorg. Chem.* **2012**, *51* (5), 2821-31.
51. Song, M.-X.; Hao, Z.-M.; Wu, Z.-J.; Song, S.-Y.; Zhou, L.; Deng, R.-P.; Zhang, H.-J., *Int. J. Quantum Chem* **2013**, *113* (11), 1641-1649.
52. Angelis, F. D.; Belpassi, L.; Fantacci, S., *J. Mol. Struct.* **2009**, *914* (1), 74-86.

53. Li, X.; Minaev, B.; Ågren, H.; Tian, H., *J. Phys. Chem. C* **2011**, *115* (42), 20724-20731.
54. Świderek, K.; Paneth, P., *J. Phys. Org. Chem.* **2009**, *22* (9), 845-856.
55. Li, X.; Minaev, B.; Ågren, H.; Tian, H., *Eur. J. Inorg. Chem.* **2011**, *2011* (16), 2517-2524.
56. Jansson, E.; Minaev, B.; Schrader, S.; Ågren, H., *Chem. Phys.* **2007**, *333* (2-3), 157-167.
57. De Angelis, F.; Fantacci, S.; Evans, N.; Klein, C.; Zakeeruddin, S. M.; Moser, J.-E.; Kalyanasundaram, K.; Bolink, H. J.; Grätzel, M.; Nazeeruddin, M. K., *Inorg. Chem.* **2007**, *46* (15), 5989-6001.
58. Tsuchiya, K.; Yagai, S.; Kitamura, A.; Karatsu, T.; Endo, K.; Mizukami, J.; Akiyama, S.; Yabe, M., *Eur. J. Inorg. Chem.* **2010**, *2010* (6), 926-933.
59. Cho, Y.-J.; Kim, S.-Y.; Kim, J.-H.; Lee, J.; Cho, D. W.; Yi, S.; Son, H.-J.; Han, W.-S.; Kang, S. O., *J. Mater. Chem. C* **2017**, *5* (7), 1651-1659.
60. Chien, C. H.; Fujita, S.; Yamoto, S.; Hara, T.; Yamagata, T.; Watanabe, M.; Mashima, K., *Dalton Trans* **2008**, (7), 916-23.
61. Lo, S.-C.; Shipley, C. P.; Bera, R. N.; Harding, R. E.; Cowley, A. R.; Burn, P. L.; Samuel, I. D. W., *Chem. Mater.* **2006**, *18* (21), 5119-5129.
62. Yanai, T.; Tew, D. P.; Handy, N. C., *Chem. Phys. Lett.* **2004**, *393* (1-3), 51-57.
63. Lu, K. Y.; Chou, H. H.; Hsieh, C. H.; Yang, Y. H.; Tsai, H. R.; Tsai, H. Y.; Hsu, L. C.; Chen, C. Y.; Chen, I. C.; Cheng, C. H., *Adv. Mater.* **2011**, *23* (42), 4933-7.
64. Shang, X.; Han, D.; Li, D.; Zhang, G., *J. Lumin.* **2014**, *147*, 127-133.
65. Han, D.; Li, H.; Shang, X.; Zhang, G.; Zhao, L., *Can. J. Chem.* **2013**, *91* (12), 1168-1173.
66. Tronnier, A.; Pothig, A.; Metz, S.; Wagenblast, G.; Munster, I.; Strassner, T., *Inorg. Chem.* **2014**, *53* (12), 6346-56.
67. Harvey, J. N.; Aschi, M.; Schawarz, H.; Koch, W., *Theor. Chem. Acc.* **1998**, *99*, 95-99.
68. Sasabe, H.; Takamatsu, J.; Motoyama, T.; Watanabe, S.; Wagenblast, G.; Langer, N.; Molt, O.; Fuchs, E.; Lennartz, C.; Kido, J., *Adv. Mater.* **2010**, *22* (44), 5003-7.

69. Yang, C.-H.; Cheng, Y.-M.; Chi, Y.; Hsu, C.-J.; Fang, F.-C.; Wong, K.-T.; Chou, P.-T.; Chang, C.-H.; Tsai, M.-H.; Wu, C.-C., *Angew. Chem. Int. Ed.* **2007**, *46* (14), 2418-2421.
70. Xie, L. M.; Bai, F. Q.; Li, W.; Zhang, Z. X.; Zhang, H. X., *Phys. Chem. Chem. Phys.* **2015**, *17* (15), 10014-21.
71. Lanoë, P.-H.; Chan, J.; Gontard, G.; Monti, F.; Armaroli, N.; Barbieri, A.; Amouri, H., *Eur. J. Inorg. Chem.* **2016**, *2016* (11), 1631-1634.
72. Luo, Y.; Xu, Y.; Zhang, W.; Li, W.; Li, M.; He, R.; Shen, W., *J. Phys. Chem. C* **2016**, *120* (6), 3462-3471.
73. Unger, Y.; Strassner, T.; Lennartz, C., *J. Organomet. Chem.* **2013**, *748*, 63-67.
74. Xu, S.; Wang, J.; Xia, H.; Zhao, F.; Wang, Y., *J. Mol. Model.* **2015**, *21* (2), 22.
75. Peng, Q.; Shi, Q.; Niu, Y.; Yi, Y.; Sun, S.; Li, W.; Shuai, Z., *J. Mater. Chem. C* **2016**, *4* (28), 6829-6838.
76. Younker, J. M.; Dobbs, K. D., *J. Phys. Chem. C* **2013**, *117* (48), 25714-25723.
77. Haneder, S.; Da Como, E.; Feldmann, J.; Lupton, J. M.; Lennartz, C.; Erk, P.; Fuchs, E.; Molt, O.; Münster, I.; Schildknecht, C.; Wagenblast, G., *Adv. Mater.* **2008**, *20* (17), 3325-3330.
78. Sajoto, T.; Djurovich, P. I.; Tamayo, A. B.; Oxgaard, J.; Goddard, W. A.; Thompson, M. E., *J. Am. Chem. Soc.* **2009**, *131*, 9813-9822.
79. Zhou, X.; Burn, P. L.; Powell, B. J., *Inorg. Chem.* **2016**, *55* (11), 5266-5273.
80. Escudero, D., *Chem. Sci.* **2016**, *7* (2), 1262-1267.
81. Adamo, C.; Barone, V., *J. Chem. Phys.* **1999**, *110* (13), 6158-6170.
82. Li, X.; Zhang, Q.; Tu, Y.; Agren, H.; Tian, H., *Phys. Chem. Chem. Phys.* **2010**, *12* (41), 13730-13736.
83. Liu, T.; Xia, B. H.; Zheng, Q. C.; Zhou, X.; Pan, Q. J.; Zhang, H. X., *J. Comput. Chem.* **2010**, *31* (3), 628-38.
84. Wang, J.; Bai, F. Q.; Xia, B. H.; Zhang, H. X.; Cui, T., *J. Mol. Model.* **2014**, *20* (3), 2108.
85. Hay, P. J.; Wadt, W. R., *J. Chem. Phys.* **1985**, *82* (1), 299-310.
86. Hariharan, P. C.; Pople, J. A., *Mol. Phys.* **1974**, *27* (1), 209-214.

87. Zhao, Y.; Schultz, N. E.; Truhlar, D. G., *J. Chem. Theory Comput.* **2006**, *2* (2), 364-382.
88. Zhao, Y.; Truhlar, D. G., *Theor. Chem. Acc.* **2007**, *120* (1), 215-241.
89. Chai, J.-D.; Head-Gordon, M., *Phys. Chem. Chem. Phys.* **2008**, *10* (44), 6615-6620.
90. Caspar, J. V.; Kober, E. M.; Sullivan, B. P.; Meyer, T. J., *J. Am. Chem. Soc.* **1982**, *104*, 630-632.
91. Caspar, J. V.; Meyer, T. J., *J. Phys. Chem.* **1983**, *87*, 952-957.
92. Kober, E. M.; Caspar, J. V.; Lumpkin, R. S.; Meyer, T. J., *J. Phys. Chem.* **1986**, *90* (16), 3722-3734.
93. Ren, X.-Y.; Wu, Y.; Wang, L.; Zhao, L.; Zhang, M.; Geng, Y.; Su, Z.-M., *J. Mol. Graphics Modell.* **2014**, *51*, 149-157.
94. Koseki, S.; Fedorov, D. G.; Schmidt, M. W.; Gordon, M. S., *J. Phys. Chem. A* **2001**, *105* (35), 8262-8268.
95. Koseki, S.; Schmidt, M. W.; Gordon, M. S., *J. Phys. Chem. A* **1998**, *102*, 10430-10435.
96. Satek, P.; Vahtras, O.; Helgaker, T.; Ågren, H., *J. Chem. Phys.* **2002**, *117* (21), 9630-9645.
97. Tunell, I.; Rinkevicius, Z.; Vahtras, O.; Satek, P.; Helgaker, T.; Ågren, H., *J. Chem. Phys.* **2003**, *119* (21), 11024-11034.
98. Aidas, K.; Angeli, C.; Bak, K. L.; Bakken, V.; Bast, R.; Boman, L.; Christiansen, O.; Cimiraglia, R.; Coriani, S.; Dahle, P.; Dalskov, E. K.; Ekstrom, U.; Enevoldsen, T.; Eriksen, J. J.; Ettenhuber, P.; Fernandez, B.; Ferrighi, L.; Fliegl, H.; Frediani, L.; Hald, K.; Halkier, A.; Hattig, C.; Heiberg, H.; Helgaker, T.; Hennum, A. C.; Hetttema, H.; Hjertenaes, E.; Host, S.; Hoyvik, I. M.; Iozzi, M. F.; Jansik, B.; Jensen, H. J.; Jonsson, D.; Jorgensen, P.; Kauczor, J.; Kirpekar, S.; Kjaergaard, T.; Klopper, W.; Knecht, S.; Kobayashi, R.; Koch, H.; Kongsted, J.; Krapp, A.; Kristensen, K.; Ligabue, A.; Lutnaes, O. B.; Melo, J. I.; Mikkelsen, K. V.; Myhre, R. H.; Neiss, C.; Nielsen, C. B.; Norman, P.; Olsen, J.; Olsen, J. M.; Osted, A.; Packer, M. J.; Pawłowski, F.; Pedersen, T. B.; Provasi, P. F.; Reine, S.; Rinkevicius, Z.; Ruden, T. A.; Ruud, K.; Rybkin, V. V.; Salek, P.; Samson, C. C.; de Meras, A. S.; Saue, T.;

- Sauer, S. P.; Schimmelpfennig, B.; Sneskov, K.; Steindal, A. H.; Sylvester-Hvid, K. O.; Taylor, P. R.; Teale, A. M.; Tellgren, E. I.; Tew, D. P.; Thorvaldsen, A. J.; Thogersen, L.; Vahtras, O.; Watson, M. A.; Wilson, D. J.; Ziolkowski, M.; Agren, H., *Wiley Interdiscip. Rev.: Comput. Mol. Sci.* **2014**, *4* (3), 269-284.
99. Omae, I., *Coord. Chem. Rev.* **2016**, *310*, 154-169.
100. Escudero, D.; Jacquemin, D., *Dalton Trans.* **2015**, *44* (18), 8346-8355.
101. Neese, F., *Wiley Interdiscip. Rev.: Comput. Mol. Sci.* **2012**, *2* (1), 73-78.
102. Escudero, D.; Heuser, E.; Meier, R. J.; Schaferling, M.; Thiel, W.; Holder, E., *Chemistry* **2013**, *19* (46), 15639-44.





APPENDIX



**Table A1.** Energy (eV), electron contribution (%), and main assignment of each molecular orbital (MO) involving absorption and emission transitions for **1**.

MO	Energy (eV)	Composition (%)				Assignment
		Ir	NHC1	NHC2	NHC3	
L+5	0.97	4	3	10	83	$\pi^*(\text{NHC3})$
L+4	0.87	6	27	61	5	$\pi^*(\text{NHC1+NHC2})$
L+3	0.70	2	67	26	6	$\pi^*(\text{NHC1+NHC2})$
L+2	0.32	5	5	9	81	$\pi^*(\text{NHC3})$
L+1	0.20	5	25	67	3	$\pi^*(\text{NHC1+NHC2})$
LUMO	0.10	3	66	20	10	$\pi^*(\text{NHC1+NHC2})$
HOMO	-4.56	41	8	19	31	$d(\text{Ir}) + \pi(\text{NHC2+NHC3})$
H-1	-4.86	36	35	13	16	$d(\text{Ir}) + \pi(\text{NHC})$
H-2	-5.03	26	19	33	22	$d(\text{Ir}) + \pi(\text{NHC})$
H-3	-5.30	9	29	39	24	$\pi(\text{NHC})$
H-4	-5.41	9	27	15	49	$\pi(\text{NHC})$
H-5	-5.59	7	41	47	4	$\pi(\text{NHC1+NHC2})$

**Table A2.** Energy (eV), electron contribution (%), and main assignment of each molecular orbital (MO) involving absorption and emission transitions for **1a**.

MO	Energy (eV)	Composition (%)				Assignment
		Ir	NHC1	NHC2	NHC3	
L+5	0.13	1	3	8	88	$\pi^*(\text{NHC3})$
L+4	0.01	1	7	86	6	$\pi^*(\text{NHC2})$
L+3	-0.07	1	90	5	5	$\pi^*(\text{NHC1})$
L+2	-0.44	4	3	3	89	$\pi^*(\text{NHC3})$
L+1	-0.52	6	10	82	2	$\pi^*(\text{NHC2})$
LUMO	-0.64	2	81	10	6	$\pi^*(\text{NHC1})$
HOMO	-4.76	36	7	22	34	$d(\text{Ir}) + \pi(\text{NHC2+NHC3})$
H-1	-5.11	26	43	18	12	$d(\text{Ir}) + \pi(\text{NHC})$
H-2	-5.23	7	21	34	37	$\pi(\text{NHC})$
H-3	-5.51	4	32	23	41	$\pi(\text{NHC})$
H-4	-5.57	23	20	31	26	$d(\text{Ir}) + \pi(\text{NHC})$
H-5	-5.68	10	40	46	4	$\pi(\text{NHC1+NHC2})$

**Table A3.** Energy (eV), electron contribution (%), and main assignment of each molecular orbital (MO) involving absorption and emission transitions for **1b**.

MO	Energy (eV)	Composition (%)				Assignment
		Ir	NHC1	NHC2	NHC3	
L+5	0.35	5	29	58	8	$\pi^*(\text{NHC1}+\text{NHC2})$
L+4	0.32	4	29	44	22	$\pi^*(\text{NHC})$
L+3	0.18	3	75	14	8	$\pi^*(\text{NHC1}+\text{NHC2})$
L+2	-1.03	0	5	93	2	$\pi^*(\text{NHC2})$
L+1	-1.06	0	6	3	91	$\pi^*(\text{NHC3})$
LUMO	-1.17	0	89	3	7	$\pi^*(\text{NHC1})$
HOMO	-4.69	38	13	18	30	$d(\text{Ir})+\pi(\text{NHC})$
H-1	-4.77	25	23	27	25	$d(\text{Ir})+\pi(\text{NHC})$
H-2	-4.84	32	13	24	32	$d(\text{Ir})+\pi(\text{NHC})$
H-3	-5.29	1	54	41	4	$\pi(\text{NHC1}+\text{NHC2})$
H-4	-5.40	3	29	42	25	$\pi(\text{NHC})$
H-5	-5.46	5	40	17	37	$\pi(\text{NHC})$

**Table A4.** Energy (eV), electron contribution (%), and main assignment of each molecular orbital (MO) involving absorption and emission transitions for **2a**.

MO	Energy (eV)	Composition (%)				Assignment
		Ir	NHC1	NHC2	NHC3	
L+5	0.45	6	4	4	85	$\pi^*(\text{NHC3})$
L+4	0.36	7	16	75	2	$\pi^*(\text{NHC1}+\text{NHC2})$
L+3	0.24	4	73	16	7	$\pi^*(\text{NHC1}+\text{NHC2})$
L+2	-0.60	0	1	0	99	$\pi^*(\text{NHC3})$
L+1	-0.70	0	1	99	0	$\pi^*(\text{NHC2})$
LUMO	-0.79	0	98	1	1	$\pi^*(\text{NHC1})$
HOMO	-4.66	33	12	9	47	$d(\text{Ir})+\pi(\text{NHC1}+\text{NHC3})$
H-1	-4.70	28	19	21	32	$d(\text{Ir})+\pi(\text{NHC})$
H-2	-4.74	26	16	42	17	$d(\text{Ir})+\pi(\text{NHC})$
H-3	-5.11	1	52	39	8	$\pi(\text{NHC1}+\text{NHC2})$
H-4	-5.25	11	48	22	19	$d(\text{Ir})+\pi(\text{NHC})$
H-5	-5.38	2	18	35	45	$\pi(\text{NHC})$

**Table A5.** Energy (eV), electron contribution (%), and main assignment of each molecular orbital (MO) involving absorption and emission transitions for **2b**.

MO	Energy (eV)	Composition (%)				Assignment
		Ir	NHC1	NHC2	NHC3	
L+5	-0.63	0	7	1	92	$\pi^*(\text{NHC3})$
L+4	-0.65	0	14	83	3	$\pi^*(\text{NHC1+NHC2})$
L+3	-0.78	0	78	17	5	$\pi^*(\text{NHC1+NHC2})$
L+2	-1.03	1	2	51	46	$\pi^*(\text{NHC2+NHC3})$
L+1	-1.03	0	9	40	51	$\pi^*(\text{NHC2+NHC3})$
LUMO	-1.15	0	90	8	2	$\pi^*(\text{NHC1})$
HOMO	-4.38	16	26	27	31	$d(\text{Ir})+\pi(\text{NHC})$
H-1	-4.42	16	9	29	47	$d(\text{Ir})+\pi(\text{NHC2+NHC3})$
H-2	-4.71	7	51	34	7	$\pi(\text{NHC1+NHC2})$
H-3	-4.86	35	13	24	28	$d(\text{Ir})+\pi(\text{NHC})$
H-4	-5.36	19	55	15	12	$d(\text{Ir})+\pi(\text{NHC})$
H-5	-5.54	2	14	40	44	$\pi(\text{NHC})$

**Table A6.** Energy (eV), electron contribution (%), and main assignment of each molecular orbital (MO) involving absorption and emission transitions for **3a**.

MO	Energy (eV)	Composition (%)				Assignment
		Ir	NHC1	NHC2	NHC3	
L+5	0.44	1	0	1	98	$\pi^*(\text{NHC3})$
L+4	0.40	1	96	2	1	$\pi^*(\text{NHC1})$
L+3	0.32	0	0	99	0	$\pi^*(\text{NHC2})$
L+2	-0.24	2	5	5	88	$\pi^*(\text{NHC3})$
L+1	-0.35	3	54	43	0	$\pi^*(\text{NHC1+NHC2})$
LUMO	-0.42	1	39	50	9	$\pi^*(\text{NHC1+NHC2})$
HOMO	-4.68	37	9	19	35	$d(\text{Ir})+\pi(\text{NHC2+NHC3})$
H-1	-4.96	30	37	17	16	$d(\text{Ir})+\pi(\text{NHC})$
H-2	-5.05	15	25	30	29	$d(\text{Ir})+\pi(\text{NHC})$
H-3	-5.31	7	23	33	37	$\pi(\text{NHC})$
H-4	-5.40	22	32	18	28	$d(\text{Ir})+\pi(\text{NHC})$
H-5	-5.53	10	46	32	12	$\pi(\text{NHC})$

**Table A7.** Energy (eV), electron contribution (%), and main assignment of each molecular orbital (MO) involving absorption and emission transitions for **3b**.

MO	Energy (eV)	Composition (%)				Assignment
		Ir	NHC1	NHC2	NHC3	
L+5	0.42	1	1	1	98	$\pi^*(\text{NHC3})$
L+4	0.31	1	79	20	0	$\pi^*(\text{NHC1+NHC2})$
L+3	0.29	1	19	80	1	$\pi^*(\text{NHC1+NHC2})$
L+2	-0.33	2	7	4	88	$\pi^*(\text{NHC3})$
L+1	-0.45	2	42	55	1	$\pi^*(\text{NHC1+NHC2})$
LUMO	-0.51	1	50	40	10	$\pi^*(\text{NHC1+NHC2})$
HOMO	-4.54	31	8	20	41	$d(\text{Ir})+\pi(\text{NHC2+NHC3})$
H-1	-4.82	19	30	36	15	$d(\text{Ir})+\pi(\text{NHC})$
H-2	-4.86	10	40	19	32	$\pi(\text{NHC})$
H-3	-5.18	14	15	36	35	$d(\text{Ir})+\pi(\text{NHC})$
H-4	-5.30	28	36	13	23	$d(\text{Ir})+\pi(\text{NHC})$
H-5	-5.47	14	38	30	19	$d(\text{Ir})+\pi(\text{NHC})$

**Table A8.** Energy (eV), electron contribution (%), and main assignment of each molecular orbital (MO) involving absorption and emission transitions for **4a**.

MO	Energy (eV)	Composition (%)				Assignment
		Ir	NHC1	NHC2	NHC3	
L+5	-0.24	1	40	53	7	$\pi^*(\text{NHC1+NHC2})$
L+4	-0.33	1	33	6	60	$\pi^*(\text{NHC1+NHC3})$
L+3	-0.38	2	6	2	90	$\pi^*(\text{NHC3})$
L+2	-0.47	3	3	28	65	$\pi^*(\text{NHC2+NHC3})$
L+1	-0.52	3	4	60	34	$\pi^*(\text{NHC2+NHC3})$
LUMO	-0.59	3	64	3	30	$\pi^*(\text{NHC1+NHC3})$
HOMO	-4.65	38	13	28	22	$d(\text{Ir})+\pi(\text{NHC})$
H-1	-5.06	25	42	23	10	$d(\text{Ir})+\pi(\text{NHC1+NHC2})$
H-2	-5.15	6	23	24	47	$\pi(\text{NHC})$
H-3	-5.44	5	32	36	26	$\pi(\text{NHC})$
H-4	-5.50	23	29	28	20	$d(\text{Ir})+\pi(\text{NHC})$
H-5	-5.54	7	37	45	11	$\pi(\text{NHC})$

**Table A9.** Energy (eV), electron contribution (%), and main assignment of each molecular orbital (MO) involving absorption and emission transitions for **4b**.

MO	Energy (eV)	Composition (%)				Assignment
		Ir	NHC1	NHC2	NHC3	
L+5	-0.32	1	32	57	10	$\pi^*(\text{NHC1}+\text{NHC2})$
L+4	-0.43	1	18	3	78	$\pi^*(\text{NHC1}+\text{NHC3})$
L+3	-0.51	1	3	1	96	$\pi^*(\text{NHC3})$
L+2	-1.18	2	7	9	81	$\pi^*(\text{NHC3})$
L+1	-1.25	3	4	86	7	$\pi^*(\text{NHC2})$
LUMO	-1.30	2	85	2	11	$\pi^*(\text{NHC1}+\text{NHC3})$
HOMO	-4.73	33	13	31	23	$d(\text{Ir})+\pi(\text{NHC})$
H-1	-5.10	11	23	42	24	$d(\text{Ir})+\pi(\text{NHC})$
H-2	-5.12	8	46	7	39	$\pi(\text{NHC1}+\text{NHC3})$
H-3	-5.44	9	13	46	33	$\pi(\text{NHC})$
H-4	-5.50	3	30	47	20	$\pi(\text{NHC})$
H-5	-5.53	13	60	6	21	$d(\text{Ir})+\pi(\text{NHC1}+\text{NHC3})$

**Table A10.** Calculated absorption energies [ $\lambda$  (nm)/ $E$  (eV)], oscillator strength ( $f$ ), orbital contributions, and charge transfer characters associated with experimental wavelength (nm) for selected vertical  $S_0 \rightarrow S_n$  transitions of the complexes in series **1**.

1						
States	$\lambda/E$	$f$	Contribution	Character	%MLCT	Exp
$S_1$	307/4.04	0.035	H $\rightarrow$ L (89%)	MLCT/ILCT	35	
$S_4$	286/4.34	0.063	H-1 $\rightarrow$ L (88%)	MLCT/ILCT	30	290
$S_6$	278/4.47	0.064	H-2 $\rightarrow$ L (55%)	MLCT/ILCT	23	
			H-1 $\rightarrow$ L+1 (33%)	MLCT/ILCT		
$S_{10}$	267/4.64	0.103	H-2 $\rightarrow$ L+2 (43%)	MLCT/ILCT	25	268
			H $\rightarrow$ L+3 (38%)	MLCT/ILCT		

**Table A10.** Calculated absorption energies [ $\lambda$  (nm)/ $E$  (eV)], oscillator strength ( $f$ ), orbital contributions, and charge transfer characters associated with experimental wavelength (nm) for selected vertical  $S_0 \rightarrow S_n$  transitions of the complexes in series **1** (Continued).

<b>1a</b>						
States	$\lambda/E$	$f$	Contribution	Character	%MLCT	Exp
$S_1$	326/3.80	0.007	H $\rightarrow$ L (83%)	MLCT/ILCT	32	
$S_4$	301/4.13	0.075	H-1 $\rightarrow$ LUMO (84%)	MLCT/ILCT	22	
$S_6$	291/4.26	0.102	H-1 $\rightarrow$ L+2 (71%)	MLCT/ILCT	17	
$S_7$	287/4.32	0.147	H-2 $\rightarrow$ LUMO (54%)	ILCT	7	
$S_8$	285/4.36	0.245	HOMO $\rightarrow$ L+3 (70%)	MLCT/ILCT	25	304
$S_{12}$	276/4.49	0.069	HOMO $\rightarrow$ L+5 (63%)	MLCT/ILCT	26	
$S_{14}$	268/4.63	0.157	H-3 $\rightarrow$ L+1 (64%)	ILCT	0	
$S_{19}$	261/4.75	0.175	H-4 $\rightarrow$ L+2 (27%)	MLCT/ILCT	11	
			H-4 $\rightarrow$ L+1 (16%)	MLCT/ILCT		
$S_{26}$	255/4.86	0.117	H-2 $\rightarrow$ L+3 (52%)	ILCT	6	
<b>1b</b>						
States	$\lambda/E$	$f$	Contribution	Character	%MLCT	Exp
$S_1$	390/3.18	0.005	H $\rightarrow$ L (89%)	MLCT/ILCT	36	
$S_2$	384/3.23	0.090	H-1 $\rightarrow$ L (60%)	MLCT/ILCT	24	
			H-1 $\rightarrow$ L+1 (23%)	MLCT/ILCT		
$S_3$	379/3.27	0.084	H $\rightarrow$ L+1 (50%)	MLCT/ILCT	36	375
			H $\rightarrow$ L+2 (44%)	MLCT/ILCT		
$S_8$	355/3.50	0.078	H-2 $\rightarrow$ L+1 (85%)	MLCT/ILCT	28	
$S_{19}$	289/4.29	0.072	H $\rightarrow$ L+3 (63%)	MLCT/ILCT	25	302
$S_{35}$	266/4.66	0.202	H-8 $\rightarrow$ L (22%)	ILCT	4	260
			H-6 $\rightarrow$ L+2 (14%)	ILCT		
$S_{38}$	263/4.71	0.123	H-7 $\rightarrow$ L+1 (21%)	ILCT	7	
			H-6 $\rightarrow$ L+2 (14%)	ILCT		

**Table A11.** Calculated absorption energies [ $\lambda$  (nm)/ $E$  (eV)], oscillator strength ( $f$ ), orbital contributions, and charge transfer characters associated with experimental wavelength (nm) for selected vertical  $S_0 \rightarrow S_n$  transitions of the complexes in series 2.

<b>2a</b>					
States	$\lambda/E$	$f$	Contribution	Character	%MLCT
$S_1$	355/3.49	0.041	H $\rightarrow$ L (79%)	MLCT/ILCT	29
$S_2$	352/3.52	0.071	H $\rightarrow$ L+1 (68%)	MLCT/ILCT	28
$S_7$	337/3.68	0.070	H $\rightarrow$ L+2 (40%)	MLCT/ILCT	26
			H-2 $\rightarrow$ L+1 (27%)	MLCT/ILCT	
$S_{10}$	311/3.99	0.076	H-3 $\rightarrow$ L (89%)	ILCT	2
$S_{19}$	285/4.36	0.108	H-2 $\rightarrow$ L+3 (25%)	MLCT/ILCT	11
			H-5 $\rightarrow$ L+2 (18%)	ILCT	
$S_{22}$	282/4.40	0.109	H-1 $\rightarrow$ L+3 (27%)	MLCT/ILCT	11
			H-2 $\rightarrow$ L+3 (19%)	MLCT/ILCT	
$S_{37}$	250/4.96	0.107	H-4 $\rightarrow$ L+3 (27%)	ILCT	5
			H-1 $\rightarrow$ L+7 (15%)	MLCT/ILCT	
<b>2b</b>					
States	$\lambda/E$	$f$	Contribution	Character	%MLCT
$S_1$	427/2.91	0.156	H $\rightarrow$ L (88%)	MLCT/ILCT	15
$S_2$	418/2.96	0.146	H-1 $\rightarrow$ L (33%)	MLCT/ILCT	13
			H $\rightarrow$ L+1 (22%)	MLCT/ILCT	
$S_9$	389/3.19	0.161	H-1 $\rightarrow$ L+4 (29%)	MLCT/ILCT	12
			H-1 $\rightarrow$ L+3 (17%)	MLCT/ILCT	
$S_{13}$	369/3.36	0.228	H-2 $\rightarrow$ L+2 (65%)	ILCT	7
$S_{28}$	306/4.06	0.141	H-4 $\rightarrow$ L+2 (39%)	MLCT/ILCT	15
			H $\rightarrow$ L+6 (26%)	MLCT/ILCT	
$S_{51}$	269/4.62	0.105	H-5 $\rightarrow$ L+5 (21%)	ILCT	8
			H-3 $\rightarrow$ L+7 (20%)	MLCT/ILCT	
$S_{62}$	258/4.80	0.176	H-6 $\rightarrow$ L+3 (17%)	ILCT	4
			H-8 $\rightarrow$ L (16%)	ILCT	

**Table A12.** Calculated absorption energies [ $\lambda$  (nm)/ $E$  (eV)], oscillator strength ( $f$ ), orbital contributions, and charge transfer characters associated with experimental wavelength (nm) for selected vertical  $S_0 \rightarrow S_n$  transitions of the complexes in series **3**.

<b>3a</b>					
States	$\lambda/E$	$f$	Contribution	Character	%MLCT
$S_1$	332/3.73	0.110	H $\rightarrow$ L (91%)	MLCT/ILCT	33
$S_5$	305/4.07	0.198	H-2 $\rightarrow$ L (54%)	MLCT/ILCT	18
			H-1 $\rightarrow$ L+1 (29%)	MLCT/ILCT	
$S_{12}$	274/4.52	0.127	H-3 $\rightarrow$ L+1 (33%)	ILCT	11
			H-4 $\rightarrow$ L+1 (11%)	MLCT/ILCT	
$S_{18}$	269/4.61	0.392	H-4 $\rightarrow$ L+2 (25%)	MLCT/ILCT	12
			H-5 $\rightarrow$ L (15%)	ILCT	
$S_{20}$	267/4.64	0.459	H-5 $\rightarrow$ L+1 (33%)	ILCT	12
			H-4 $\rightarrow$ L+1 (20%)	MLCT/ILCT	
$S_{23}$	263/4.71	0.171	H $\rightarrow$ L+8 (38%)	MLCT/ILCT	18
			H-3 $\rightarrow$ L+2 (16%)	ILCT	
<b>3b</b>					
States	$\lambda/E$	$f$	Contribution	Character	%MLCT
$S_1$	350/3.54	0.212	H $\rightarrow$ L (92%)	MLCT/ILCT	28
$S_4$	325/3.82	0.171	H-1 $\rightarrow$ L (75%)	MLCT/ILCT	15
$S_5$	320/3.87	0.300	H-2 $\rightarrow$ L (40%)	ILCT	12
			H-1 $\rightarrow$ L+1 (33%)	MLCT/ILCT	
$S_8$	309/4.01	0.118	H-2 $\rightarrow$ L+1 (51%)	ILCT	9
$S_{15}$	286/4.33	0.295	H-3 $\rightarrow$ L+1 (34%)	MLCT/ILCT	14
$S_{17}$	282/4.39	0.232	H-4 $\rightarrow$ L+2 (42%)	MLCT/ILCT	16
			H-3 $\rightarrow$ L+2 (30%)	MLCT/ILCT	
$S_{20}$	277/4.47	0.326	H-6 $\rightarrow$ L+1 (38%)	MLCT/ILCT	15
			H-6 $\rightarrow$ L (23%)	MLCT/ILCT	
$S_{41}$	251/4.93	0.101	H-7 $\rightarrow$ L (29%)	ILCT	6
			H $\rightarrow$ L+11 (19%)	MLCT/ILCT	



**Table A13.** Calculated absorption energies [ $\lambda$  (nm)/ $E$  (eV)], oscillator strength ( $f$ ), orbital contributions, and charge transfer characters associated with experimental wavelength (nm) for selected vertical  $S_0 \rightarrow S_n$  transitions of the complexes in series **4**.

<b>4a</b>					
States	$\lambda/E$	$f$	Contribution	Character	%MLCT
$S_1$	340/3.65	0.003	H $\rightarrow$ L (46%)	MLCT/ILCT	33
			H $\rightarrow$ L+1 (44%)	MLCT/ILCT	
$S_7$	301/4.12	0.108	H-1 $\rightarrow$ L+1 (73%)	MLCT/ILCT	18
$S_{12}$	289/4.29	0.091	H $\rightarrow$ L+7 (53%)	MLCT/ILCT	21
			H-2 $\rightarrow$ L+1 (28%)	ILCT	
$S_{20}$	276/4.50	0.083	H-3 $\rightarrow$ L+1 (21%)	ILCT	10
			H $\rightarrow$ L+10 (14%)	MLCT/ILCT	
$S_{26}$	270/4.60	0.101	H-3 $\rightarrow$ L+2 (56%)	ILCT	3
$S_{31}$	266/4.67	0.096	H-4 $\rightarrow$ L (19%)	MLCT/ILCT	8
			H-5 $\rightarrow$ L+1 (14%)	ILCT	
$S_{59}$	248/5.01	0.061	H-6 $\rightarrow$ L (12%)	ILCT	7
			H-2 $\rightarrow$ L+9 (11%)	ILCT	
<b>4b</b>					
States	$\lambda/E$	$f$	Contribution	Character	%MLCT
$S_1$	385/3.22	0.009	H $\rightarrow$ L+1 (64%)	MLCT/ILCT	28
			H $\rightarrow$ L (29%)	MLCT/ILCT	
$S_7$	335/3.71	0.103	H-1 $\rightarrow$ L+2 (56%)	ILCT	6
			H-2 $\rightarrow$ L+1 (22%)	ILCT	
$S_9$	324/3.83	0.057	H-2 $\rightarrow$ L+2 (55%)	ILCT	5
$S_{10}$	312/3.97	0.113	H-3 $\rightarrow$ L+1 (34%)	ILCT	7
$S_{16}$	304/4.08	0.117	H-6 $\rightarrow$ L+1 (25%)	MLCT/ILCT	14
			H-5 $\rightarrow$ L+1 (14%)	MLCT/ILCT	
$S_{24}$	293/4.23	0.143	H $\rightarrow$ L+4 (82%)	MLCT/ILCT	26
$S_{29}$	282/4.40	0.212	H $\rightarrow$ L+8 (43%)	MLCT/ILCT	16
			H-7 $\rightarrow$ L+1 (10%)	ILCT	

**Table A14.** Transition dipole moments [ $\mu(S_n)$ , Debye], singlet-triplet splitting energies [ $\Delta E(S_n - T_1)$ , eV], and SOC constants [ $\langle S_n | \hat{H}_{SO} | T_1 \rangle$ ,  $\text{cm}^{-1}$ ] for the complexes of series 1.

	<b>1</b>			<b>1a</b>		
	$\mu(S_n)$	$\Delta E(S_n - T_1)$	$\langle S_n   \hat{H}_{SO}   T_1 \rangle$	$\mu(S_n)$	$\Delta E(S_n - T_1)$	$\langle S_n   \hat{H}_{SO}   T_1 \rangle$
$S_1$	0.80	0.47	35.58	0.66	0.16	62.18
$S_2$	0.79	0.54	33.44	0.28	0.24	27.29
$S_3$	0.56	0.62	47.13	0.70	0.32	14.74
$S_4$	1.38	0.79	188.24	1.05	0.51	309.61
$S_5$	0.88	0.89	134.01	0.79	0.64	82.75
$S_6$	1.72	0.99	194.58	2.08	0.73	182.17

<b>1b</b>			
	$\mu(S_n)$	$\Delta E(S_n - T_1)$	$\langle S_n   \hat{H}_{SO}   T_1 \rangle$
$S_1$	0.85	0.74	78.95
$S_2$	1.64	0.85	193.82
$S_3$	0.91	0.87	78.45
$S_4$	1.29	0.88	27.75
$S_5$	0.88	0.90	57.77
$S_6$	1.19	0.98	145.62

**Table A15.** Transition dipole moments [ $\mu(S_n)$ , Debye], singlet-triplet splitting energies [ $\Delta E(S_n - T_1)$ , eV], and SOC constants [ $\langle S_n | \hat{H}_{SO} | T_1 \rangle$ ,  $\text{cm}^{-1}$ ] for the complexes of series 2.

	<b>2a</b>			<b>2b</b>		
	$\mu(S_n)$	$\Delta E(S_n - T_1)$	$\langle S_n   \hat{H}_{SO}   T_1 \rangle$	$\mu(S_n)$	$\Delta E(S_n - T_1)$	$\langle S_n   \hat{H}_{SO}   T_1 \rangle$
$S_1$	0.53	0.82	220.73	1.77	0.80	12.17
$S_2$	0.97	0.90	41.82	1.25	0.83	38.29
$S_3$	0.50	0.91	152.44	1.78	0.92	115.73
$S_4$	1.45	0.95	74.81	1.30	0.92	0.97
$S_5$	0.78	0.98	27.34	1.92	0.96	89.44
$S_6$	0.21	0.99	5.98	1.34	0.97	9.92

**Table A16.** Transition dipole moments [ $\mu(S_n)$ , Debye], singlet-triplet splitting energies [ $\Delta E(S_n - T_1)$ , eV], and SOC constants [ $\langle S_n | \hat{H}_{SO} | T_1 \rangle$ ,  $\text{cm}^{-1}$ ] for the complexes of series 3.

	3a			3b		
	$\mu(S_n)$	$\Delta E(S_n - T_1)$	$\langle S_n   \hat{H}_{SO}   T_1 \rangle$	$\mu(S_n)$	$\Delta E(S_n - T_1)$	$\langle S_n   \hat{H}_{SO}   T_1 \rangle$
$S_1$	1.56	0.56	29.18	2.12	0.63	23.46
$S_2$	0.96	0.62	53.02	1.04	0.69	47.43
$S_3$	1.45	0.71	18.32	2.11	0.78	20.48
$S_4$	2.05	0.87	184.88	2.30	0.94	133.10
$S_5$	2.21	0.93	121.21	4.27	0.99	96.71
$S_6$	3.10	0.99	150.63	1.80	1.03	103.51

**Table A17.** Transition dipole moments [ $\mu(S_n)$ , Debye], singlet-triplet splitting energies [ $\Delta E(S_n - T_1)$ , eV], and SOC constants [ $\langle S_n | \hat{H}_{SO} | T_1 \rangle$ ,  $\text{cm}^{-1}$ ] for the complexes of series 4.

	4a			4b		
	$\mu(S_n)$	$\Delta E(S_n - T_1)$	$\langle S_n   \hat{H}_{SO}   T_1 \rangle$	$\mu(S_n)$	$\Delta E(S_n - T_1)$	$\langle S_n   \hat{H}_{SO}   T_1 \rangle$
$S_1$	0.51	0.18	55.26	0.81	0.43	9.07
$S_2$	0.47	0.23	71.58	0.81	0.46	20.66
$S_3$	0.77	0.30	47.04	1.31	0.55	16.39
$S_4$	0.39	0.50	20.80	1.09	0.81	18.72
$S_5$	0.60	0.56	24.27	1.06	0.88	95.91
$S_6$	0.78	0.62	255.69	1.64	0.92	16.52

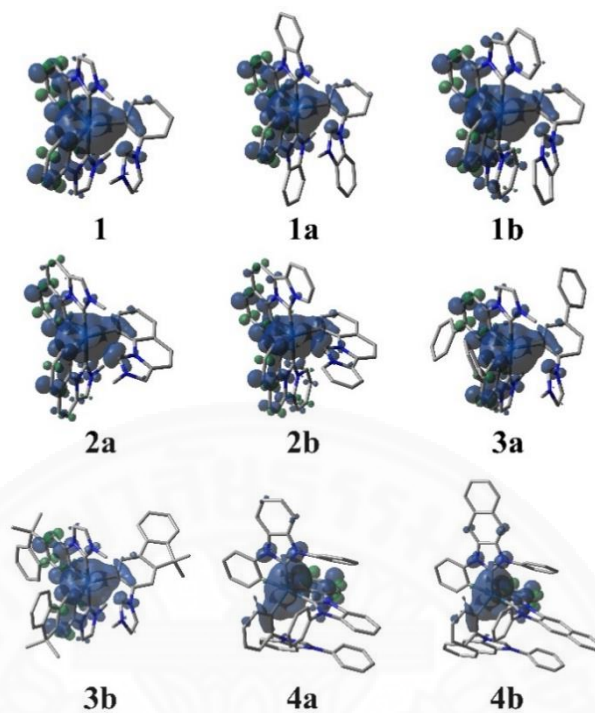


**Figure A1.** Spin density contributions at the optimized  $^3\text{MC}$  geometries for the complexes (isovalue = 0.002).

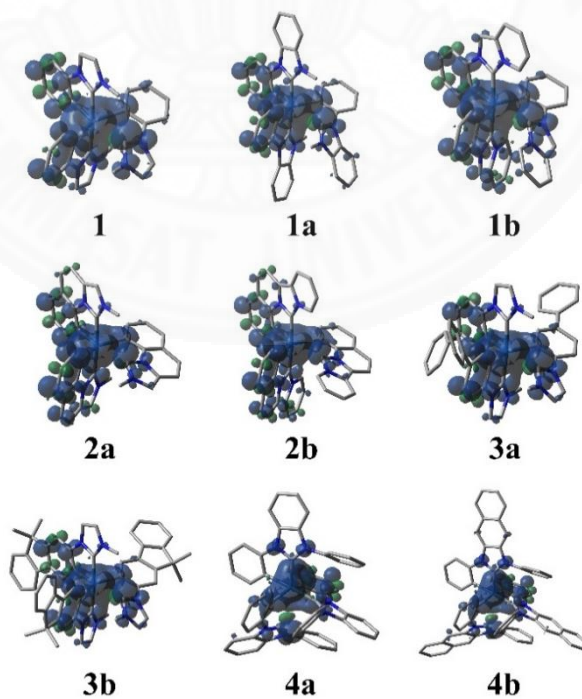


**Figure A2.** Spin density contributions at the optimized  $^3\text{TS}$  geometries for the complexes (isovalue = 0.002).

**BIOGRAPHY**

Name	Mr. Phoom Chumponanomakun
Date of Birth	October 3, 1991
Educational Attainment	2014: Bachelor of Science in Chemistry, Thammasat University
Scholarship	2010-present: Science Achievement Scholarship of Thailand, SAST 2017: Thammasat University under the TU Research Scholar

## Publications

Vittaya, L.; Leesakul, N.; Saithong, S.; Phongpaichit, S.; **Chumponanomakun, P.**;  
Boonprab, T.; Chainok, K.; Tantirungrotechai, Y., *ScienceAsia* **2017**, *43*, 175-185.